

Dipartimento di Elettronica,  
Informatica e Sistemistica  
Università di Bologna

Laboratoire de Physique de la  
Matière Condensée  
Université de Nice-Sophia Antipolis

---

Dottorato di Ricerca in Ingegneria  
Elettronica, Informatica  
e delle Telecomunicazioni  
ING-INF/02 - XIX Ciclo

Pour obtenir le grade de  
Docteur dans la  
Spécialité Physique

**STUDY, FABRICATION AND CHARACTERIZATION  
OF SEGMENTED WAVEGUIDES FOR ADVANCED  
PHOTONIC COMPONENTS ON LITHIUM NIOBATE**

**Davide Castaldini**

*Relatore:*

**Prof. Paolo Bassi**

*Co-relatore:*

**Prof. Pascal Baldi**

*Coordinatore*

**Prof. Paolo Bassi**

*Directeur de thèse:*

**Prof. Pascal Baldi**

*Co-directeur de thèse:*

**Prof. Paolo Bassi**

*Rapporteurs:*

**Dr Serge Valette**

**Dr Alain Barthelemy**

*Examineurs:*

**Prof. Fabrizio Frezza**

**Dott. Gian Giuseppe Bentini**

*Membrès invités*

**Dr Marc de Micheli**

**Dr Pierre Aschieri**

---

**A.A. 2005/2006**



*Alla mia famiglia*



# Contents

<b>Introduction</b>	<b>1</b>
<b>1 Segmented structures</b>	<b>5</b>
1.1 Introduction . . . . .	5
1.2 Propagation in periodic media . . . . .	5
1.3 Equivalence theorem for periodic media . . . . .	7
1.4 Periodically segmented waveguides . . . . .	10
1.5 Propagation losses in periodically segmented waveguides . . . . .	11
1.6 Cutoff properties of periodically segmented waveguides . . . . .	12
1.7 Segmented waveguides . . . . .	15
1.7.1 Mode transformers: Taper . . . . .	16
1.7.2 Mode filters . . . . .	19
<b>2 Numerical methods</b>	<b>23</b>
2.1 Introduction . . . . .	23
2.2 3D fully vectorial Beam Propagation Method . . . . .	24
2.2.1 Finite difference schematization . . . . .	29
2.2.2 Crank-Nicholson method . . . . .	30
2.2.3 Perfect Matched Layer . . . . .	31
2.2.4 BPM validation . . . . .	34
2.2.5 Consideration on the non-unitarity of BPM operators . . . . .	38
2.3 Finite difference mode solver . . . . .	38
2.3.1 Mode solver validation . . . . .	42
<b>3 Device fabrication techniques</b>	<b>45</b>
3.1 Introduction . . . . .	45
3.2 Properties of Lithium Niobate . . . . .	45
3.3 Waveguide fabrication . . . . .	47
3.3.1 Soft Proton Exchange . . . . .	48
3.4 Photolithography . . . . .	50
3.4.1 Photomask design . . . . .	53
3.5 Fabrication results . . . . .	56

---

3.5.1	M-lines characterization . . . . .	58
3.6	Polishing . . . . .	61
<b>4</b>	<b>Characterization techniques</b>	<b>65</b>
4.1	Introduction . . . . .	65
4.2	Measuring attenuation, effective group index and mode size . . . . .	65
4.3	Experimental setup . . . . .	67
4.3.1	Loss measurements . . . . .	68
4.3.2	Group index and dispersion measurements . . . . .	71
4.3.3	Mode size measurements . . . . .	75
4.4	Results . . . . .	77
<b>5</b>	<b>Segmented Waveguide Taper</b>	<b>83</b>
5.1	Introduction . . . . .	83
5.2	Numerical design of the taper . . . . .	84
5.2.1	Numerical modelling of Lithium Niobate waveguides . . . . .	85
5.2.2	Segmented waveguide design . . . . .	89
5.2.3	Taper design . . . . .	93
5.3	Device Fabrication . . . . .	97
5.4	Experimental setup . . . . .	97
5.5	Results . . . . .	98
5.6	Tapers in quantum relay . . . . .	101
<b>6</b>	<b>Segmented waveguide mode filter</b>	<b>105</b>
6.1	Introduction . . . . .	105
6.2	Mode filter operation . . . . .	105
6.3	Coupled Mode Theory for segmented waveguide mode filters . . . . .	107
6.4	Experimental results . . . . .	112
	<b>Conclusions</b>	<b>120</b>
	<b>Author's references</b>	<b>124</b>
	<b>Bibliography</b>	<b>126</b>

# Foreword

Before starting my thesis report, I would like to gratefully acknowledge the French-Italian University (<http://www.universita-italo-francese.org/>) for providing a Vinci Program fellowship which allowed this work in the framework of a co-tutored PhD activity developed at DEIS (Dipartimento di Elettronica Informatica e Sistemistica) of the University of Bologna, Italy, and at LPMC (Laboratoire de Physique de la Matière Condensée) of the University of Nice-Sophia Antipolis, France.

Daide Castaldini



# Introduction

After their first demonstration, occurred in the first seventies, optical telecommunications experienced a very rapid evolution, which has allowed dramatic changes not only in the telecommunication networks [1], but also in the services which they allow to provide to the final users.

The effort which has generated so rapid improvements has been twofold and does not seem concluded yet. From one side, new and then expensive technologies have been developed. Such technologies made available, for example, sources and detectors operating at always longer wavelengths, to take advantage of lower absorption losses of silica fibers, optical amplifiers, to allow transoceanic links with less repeaters, high speed modulators, to modulate directly the optical signal, Wavelength Division Multiplexing (WDM) systems [2], to transmit many independent channels on the same fiber and then increase the overall bandwidth. Research is not concluded, anyway, as there are still some bottlenecks which should be eliminated. For example, a cost effective way to perform all optical wavelength conversion or switching and routing operations without high-speed electronic data processing which requires opto-electrical and electro-optical conversions has not yet been found. To this purpose new components, for example based on non linear effects [3], are under investigation.

But it must also be acknowledged that the attempts to advance technology beyond its present limits are not the only challenge researchers have to face. The widespread application of optical technologies, in fact, has made cost reduction and ease of operation an equally important issue. In view of a general system optimization, also the design of basic elements should then be reconsidered. A typical example is device pigtailling. Low loss connection of an optical fiber to an integrated optical waveguide is a critical operation which requires time consuming alignment procedures and expensive micropositioning systems. However, for mass production, an easy operation with low positioning tolerances should be done to reduce cost and time.

Coupling does not only introduce loss problems. In non linear optics and namely in frequency conversion experiments, for example, waveguides which are monomode at longer wavelengths are generally multimode at shorter ones [4]. The presence of higher order modes reduces the process efficiency. In these cases, it would then be important that the field coming from a shorter wavelength device could be trans-

formed into the field of the long wavelength waveguide filtering higher order modes to avoid the drawbacks caused by their presence.

It is also worth to be noticed that the set up of new kind of transmission systems and the efficient solution of basic problems may not be independent. For example, in transmission systems exploiting quantum properties of photons [5], allowing a new kind of information cryptography [6] and then attracting as they seem a good solution to the privacy problems, loss reductions can be obtained only by optimizing all the component as bits are associated to single photons (Qbit), which then cannot be amplified with classical amplifiers as, in this case, all the information would be lost.

The simple examples mentioned before show how the quest for new and simple optical devices has not yet reached its end. Instead of using time consuming operations or huge technological efforts, a careful rethinking of the devices, exploiting new structures or physical principles seems then the way to follow.

This thesis tackles the problem of conceiving, designing and realizing new devices to solve the basic problem of obtaining low loss and efficient device coupling. To this purpose we considered the so called *segmented waveguides*. They are waveguides with longitudinal variations of their refractive index. These variations can be not only periodic, as it happens in gratings, or, more generally, in the so called Photonic Crystals [7], but can also be suitably tailored. The versatility provided by their many degrees of freedom has suggested us to investigate if they could be a way to fabricate low loss couplers and mode filters.

This study has been carried out in all the steps necessary to demonstrate devices operation, starting from their design, exploiting theoretical features of these components also using suitable numerical techniques, through their fabrication and performing also their characterization. The material chosen for the realization is Lithium Niobate ( $LiNbO_3$ ), which is interesting for its low losses at the standard telecommunications wavelengths and its good non linear as well as good electro-optics properties. We have then realized a setup suitable to evaluate the performances of the realized devices and compare them with the numerical predictions. Coupling losses reduction and mode filtering will be the particular examples in which the use of segmented waveguides will be proposed as a technologically simple and efficient solution to obtain the desired result to improve performances.

In chapter 1, the properties of the segmented waveguides will be studied first, introducing general principles with simple 1D models, and extending them to the more interesting cases of slab and channel waveguides. In chapter 2, numerical tools developed to model segmented waveguides in their 3D general structure will be introduced. After their design, segmented waveguide based devices have been realized starting from mask preparation up to device fabrication and characterization. Fabrication techniques will be described in chapter 3, while in chapter 4 the experimental set up used for device characterization will be described. The measurement apparatus is an all-in-one set up conceived to evaluate not only propagation losses or

guided mode size but also effective group index and dispersion for both integrated optical waveguides and optical fibers. In chapter 5 the results obtained for tapers characterization will be described showing that segmented waveguides allow realization of couplers with coupling losses reduced by up to 0.78 dB. These devices have also been successfully introduced, with similar performances, in a complex device for quantum communication like a quantum relay. In chapter 6 we will report results concerning a modal filter designed to operate at the wavelength  $\lambda = 840 \text{ nm}$ . In particular it will be described the design of the two tapers present in this component in order to provide a fundamental mode transformation without the introduction of higher order modes. Finally conclusions will be drawn.



# 1

## Segmented structures

### 1.1 Introduction

In this chapter, the characteristics of electromagnetic field propagation in waveguides with longitudinal changes of the refractive index will be described. The general features of these structures will be introduced starting from the case of *periodically segmented waveguides*, i.e. structures in which such changes are longitudinally periodic. The very simple case of 1D periodic structures will be preliminarily used to determine analytically their dispersion curves and different possible operation regimes. It will also be shown that many properties of these structures can be determined also studying an equivalent continuous structure. The obtained results will then be extended to 2D and 3D structures such as integrated optical slab or channel waveguides. In the last part of the chapter we will relax the constraint of regular periodicity and introduce the more general concept of *segmented waveguide* where period and other device parameters can be varied longitudinally. In this case the properties of periodic waveguides will be considered valid locally with the same idea leading to define local normal modes in longitudinally varying continuous structures. After reminding some well known applications of these structures, the possible uses of segmented waveguides studied in this thesis will be introduced.

### 1.2 Propagation in periodic media

In order to show the properties of an electromagnetic field propagating through a periodic medium, a simple 1D model can be used [8, 9, 10, 11]. The structure is constituted by the regular repetition, with period  $P$  of layers alternatively with high (width equal to  $a$ ) and low (width equal to  $b$ ) refractive indices, with infinite dimensions in the two  $x$  and  $y$  directions orthogonal to  $z$ , as schematically illustrated in 1.1.

One of the most important parameters for the characterization of any optical

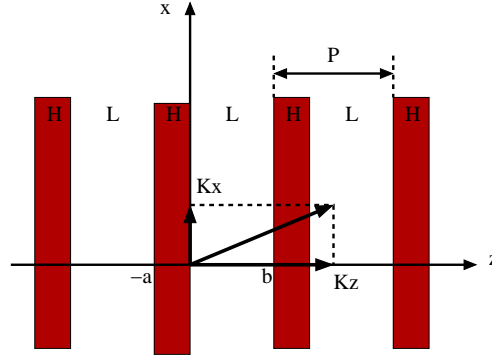


Figure 1.1: Ideal 1D periodic structure, consisting of alternating layers of low and high index.  $P$  is the period of the structure,  $a$  and  $b$  are respectively the length of the high (H) and of the low (L) refractive index segments.

structure is the so called *dispersion function*. Dispersion describes, in fact, the frequency (or wavelength) dependence of the wave speed. For the structure of figure 1.1, the dispersion functions depend on the incident field polarization. In particular for TE and TM polarization of an incident plane wave the following equations hold respectively [11, 10]:

$$\cos(Kb) \cos(Qa) - \frac{Q^2 + K^2}{2QK} \sin(Kb) \sin(Qa) = \cos(k_z P) \quad (1.1)$$

$$\cos(Kb) \cos(Qa) - \frac{\epsilon_L^2 Q^2 + \epsilon_H^2 K^2}{2\epsilon_L \epsilon_H QK} \sin(Kb) \sin(Qa) = \cos(k_z P) \quad (1.2)$$

where

$$K^2 = \omega^2 \mu_0 \epsilon_L - k_x^2 - k_y^2 \quad (1.3)$$

$$Q^2 = \omega^2 \mu_0 \epsilon_H - k_x^2 - k_y^2 \quad (1.4)$$

are the propagation constants along the longitudinal direction  $z$ . If propagation occurs exactly along the longitudinal direction ( $z$ ), the two propagation vectors  $k_x$  and  $k_y$  vanish and the dispersion functions for TE and TM modes degenerate.

In figure 1.2 dispersion curves are reported in a normalized reference plane where  $\Omega$  is the normalized frequency and  $\kappa$  the normalized wavevector, defined as:

$$\Omega = \frac{P}{\lambda_0} \quad (1.5)$$

$$\kappa = k_z P. \quad (1.6)$$

being  $\lambda_0$  the wavelength in vacuum. The dispersion diagrams of these structures are similar to that reported in figure 1.2. There are infinite dispersion curves along the  $\Omega$  axis. They also repeat periodically along the  $\kappa$  axis. Curves are separated in frequency and form an infinite series of bands. For each of them it is possible to distinguish three different working regions:

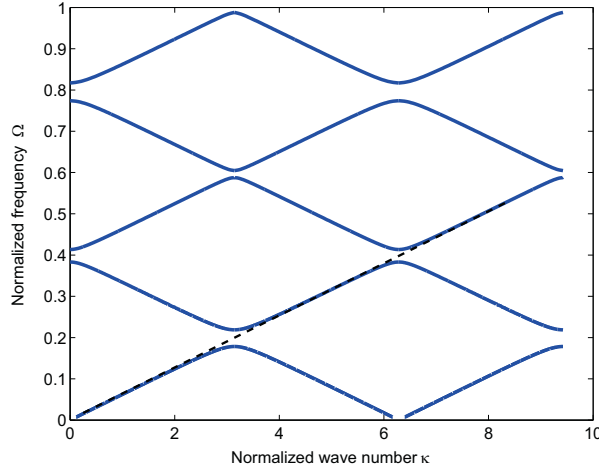


Figure 1.2: Dispersion curves for  $\epsilon_L = 5\epsilon_0$ ,  $\epsilon_H = 10\epsilon_0$ ,  $a = 1.5\mu m$  and  $b = 5\mu m$  for degenerate TE and TM polarizations.

- **Band Edge:** for values of the normalized wavevector  $\kappa$  corresponding to  $\pi + m\pi$  (where  $m$  is an integer constant) the dispersion function exhibits the so called *band edge*. The gap between two band edges of different adjacent bands is the so called *band gap*. Exciting the structure with a field at a normalized frequency inside a band gap the propagation vector  $k_z$  becomes imaginary [9]. This means that the field can not propagate through the structure but is reflected. Bragg gratings work in this region.
- **Slow light region:** close to the band gap, the dispersion curves are strongly non linear. In this region, the propagating plane waves are characterized by slow group velocity ( $v_g$ ) because of the small slope of the dispersion curves ( $v_g = \frac{\partial \omega}{\partial k_z}$ ).
- **Linear region:** this third zone is the linear one. In such regime the structure behaves like an homogeneous medium from a dispersive point of view. In the rest of the thesis we will be mainly interested in this region. In the next paragraph this idea will be developed with more mathematical detail to demonstrate the very important *theorem of the equivalent waveguide*.

### 1.3 Equivalence theorem for periodic media

As said before, for frequencies far away from the band gap, the dispersion curve of a periodic structure is almost linear, as it happens for an homogeneous medium in the limit of neglecting material dispersion. In this section we then evaluate the terms of this equivalence. We consider  $(\Omega_n, \kappa_n)$ , the mid point of the linear part of

the dispersion curve, as working point. With reference to figure 1.2 the normalized wavevector  $\kappa_n$  is:

$$\kappa_n = \frac{\pi}{2} + n\pi, n = 0, 1, 2, \dots \quad (1.7)$$

Replacing 1.7 in equation 1.1 or in 1.2 and noting that:

$$\cos(k_z P) = \cos(\kappa_n) = \cos[(n + 1/2)\pi] = 0 \quad (1.8)$$

the dispersion relationship 1.1 or 1.2 with  $k_x = k_y = 0$  reduces to:

$$\tan(Kb) \tan(Qa) = \frac{2QK}{Q^2 + K^2}. \quad (1.9)$$

This is a transcendental equation and an analytical solution can be obtained only after some approximations. First of all, observing equations 1.3 and 1.4 we can write:

$$Q = K + \Delta \quad (1.10)$$

where  $\Delta$  is related to the difference between  $\epsilon_L$  and  $\epsilon_H$ . Replacing 1.10 in the right part of equation 1.9 and assuming that  $\Delta/K \ll 1$ , it holds:

$$\frac{2QK}{Q^2 + K^2} \approx 1 - \frac{\Delta^2}{2K^2} \quad (1.11)$$

Neglecting second order infinitesimal terms in  $\Delta/K$ , equation 1.9 can be approximated by:

$$\tan(Kb) \tan(Qa) \approx 1. \quad (1.12)$$

The solution of equation 1.12 can be obtained using the identity:

$$\tan[(m \pm 1/4)\pi - \xi] \tan[(m \pm 1/4)\pi + \xi] = 1 \quad (1.13)$$

where  $m$  is an integer and  $\xi$  is arbitrary. Comparing equation 1.12 with the previous identity, one finds that:

$$\begin{aligned} Kb &= (m \pm 1/4)\pi - \xi \\ Qa &= (m \pm 1/4)\pi + \xi. \end{aligned} \quad (1.14)$$

Adding  $Kb$  to  $Qa$  we get:

$$\begin{aligned} Kb + Qa &= (m \pm 1/4)\pi - \xi + (m \pm 1/4)\pi + \xi = \\ &= 2(m \pm 1/4)\pi. \end{aligned} \quad (1.15)$$

Replacing the definitions of  $K$  and  $Q$  (1.3, 1.4) in 1.15 we obtain:

$$\omega\sqrt{\mu_0} (b\sqrt{\epsilon_L} + a\sqrt{\epsilon_H}) = 2(m \pm 1/4)\pi. \quad (1.16)$$

	$m = -1$	$m = 0$	$m = 1$	$m = 2$
$2(m + 1/4)\pi$	$-(3/2)\pi$	$(1/2)\pi$	$(5/2)\pi$	$(9/2)\pi$
$2(m - 1/4)\pi$	$-(5/2)\pi$	$-(1/2)\pi$	$(3/2)\pi$	$(7/2)\pi$
	$n = -1$	$n = 0$	$n = 1$	$n = 2$
$(n + 1/2)\pi$	$-(1/2)\pi$	$(1/2)\pi$	$(3/2)\pi$	$(5/2)\pi$

Table 1.1: Sequence of the two equivalent expressions:  $(m \pm 1/4)\pi$  and  $(n + 1/2)\pi$  for  $m$  and  $n$  integers.

For integer values of  $m$ , the sequence  $2(m \pm 1/4)\pi$  (developed in table 1.1) is equivalent to the sequence  $(n + 1/2)\pi$  with integers values of  $n$ . We can then write equation 1.16 as:

$$\omega\sqrt{\mu_0}(b\sqrt{\epsilon_L} + a\sqrt{\epsilon_H}) = (n + 1/2)\pi. \quad (1.17)$$

Dividing both sides of 1.17 by  $a + b = P$  we obtain:

$$\frac{\omega(bn_L + an_H)}{c(a + b)} = \frac{(n + 1/2)\pi}{a + b} \quad (1.18)$$

where  $n_L$  and  $n_H$  are the refractive indices of the two segments and  $c = 1/\sqrt{\mu_0\epsilon_0}$  is the light velocity in the vacuum.

Replacing the definition of  $\kappa_n$  we obtain finally:

$$\frac{\omega(bn_L + an_H)}{c(a + b)} = \frac{\kappa_n}{P} = k_z. \quad (1.19)$$

One can read this as the dispersion function of an homogeneous medium with refractive index  $n_{eq}$ :

$$\omega = \frac{c}{n_{eq}}k_z \quad (1.20)$$

having defined

$$\begin{aligned} n_{eq} &= \frac{(bn_L + an_H)}{a + b} = \frac{(bn_L + an_H)}{P} = \\ &= \frac{b}{P}n_L + \frac{a}{P}n_H. \end{aligned} \quad (1.21)$$

Moreover, defining the duty cycle  $DC$  as the ratio between the length  $a$  of the higher index segment and the period  $P$ , we can write:

$$\begin{aligned} n_{eq} &= (1 - DC)n_L + DCn_H = n_L - DCn_L + DCn_H = \\ &= n_L + (n_H - n_L)DC. \end{aligned} \quad (1.22)$$

In conclusion we have shown that in the linear zone of the dispersion curve a periodic medium is equivalent to an homogeneous one with refractive index equal to

the average of the two refractive indexes  $n_L$  and  $n_H$  weighed by the  $DC$ . This dependency of the equivalent index with a parameter like the  $DC$  is very interesting from the technological point of view. The refractive index is, in general, a parameter fixed by the technology and is then very hard to change. The  $DC$ , on the contrary, is a parameter fixed by the design of the structure and is then relatively simple to modify. This then allows to modify easily the equivalent index of the structure without changing the fabrication technology.

## 1.4 Periodically segmented waveguides

Up to now, the considered structure is infinite in the transversal directions  $x$  and  $y$ . This type of structure has a limited range of applications (lens antireflection coatings, for example) but has no interest for integrated optics as the field is not confined. We will then consider now structures that arrange the periodicity of the refractive index, in the propagation direction, and also allow transversal confinement of the field. Two examples of these structures are respectively the *periodically segmented slab* (in the following also denoted as *periodic slab*) and the *periodically segmented waveguide* (in the following also denoted as *periodic waveguide*) whose structures are sketched in figure 1.3. For the periodic slab, the confinement of the

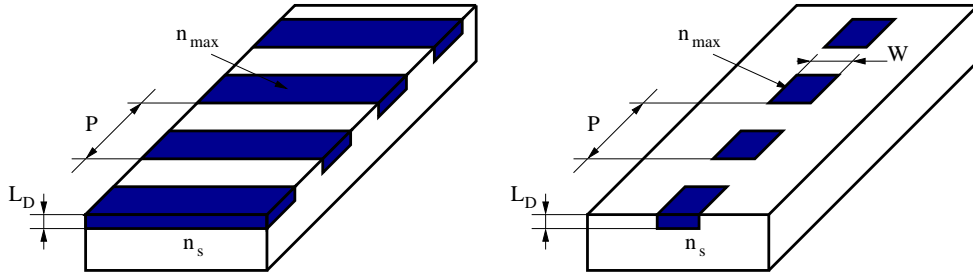


Figure 1.3: Representation of a periodic slab (left part of the figure) and of a periodic waveguide (right part).

field is only in one direction and is guaranteed by the total reflection at the film-substrate interface, while, for the periodic waveguide, confinement occurs in both transversal directions.

The electromagnetic field propagating through a periodic slab or waveguide still obeys the equivalent waveguide theorem. Validity of equation 1.22 also for confined period structures has been confirmed by many publications [12, 13, 14, 15]. These results confirm that for wavelengths far away from a band gap, a periodic waveguide is equivalent to a continuous one with the same width and depth but with refractive index equal to:

$$n_{eq} = n_s + DC \Delta n_{max} \quad (1.23)$$

where  $\Delta n_{max}$  and  $n_s$  are respectively the maximum and the substrate refractive index of the periodic waveguide. The use of periodic waveguides allows then to artificially tune the refractive index of the waveguide without changing dopants or technology.

The presence of longitudinal discontinuities in the waveguides, however, also introduces propagation losses as the guided mode couples to radiation modes. This point is important and merits to be investigated with some more detail.

## 1.5 Propagation losses in periodically segmented waveguides

As just said, it is reasonable to expect that, passing from a continuous waveguide to a periodic one, losses appear and increase for decreasing duty cycle as the fraction of high index material in the period, which allows field confinement, is reduced. In the low index zone, the field is not confined and is then coupled to radiation modes. The field then spreads and when it reaches the next higher index piece of waveguide it can not be totally coupled back to the guided mode. The smaller is the guiding segment with respect to the period, the larger will be then the expected losses.

Amazingly, this explanation turns out to be valid only for duty cycles from 0.5 to 1. Further reduction of the duty cycle, in fact, leads to a maximum but then losses are again reduced approaching  $DC = 0$ . This loss reduction is limited by the presence of the cutoff wavelength, which limits the possible  $DC$  reduction.

This behavior has been confirmed both numerically [16, 14] and experimentally [17, 18]. An explanation of the phenomenon is developed in the following. The electromagnetic field in the periodic core can be expressed as a combination of the so called spatial harmonics, i.e. solutions with longitudinal propagation constant given by:

$$\beta + nG, \quad n = \pm 0, 1, 2, \dots; \quad G = \frac{2\pi}{P}. \quad (1.24)$$

In cover and substrate, only the plane waves with the same longitudinal propagation constant can contribute to the field structure and only some of them significantly contribute to the overall field. If the transversal propagation constant of these planes waves has a small propagation factor in the transversal direction, the mode is still practically confined. More details on this can be found, for example, in [14]. Computational result of propagating losses as a function of  $DC$  is shown in figure 1.4 for a slab waveguide. The attenuation peak at  $DC$  slightly larger than 0.9 is due to Bragg reflection in the structure. The possibility of having small radiation losses allows then the use of segmented waveguide as standard component in integrated optics.

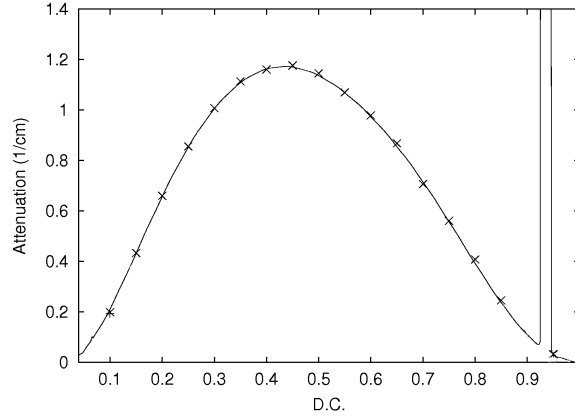


Figure 1.4: Field attenuation versus  $DC$  in periodic waveguide, from Fogli et al. [14].

## 1.6 Cutoff properties of periodically segmented waveguides

A further interesting properties of periodic waveguides concerns the dependence of the cutoff wavelength on the  $DC$  [19]. Cutoff is the condition for which the effective index of the propagating mode becomes equal to the substrate index. Such condition implies that the mode is no longer confined but is spread out in the substrate. Fixing the transversal index distribution in a continuous waveguide (CWG) the cutoff condition depends only on wavelength.

In order to understand how the characteristics of a periodic waveguide can control the cutoff wavelength, we consider the easier case of a periodic slab and then we extend the result in the case of a periodic waveguide.

For a slab waveguide the normalized frequency [20] is defined as:

$$V = L_D \frac{2\pi}{\lambda_0} \sqrt{(n_{max}^2 - n_s^2)} \quad (1.25)$$

where  $n_{max}$  is the maximum refractive index of the slab waveguide,  $n_s$  is the substrate refractive index and  $L_D$  is the depth of the waveguide. The expression 1.25 can be used for both the step index [21, 22] and the graded index slab [20]. For the diffused slab waveguide the only assumption is that the index profile decreases monotonically from the maximum surface value to the substrate one. At cutoff, the normalized frequency  $V$  depends only on the asymmetry parameter  $a$  [22] defined as:

$$a = \frac{n_s^2 - n_c^2}{n_{max}^2 - n_s^2} \quad (1.26)$$

where  $n_c$  is the cladding refractive index. Assuming  $n_{max} > n_s > n_c$ , the parameter  $a$  can vary between 0, for the perfect symmetric structures ( $n_s = n_c$ ) and infinity,

for structures with strong asymmetries ( $n_s \neq n_c$  and  $n_s \rightarrow n_{max}$ ). In the case of integrated optical devices the cladding is generally air and the structures present strong asymmetries. This means that  $a$  is almost infinity and for all the devices of this type the value of  $V$  is the same. In particular it is possible to say that the normalized frequency, at cutoff, is the same for a slab waveguide (CWG, continuous waveguide) and for a periodic slab (PWG, periodic waveguide):

$$V_{PWG}^{cutoff} = V_{CWG}^{cutoff} \quad (1.27)$$

As a consequence, changing the  $DC$  of a periodic waveguide, the cutoff wavelength is modified too. This is a consequence of the equivalence theorem and of equation 1.27. Writing  $n_{max}$  as:

$$n_{max} = n_s + \Delta n \quad (1.28)$$

and assuming a small index change:

$$\Delta n^2 \ll 2n_s \Delta n \quad (1.29)$$

we obtain:

$$(n_{max}^2 - n_s^2) \approx 2n_s \Delta n. \quad (1.30)$$

Replacing approximation 1.30 in the definition of the normalized frequency 1.25, we obtain the following expression for  $V^2$ :

$$V^2 = L_D^2 \left( \frac{2\pi}{\lambda_0} \right)^2 (n_{max}^2 - n_s^2) \approx L_D^2 \left( \frac{2\pi}{\lambda_0} \right)^2 (2n_s \Delta n). \quad (1.31)$$

Equation 1.31 can be evaluated in the case of a continuous slab and a periodic slab, taking into account the dispersive behavior in frequency of  $n_s$  and  $\delta n$ . For the continuous slab it holds:

$$(V_{CWG}^{cutoff})^2 = L_D^2 \left( \frac{2\pi}{\lambda_{CWG}} \right)^2 2n_s(\lambda_{CWG}) \Delta n(\lambda_{CWG}) \quad (1.32)$$

where  $\lambda_{CWG}$  is the cutoff wavelength of the continuous slab. For the periodic slab it holds:

$$(V_{PWG}^{cutoff})^2 = L_D^2 \left( \frac{2\pi}{\lambda_{PWG}} \right)^2 2n_s(\lambda_{PWG}) \Delta n_{eq}(\lambda_{PWG}) \quad (1.33)$$

where  $\lambda_{PWG}$  is the cutoff wavelength of the periodic slab and  $\Delta n_{eq}(\lambda_{PWG})$  can be expressed using the relation of the equivalent waveguide 1.23 as:

$$\Delta n_{eq}(\lambda_{PWG}) = DC \Delta n(\lambda_{PWG}). \quad (1.34)$$

Using 1.34, 1.27, 1.32 and 1.33 we can write:

$$\frac{\lambda_{PWG}^2 n_s(\lambda_{CWG}) \Delta n(\lambda_{CWG})}{\lambda_{CWG}^2 n_s(\lambda_{PWG}) \Delta n(\lambda_{PWG})} = DC. \quad (1.35)$$

The terms  $n_s(\lambda_{CWG})/n_s(\lambda_{PWG})$  and  $\Delta n(\lambda_{CWG})/\Delta n(\lambda_{PWG})$  on the left side of equation 1.35 are related to the dispersive behavior of the materials. Neglecting material dispersion, equation 1.35 can be simplified to:

$$DC = \frac{\lambda_{PWG}^2}{\lambda_{CWG}^2}. \quad (1.36)$$

Figure 1.5 shows a plot of the cutoff wavelength versus the  $DC$  for a periodic

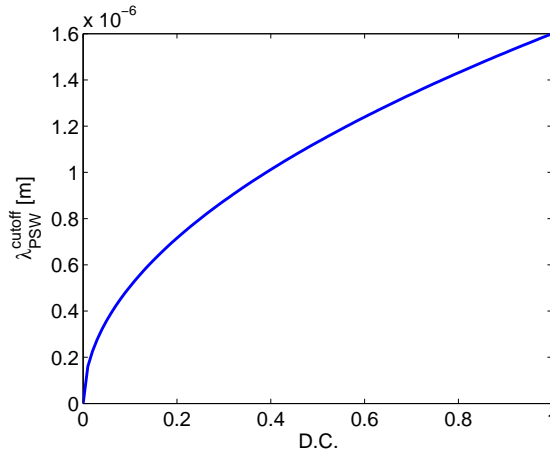


Figure 1.5: Cutoff wavelength as a function of the duty cycle for a periodic slab with  $n_{max} = 2.2443$ ,  $n_s = 2.1897$ ,  $n_c = 1$  and  $L_d = 0.67\mu m$ .

slab. Another way to visualize the result given by 1.36 is reported in figure 1.6, where the cutoff wavelength of the periodic slab waveguide can be expressed, for a fixed  $DC$ , as a function of the cutoff wavelength of the continuous slab waveguide. Noting that a continuous waveguide is a segmented waveguide with  $DC = 1$ , we can rewrite equation 1.35 replacing the continuous slab waveguide parameters with those of another periodic slab waveguide. To distinguish the two waveguides, suffix 1 will be used for parameters of the original PWG while suffix 2 will indicate the parameters of the newly introduced one. Equation 1.35 becomes then:

$$\frac{\lambda_{PWG}^2(DC_1)n_s(\lambda_{PWG}(DC_2))\Delta n(\lambda_{PWG}(DC_2))}{\lambda_{PWG}^2(DC_2)n_s(\lambda_{PWG}(DC_1))\Delta n(\lambda_{PWG}(DC_1))} = \frac{DC_1}{DC_2}. \quad (1.37)$$

Neglecting dispersion we obtain:

$$\frac{DC_1}{DC_2} = \frac{\lambda_{PWG}^2(DC_1)}{\lambda_{PWG}^2(DC_2)}. \quad (1.38)$$

This result can be generalized in the case of channel waveguide using the relation between the normalized frequency  $V$  for the slab waveguide and the normalized

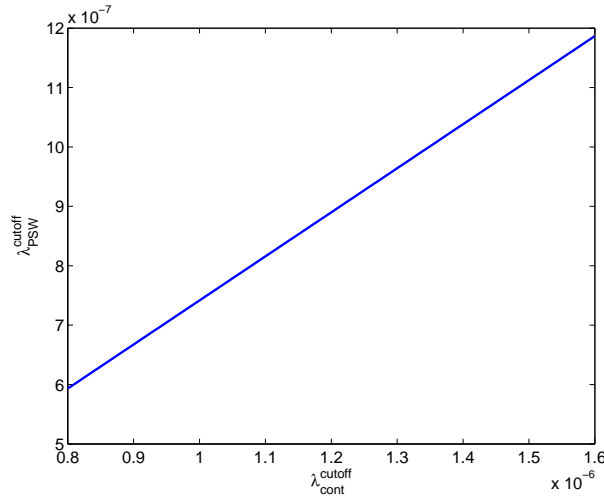


Figure 1.6: Periodic waveguide cutoff wavelength versus the cutoff wavelength of a continuous waveguide for a fixed  $DC$  equal to 0.55.

frequency  $V^c$  for a channel waveguide [23].

$$V^c = Vb \frac{W}{L_D} \quad (1.39)$$

where  $W$  is the width of the channel waveguide and  $b$  is the normalized propagation constant [23]. Equation 1.39 suggests that for a channel waveguide with fixed width and depth, the parameter  $V^c$  is a function of only  $V$  and  $b$ . Being  $b$  a function of  $V$  it is then possible to deduce that  $V^c$  is directly related to  $V$ . At cutoff,  $V^c$  is then the same for a periodic and a continuous waveguide. All the results obtained for slab waveguides can then be extended to channel waveguides.

## 1.7 Segmented waveguides

Up to now, we have discussed the properties of periodically segmented waveguides. It is anyway possible to imagine to vary longitudinally any of the parameters describing one of the features of the periodic waveguide: the period  $P$ , the duty cycle  $DC$  and also the lateral width of the pieces of waveguides forming the structure. In this case only numerical approaches can be used to determine the electromagnetic behavior of these structures as the propagation constant  $\beta$  is no longer constant, but varies with  $z$  and the *ansatz*  $E(x, y, z) = E(x, y) e^{-j\beta z}$  cannot be set to determine the modes of the structure.

It is anyway possible to assume that, locally, the guided field is the same for both a structure with longitudinal features equal anywhere and those of the considered section. This is not rigorous, but it is anyway useful, mainly when longitudinal

changes are “slow” with respect to the wavelength, so that one can suppose that there are no significant changes in the propagation constant or important reflections [24]. We will refer to these structures simply denoting them as *segmented*.

This conceptually simple extension opens a lot of possibilities to imagine new types of structures, but also sets the huge problem of designing a structure optimizing many parameters at the same time. This task can in effect be tackled only in a two step process: the former conceiving the structure with the desired properties using simple, also analytical, approaches; the latter refining the design using 2D or 3D numerical methods, and, in case, iterating the process until the desired device performances are envisaged. This allows to minimize the number of prototypes which must be fabricated. This was in effect the way of working used in this work.

Before entering into detailed descriptions of the realized devices, it is anyway worthwhile to provide a brief summary of the most important applications of (periodically) segmented structures in optical transmission systems and then provide a general description of the problems to be solved by this kind of devices.

Segmented waveguides have been widely used both for linear and non linear applications such as Bragg reflectors, dispersion compensators, sensors, wavelength converters, frequency generation, etc. More details and references can anyway be found in many text books or papers, such as, for example [25, 26, 27, 28, 29, 30, 31].

We now focus our attention to the two particular examples which will have been deeply investigated in this thesis work. They operate in the almost linear part of the dispersion characteristic (figure 1.2) and then do not present any Bragg reflection effect. This way, the use of the local mode approximation will be allowed.

### 1.7.1 Mode transformers: Taper

The mode transformers or tapers are devices able to couple two different optical waveguides allowing maximum energy transfer. Coupling two different waveguides, in fact, induces losses which can be very important. The first cause of loss is related to Fresnel reflections, due to the refractive index mismatch of the two waveguides. The second contribution to the coupling losses is related to the different mode shape in the two structures. If the two modes are different, continuity conditions at the interface induce coupling also to the radiating modes or to higher order modes, if they exist. This introduces losses as well.

Fresnel losses can be reduced using proper index matching materials.

To minimize shape mismatch losses, a mode transformer should be placed (as schematically shown in figure 1.7) between the two structures to be coupled, A and B. The three goals of a taper are: reduction of the interface reflections, improvement of the mode overlap at the interfaces and reduction of the mode transformation losses. The most interesting application of the taper is coupling optimization between an integrated optical waveguide and an external optical fiber as these two guides have large structural differences. In these cases the presence of a taper between waveguide

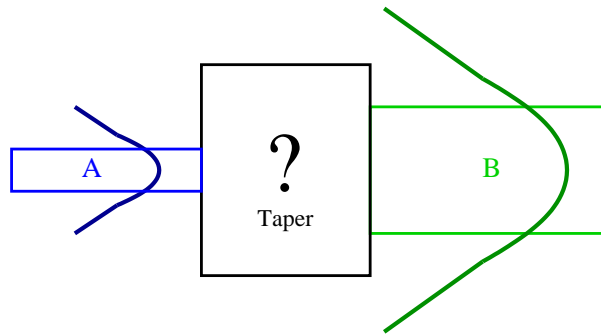


Figure 1.7: Schematic of the taper insertion between two different optical structures.

and fiber turns out favorable.

In order to realize a taper, different solutions can be envisaged, depending on the specific requirements and the available technology. The first idea that can be proposed in order to increase the propagating mode size in a waveguide is based on a gradual increase of the waveguide size. An example of this type of structure is shown in figure 1.8. The advantage of this kind of taper is the fabrication simplicity.

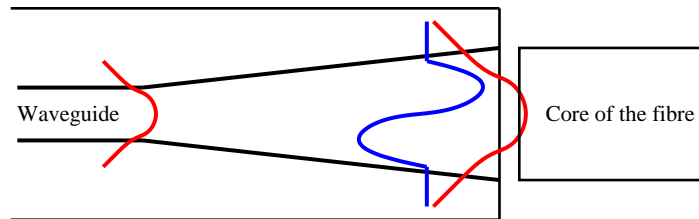


Figure 1.8: Schematic representation of a taper obtained by increasing the width of the waveguide in the propagation direction.

But a taper of this type it affected by some problems. First of all it is not always true that increasing the size of an optical waveguide also induces an increase of the guided mode size. Two phenomena exist, in fact, when the dimension of a waveguide is increased. The first phenomenon is the increase of the mode size related to the fact that the guiding structure is larger, the second is the increase of the effective index of the mode, that induces, on the contrary, a better confinement of the field.

The presence of these two effects has the consequence that the mode size can not change monotonically with the waveguide dimension, but shows a minimum as sketched in figure 1.9. For a fixed fabrication technology an optical waveguide can be on the left or on the right of the characteristic curve minimum. Increasing the waveguide section when the initial operating condition is on the right of the minimum means in effect an increase of the mode size. But, if the initial operating

condition belongs to the left part of the curve, the increase of the waveguide size causes an unwanted reduction of the mode size.

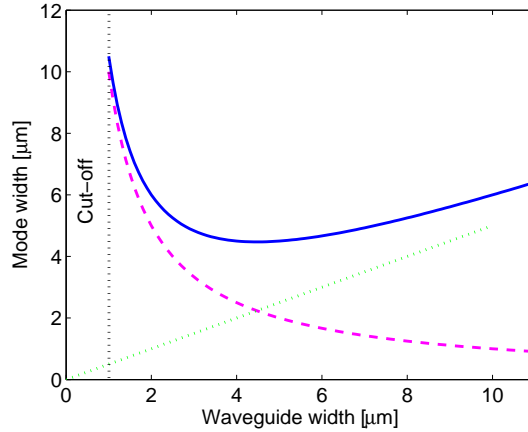


Figure 1.9: Representation of the fundamental mode width in a generic optical waveguide as a function of the waveguide width (continuous line) resulting on the contribution of the effective index (dashed line) and waveguide size (dotted line).

Another problem that occurs in this type of taper is that often, it is not technologically easy or even possible to modify the waveguide depth. This causes a strong ellipticity of the waveguide mode resulting completely unsatisfactory from the point of view of the overlap with the fundamental mode of a circular fiber. The last drawback of this solution is that increasing the waveguide size at a fixed wavelength the structure can become multimode, which is a condition obviously to be avoided.

A second kind of taper is shown in figure 1.10. A reduction of the waveguide size can in fact induce a mode size increase as suggested in figure 1.9.

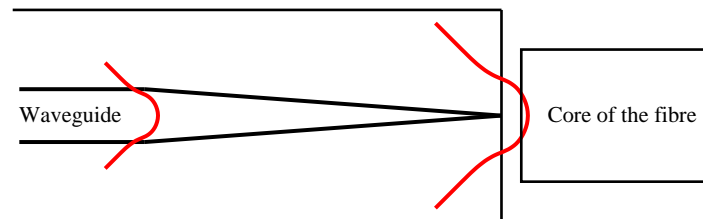


Figure 1.10: Schematic representation of a taper obtained reducing the width of the waveguide in the propagation direction. The mode size widens approaching the cutoff condition.

Reducing the size of the waveguide, in fact, induces a reduction of the effective index and, as a consequence, the mode turns out to be less confined. The advantages

of this type of taper are due to the fact that an increase of both the lateral and vertical mode size can be obtained and that the structure can not become multimode. The drawback are related to technological problems. The only parameter which can be easily controlled during fabrication is the width of the waveguide and this is the only parameter which can be used to modify the mode size in both directions. This makes the design of this taper critical. Moreover curves at the left of the minimum of figure 1.9 are usually very steep as operating conditions approach cutoff. This means that a small imprecision on the determination of the width of the taper can cause large changes of the mode size.

In this work we have investigated the possibility to use segmented waveguides [32] to provide a third way to fabricate tapers. Expected advantages are fabrication simplicity and the possibility to eliminate the problems evidenced for the previously described structures [33].

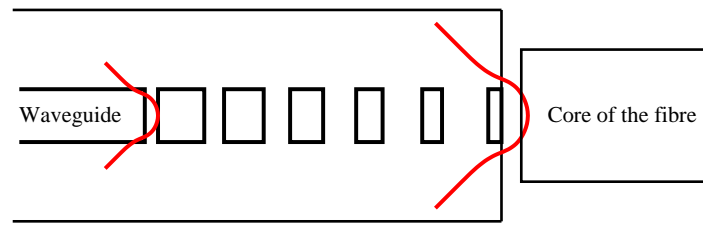


Figure 1.11: Schematic representation of a segmented waveguide taper obtained with a graded variation of the  $DC$  in the propagation direction.

The structure of this segmented waveguide taper is shown in figure 1.11. The continuous waveguide becomes segmented with variable duty cycle along the propagation direction. Once reached the desired duty cycle the mode can be stabilized with a periodically segmented waveguide. From the equivalent waveguide theorem this structure can be analyzed as a continuous waveguide with refractive index gradually reduced along the longitudinal direction. As a result the mode size is therefore increased both in width and depth. The final mode shape depends on the combination of the final duty cycle and the waveguide width. The possibility of controlling the mode size through two independent parameters is an important feature which provides less critical design of the structures, with respect to the previously presented solutions. Moreover, no unwanted higher order modes appear as segmentation reduces the effective index with respect to that of the continuous waveguide.

### 1.7.2 Mode filters

A mode filter is a device able to eliminate one or more higher order modes propagating in a multimode waveguide. Such operation turns out to be particularly important in non linear applications, for example in wavelength conversion. In

the case of a difference-frequency mixer, for example, a pump at frequency  $\omega_p$  is mixed with a signal with frequency  $\omega_s$  in order to generate an idler frequency  $\omega_i = \omega_p - \omega_s$ . This type of interaction is used in many applications, from the generation of particular radiation in the near infrared, to wavelength conversion for WDM systems or for single photon generation in quantum communication applications. Usually idler or signal radiations have wavelength significantly larger with respect to that of the pump. Even if the guide is monomode at the idler and signal wavelengths, it is multimode at the pump frequency. Therefore, it turns out difficult to couple in efficient way the laser radiation of the pump to the fundamental mode of the waveguide. Moreover, the unavoidable excitation of higher order modes generates undesired peaks in the fluorescence output spectrum.

Using segmented waveguides it is possible to solve also this problem. Higher order modes at the pump wavelength can in fact be filtered by simply reducing the value of the duty cycle  $DC$  of a segmented waveguide thus leading those modes to cutoff. This is shown in figure 1.12 where the effective indices of the propagating modes in the segmented waveguide are reported as a function of  $DC$ .

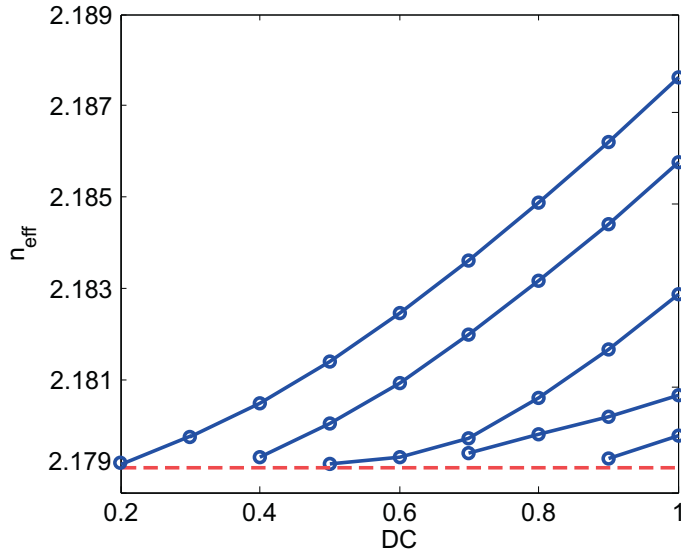


Figure 1.12: Effective index values of guided modes as a function of the  $DC$ . The substrate refractive index is  $n_s = 2.1788$  (dashed line), for effective index  $n_{eff}$  smaller than  $n_s$  the corresponding mode is at cutoff.

The waveguide considered in this example guides five modes at  $\lambda_p = 775$  nm. Reducing  $DC$ , the value of their effective indices is reduced. For values of the  $DC$  between 0.2 and 0.4 just one mode results in propagation ( $n_{eff} > n_s$ ). Taking advantage of this property, a segmented waveguide structure acting as mode filter has been proposed [34]. A schematization of this solution is shown in figure 1.13.

The input section is a segmented waveguide with constant  $DC$  determined to

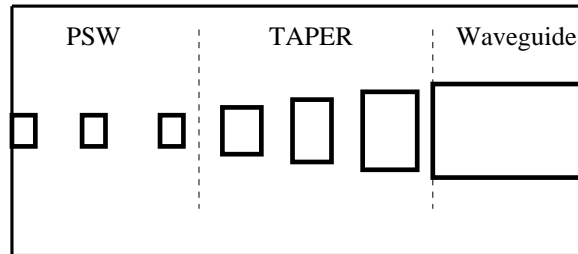


Figure 1.13: Schematization of the mode filter proposed by [34] constituted by a segmented waveguide with constant  $DC$  (PWG) and a taper which optimize the coupling with the continuous waveguide.

guarantee monomode operation for the pump and also the propagation of the signal at higher wavelength. Through the taper, the fundamental mode of the segmented waveguide is slowly transformed into the fundamental mode of the continuous waveguide. This operation must be performed accurately in order to reduce both the excitation of higher order mode and the mode transformation losses. In the case shown in figure 1.13, also the waveguide width is tapered in the propagation direction. This particular taper design is necessary to obtain large mode transformations and also to better control the ellipticity of the mode.



# 2

## Numerical methods

### 2.1 Introduction

In this chapter the main features of two numerical tools used both to design the components and analyze the experimental results comparing them with theoretical predictions will be discussed. The two algorithms solve the fundamental problems one faces when designing a component: computing both the field evolution along a longitudinally varying guide and the field which can be guided by a longitudinally invariant structure. From the mathematical point of view, the former is an *initial value problem*, while the latter is a *boundary value problem*.

The development of the source code allows to control in detail all the modelling parameters for the different devices. The choice to develop original versions of the codes instead of buying commercial ones is due to the fact that in this way we have the full control of all the introduced assumptions and a precise knowledge of the theoretical and numerical limitations.

The first technique is the so called full vectorial Finite Difference 3D Beam Propagation Method (FD-BPM)[35]. It uses a finite difference scheme to solve the Helmholtz equations in the case of unidirectional propagation of the electromagnetic field through the optical structure. The formulation originally adopted and extended for this work is based on the Helmholtz equations written for the electric field. However, numerical instability problems affecting this kind of solver have been found. To eliminate them, a 3D BPM based on the so called magnetic formulation was then developed. It solves the Helmholtz equation written for the magnetic field. In order to improve the result accuracy and to allow the study of wide-angle propagations, the paraxial approximation has been replaced by the Padé approximants in both codes. The anisotropic Perfectly Matched Layer (PML) boundary condition [36] essential to absorb outgoing radiation was also introduced.

The second numerical technique developed and discussed in this chapter allows to calculate the mode properties (shape, effective index) of  $z$ -invariant structures. It is a Mode Solver and solves the Maxwell equations by a Finite Difference technique

in the Frequency Domain (FD-FD). This tool is also used to calculate the initial conditions (input field) of the 3D BPM if a mode of the structure is to be considered.

## 2.2 3D fully vectorial Beam Propagation Method

The time domain electromagnetic field behavior in a photonic devices is described by the Maxwell equations and by the constitutive relations of the material. In a Cartesian orthogonal reference frame they can be written as:

$$\nabla \times \bar{E}(x, y, z, t) = -\frac{\partial \bar{B}(x, y, z, t)}{\partial t} \quad (2.1)$$

$$\nabla \times \bar{H}(x, y, z, t) = \frac{\partial \bar{D}(x, y, z, t)}{\partial t} + \bar{J}(x, y, z, t) \quad (2.2)$$

$$\nabla \cdot \bar{D}(x, y, z, t) = \rho(x, y, z, t) \quad (2.3)$$

$$\nabla \cdot \bar{B}(x, y, z, t) = 0 \quad (2.4)$$

where

- $\bar{E}$  and  $\bar{H}$  are the electric and magnetic field vectors
- $\bar{D}$  and  $\bar{B}$  are the electromagnetic and magnetic induction vectors
- $\bar{J}$  is the source current vector
- $\rho$  is the electric charge density
- $\bar{\epsilon}$  and  $\bar{\mu}$  are the tensors of dielectric permittivity and magnetic permeability.

Electric and magnetic induction vectors can be expressed as:

$$\bar{D}(x, y, z, t) = \bar{\epsilon}(x, y, z, \omega, |\bar{E}|) \cdot \bar{E}(x, y, z, t) \quad (2.5)$$

$$\bar{B}(x, y, z, t) = \bar{\mu}(x, y, z, \omega, |\bar{H}|) \cdot \bar{H}(x, y, z, t) \quad (2.6)$$

which set the relations between electromagnetic fields and material properties. Permittivity and permeability are represented by tensorial quantities in order to take into account anisotropic materials. They depend on the considered point  $(x, y, z)$ , the frequency  $(\omega)$  and on the electric and magnetic field intensity. In this way we can consider non homogeneous materials with both frequency dispersion and non linearity. The solution of this completely general problem is not always necessary and we can then simplify the model according to the characteristics of the considered structures.

We can first assume that the tensor  $\bar{\mu}$  is a scalar constant:

$$\mu = \mu_0 = 4\pi 10^{-7} H/m \quad (2.7)$$

while for the dielectric properties we consider a linear, non dispersive and isotropic material. In this case  $\bar{\epsilon}(x, y, z, \omega, |\bar{E}|)$  reduces to a scalar function of the point:  $\epsilon(x, y, z)$ . We can finally assume also that no charges ( $\rho = 0$ ) and no sources ( $\bar{J} = 0$ ) are present in the computational domain.

For the linearity of Maxwell equations we can consider also a stationary harmonic regime. This allows to introduce complex vectors [37]:

$$\begin{aligned}\bar{E}(x, y, z, t) &= \Re \{ \bar{E}(x, y, z) e^{j\omega t} \} \\ \bar{H}(x, y, z, t) &= \Re \{ \bar{H}(x, y, z) e^{j\omega t} \}\end{aligned}$$

where  $\Re\{\cdot\}$  denotes the real part of the argument.

Introducing all these hypotheses in the Maxwell equations, after some simple algebra, we get:

$$\nabla^2 \bar{E}(x, y, z) + k_0^2 n^2(x, y, z) \bar{E}(x, y, z) = \nabla (\nabla \cdot \bar{E}(x, y, z)) \quad (2.8)$$

where  $k_0 = 2\pi/\lambda_0$  is the wavenumber in vacuum and  $n(x, y, z) = \sqrt{\frac{\epsilon(x, y, z)}{\epsilon_0}}$  is the local refractive index.

Being  $\rho = 0$ , equation 2.3 reduces to  $\nabla \cdot \bar{D}(x, y, z, t) = 0$  and we can write:

$$\begin{aligned}\nabla \cdot \bar{D}(x, y, z) &= \nabla \cdot \epsilon(x, y, z) \bar{E}(x, y, z) = \\ &= \epsilon(x, y, z) \nabla \cdot \bar{E}(x, y, z) + \nabla \epsilon(x, y, z) \cdot \bar{E}(x, y, z) = \\ &= 0.\end{aligned} \quad (2.9)$$

From this, it follows immediately that  $\nabla \cdot \bar{E}(x, y, z)$  can be expressed as:

$$\begin{aligned}\nabla \cdot \bar{E}(x, y, z) &= -\frac{\nabla \epsilon(x, y, z)}{\epsilon(x, y, z)} \cdot \bar{E}(x, y, z) = \\ &= -\frac{\nabla n^2(x, y, z)}{n^2(x, y, z)} \cdot \bar{E}(x, y, z).\end{aligned} \quad (2.10)$$

Inserting 2.10 in 2.8 we obtain:

$$\nabla^2 \bar{E}(x, y, z) + k_0^2 n^2(x, y, z) \bar{E}(x, y, z) = \nabla (\nabla (\ln n^2(x, y, z)) \cdot \bar{E}(x, y, z)). \quad (2.11)$$

This is the Helmholtz vectorial equation. In the adopted Cartesian reference frame, this equation can be separated in three equations of the type:

$$\begin{aligned}\frac{\partial^2 E_i(x, y, z)}{\partial x^2} + \frac{\partial^2 E_i(x, y, z)}{\partial y^2} + \frac{\partial^2 E_i(x, y, z)}{\partial z^2} + \\ + k_0^2 n^2(x, y, z) E_i(x, y, z) = -\frac{\partial}{\partial i} \left[ E_x(x, y, z) \frac{\partial \ln n^2(x, y, z)}{\partial x} + \right. \\ \left. E_y(x, y, z) \frac{\partial \ln n^2(x, y, z)}{\partial y} + E_z(x, y, z) \frac{\partial \ln n^2(x, y, z)}{\partial z} \right]\end{aligned} \quad (2.12)$$

where  $i$  can be  $x, y$  or  $z$  and  $E_x(x, y, z)$ ,  $E_y(x, y, z)$ ,  $E_z(x, y, z)$  are the cartesian components of the electric field:

$$\bar{E}(x, y, z) = E_x(x, y, z)\hat{x} + E_y(x, y, z)\hat{y} + E_z(x, y, z)\hat{z}. \quad (2.13)$$

If  $z$  is associated to the propagation direction, one can write any component as the product of a rapidly varying propagation term ( $e^{-jk_0n_0z}$ ) and a slowly varying one  $F_i(x, y, z)$ , the so called *pulse envelope*:

$$E_i(x, y, z) = F_i(x, y, z) e^{-jk_0n_0z} \quad (2.14)$$

where  $n_0$  is a properly chosen reference refractive index.

Replacing 2.14 in 2.12 for  $i = x$  we obtain:

$$\begin{aligned} & \frac{\partial^2 F_x(x, y, z)e^{-j\beta z}}{\partial x^2} + \frac{\partial^2 F_x(x, y, z)e^{-j\beta z}}{\partial y^2} + \frac{\partial^2 F_x(x, y, z)e^{-j\beta z}}{\partial z^2} + \\ & + k_0^2 n^2(x, y, z) F_x(x, y, z) e^{-j\beta z} = -\frac{\partial}{\partial x} \left[ F_x(x, y, z) e^{-j\beta z} \frac{\partial \ln n^2(x, y, z)}{\partial x} + \right. \\ & \left. F_y(x, y, z) e^{-j\beta z} \frac{\partial \ln n^2(x, y, z)}{\partial y} + F_z(x, y, z) e^{-j\beta z} \frac{\partial \ln n^2(x, y, z)}{\partial z} \right] \end{aligned}$$

where  $\beta = k_0 n_0$  is the reference propagation constant. Developing separately the three derivatives:

$$\begin{aligned} \frac{\partial^2 F_x(x, y, z)e^{-j\beta z}}{\partial x^2} &= e^{-j\beta z} \frac{\partial^2 F_x(x, y, z)}{\partial x^2} \\ \frac{\partial^2 F_x(x, y, z)e^{-j\beta z}}{\partial y^2} &= e^{-j\beta z} \frac{\partial^2 F_x(x, y, z)}{\partial y^2} \\ \frac{\partial^2 F_x(x, y, z)e^{-j\beta z}}{\partial z^2} &= \frac{\partial}{\partial z} \left( e^{-j\beta z} \frac{\partial F_x(x, y, z)}{\partial z} - j\beta F_x(x, y, z) e^{-j\beta z} \right) \end{aligned}$$

we obtain:

$$\begin{aligned} & e^{-j\beta z} \frac{\partial^2 F_x(x, y, z)}{\partial x^2} + e^{-j\beta z} \frac{\partial^2 F_x(x, y, z)}{\partial y^2} - j\beta e^{-j\beta z} \frac{\partial F_x(x, y, z)}{\partial z} + \\ & + e^{-j\beta z} \frac{\partial^2 F_x(x, y, z)}{\partial z^2} - j\beta e^{-j\beta z} \frac{\partial F_x(x, y, z)}{\partial z} + (-j\beta)(-j\beta) e^{-j\beta z} F_x(x, y, z) + \\ & + k_0^2 n^2(x, y, z) F_x(x, y, z) e^{-j\beta z} = -\frac{\partial}{\partial x} \left[ F_x(x, y, z) e^{-j\beta z} \frac{\partial \ln n^2(x, y, z)}{\partial x} + \right. \\ & \left. + F_y(x, y, z) e^{-j\beta z} \frac{\partial \ln n^2(x, y, z)}{\partial y} + F_z(x, y, z) e^{-j\beta z} \frac{\partial \ln n^2(x, y, z)}{\partial z} \right]. \end{aligned}$$

This equation can be rearranged as:

$$-\frac{\partial^2 F_x(x, y, z)}{\partial z^2} + j2\beta \frac{\partial F_x(x, y, z)}{\partial z} = \frac{\partial^2 F_x(x, y, z)}{\partial x^2} + \frac{\partial^2 F_x(x, y, z)}{\partial y^2} +$$

$$\begin{aligned}
& + (k_0^2 n^2 - \beta^2) F_x(x, y, z) + \frac{\partial}{\partial x} \left[ F_x(x, y, z) \frac{\partial \ln n^2(x, y, z)}{\partial x} + \right. \\
& \left. + F_y(x, y, z) \frac{\partial \ln n^2(x, y, z)}{\partial y} + F_z(x, y, z) \frac{\partial \ln n^2(x, y, z)}{\partial z} \right]. \quad (2.15)
\end{aligned}$$

If one can assume that the so called Slowly Varying Envelope Approximation (SVEA)

$$\left| \frac{\partial^2 F_x(x, y, z)}{\partial z^2} \right| \ll 2k_0 n_0 \left| \frac{\partial F_x(x, y, z)}{\partial z} \right| \quad (2.16)$$

holds, the contribution of  $\frac{\partial^2 F_x(x, y, z)}{\partial z^2}$  is negligible in 2.15. This approximation, also known as paraxial approximation [38], fixes a limit on the variation of field envelope during the propagation. If SVEA is a too much restrictive condition, it is possible to introduce the Padé approximate operators. They allow to better describe wide angle propagation [39, 40, 41]. The code previously developed was then extended to include the Padé operators. To do so, we first move all the derivatives of  $F_x(x, y, z)$  to the left side of 2.15 in order to leave on the right side only terms which depend on  $F_y$  and  $F_z$ :

$$\begin{aligned}
& \frac{\partial^2 F_x(x, y, z)}{\partial z^2} - 2j\beta \frac{\partial F_x(x, y, z)}{\partial z} + \\
& + \frac{\partial^2 F_x(x, y, z)}{\partial x^2} + \frac{\partial^2 F_x(x, y, z)}{\partial y^2} + \frac{\partial}{\partial x} \left( F_x(x, y, z) \frac{\partial \ln n(x, y, z)^2}{\partial x} \right) + \\
& + (k_0^2 n^2(x, y, z) - \beta^2) F_x(x, y, z) = \\
& = - \underbrace{\frac{\partial}{\partial x} \left[ F_y(x, y, z) \frac{\partial \ln n^2(x, y, z)}{\partial y} + F_z(x, y, z) \frac{\partial \ln n^2(x, y, z)}{\partial z} \right]}_Q.
\end{aligned}$$

We can then write:

$$\begin{aligned}
-\frac{\partial}{\partial z} \left( \frac{\partial}{\partial z} - 2j\beta \right) F_x(x, y, z) & = P F_x(x, y, z) + Q \\
& = P \left( 1 + \frac{Q}{P F_x(x, y, z)} \right) F_x(x, y, z)
\end{aligned}$$

which allows to obtain the  $z$ -derivative of  $F_x(x, y, z)$ :

$$\begin{aligned}
\frac{\partial F_x(x, y, z)}{\partial z} & = - \frac{P \left( 1 + \frac{Q}{P F_x(x, y, z)} \right)}{\frac{\partial}{\partial z} - 2j\beta} F_x(x, y, z) = - \frac{[P(1 + \frac{Q}{P F_x(x, y, z)})]}{2j\beta} F_x(x, y, z) \\
& = \frac{-j[P(1 + \frac{Q}{P F_x(x, y, z)})]}{2\beta} F_x(x, y, z) \\
& = \frac{j}{1 + \frac{j}{2\beta} \frac{\partial}{\partial z}} F_x(x, y, z). \quad (2.17)
\end{aligned}$$

From 2.17 we can find the iterative expression of  $\frac{\partial}{\partial z}$  by using the Padé approximants:

$$\left. \frac{\partial}{\partial z} \right|_p = \frac{-j \left[ P \left( 1 + \frac{Q}{PF_x(x,y,z)} \right) \right]}{1 + \frac{j}{2\beta} \left. \frac{\partial}{\partial z} \right|_{p-1}}. \quad (2.18)$$

We have obtained a recursive relation for the operator  $\frac{\partial}{\partial z}$  whose precision depends on the value of  $p$ . Increasing  $p$  we obtain a better approximation. For example, if  $p = 1$  we can write:

$$\left. \frac{\partial}{\partial z} \right|_1 = \frac{-jP \left( 1 + \frac{Q}{PF_x(x,y,z)} \right)}{2\beta} \quad (2.19)$$

while for  $p = 2$  we find:

$$\begin{aligned} \left. \frac{\partial}{\partial z} \right|_2 &= \frac{\frac{-j \left[ P \left( 1 + \frac{Q}{PF_x(x,y,z)} \right) \right]}{2\beta}}{1 + \frac{j}{2\beta} \left. \frac{\partial}{\partial z} \right|_1} = \frac{\frac{-j \left[ P \left( 1 + \frac{Q}{PF_x(x,y,z)} \right) \right]}{2\beta}}{1 + \frac{j}{2\beta} \frac{-jP \left( 1 + \frac{Q}{PF_x(x,y,z)} \right)}{2\beta}} \\ &= \frac{\frac{-j \left[ P \left( 1 + \frac{Q}{PF_x(x,y,z)} \right) \right]}{2\beta}}{1 + \frac{P \left( 1 + \frac{Q}{PF_x(x,y,z)} \right)}{4\beta^2}}. \end{aligned} \quad (2.20)$$

Usually, we refer to these two examples as Padé approximants of order (1,0) and (1,1) respectively. The first number is the degree of the numerator polynomial, while the second one is the degree of the denominator polynomial. Note that for the approximant (1,0) we obtain the paraxial approximation obtained eliminating the second order derivative term of the field in the propagation direction. We can finally write equation 2.17 using Padé approximant (1,1):

$$\frac{\partial F_x(x,y,z)}{\partial z} = \frac{-j \frac{P \left( 1 + \frac{Q}{PF_x(x,y,z)} \right)}{2\beta}}{1 + \frac{j}{2\beta} \frac{-jP \left( 1 + \frac{Q}{PF_x(x,y,z)} \right)}{2\beta}} = -j \frac{N}{D} F_x(x,y,z) \quad (2.21)$$

where  $N$  and  $D$  are respectively:

$$\begin{aligned} N &= \frac{P \left( 1 + \frac{Q}{PF_x(x,y,z)} \right)}{2\beta} \\ D &= 1 + \frac{P \left( 1 + \frac{Q}{PF_x(x,y,z)} \right)}{4\beta^2}. \end{aligned}$$

From 2.21 one then gets:

$$D \frac{\partial F_x(x,y,z)}{\partial z} = -j N F_x(x,y,z).$$

Repeating the same procedure for  $F_y$  and  $F_z$  and separating the contribution of the different terms, it is possible to rewrite the vectorial equations in the following compact formulation:

$$\begin{aligned} -\frac{\partial F_x(x, y, z)}{\partial z} &= G_{xx}F_x(x, y, z) + G_{xy}F_y(x, y, z) + G_{xz}F_z(x, y, z) \\ -\frac{\partial F_y(x, y, z)}{\partial z} &= G_{yx}F_x(x, y, z) + G_{yy}F_y(x, y, z) + G_{yz}F_z(x, y, z) \\ -\frac{\partial F_z(x, y, z)}{\partial z} &= G_{zx}F_x(x, y, z) + G_{zy}F_y(x, y, z) + G_{zz}F_z(x, y, z) \end{aligned} \quad (2.22)$$

From this system of equations it is quite easy to understand how to move from a vectorial to a scalar formulation of the BPM. First of all, just one equation is needed and then all the coupling terms must vanish. In many case a scalar formulation can be used to find preliminary results in structures where the polarization state is preserved during the propagation. The main advantage is the reduced memory and time consuming with respect to a full vectorial formulation.

### 2.2.1 Finite difference schematization

To solve numerically these equations, a finite difference approach has been adopted: the continuous space is sampled on a lattice structure defined in the computational region using a  $\Delta x$ ,  $\Delta y$ ,  $\Delta z$  mesh and all the differential operators are replaced by their corresponding finite-difference ones. This can be done observing that a complex function  $f(x)$  of a real variable  $x$ , which can be derived at  $x = a$ , has derivatives in this point equal to:

$$f'(a) = \lim_{h \rightarrow 0} \frac{f(a+h) - f(a)}{h}. \quad (2.23)$$

This derivative can be approximated by a central difference scheme as:

$$f'(a) \cong \frac{f(a+h) - f(a-h)}{2h}. \quad (2.24)$$

The same procedure can be applied to the second order derivative:

$$f''(a) \cong \frac{f(a+h) - 2f(a) + f(a-h)}{h^2} = \frac{f'(a+h) - f'(a-h)}{2h}. \quad (2.25)$$

Applying this rules to equations 2.22 the differential problem becomes the following algebraic one:

$$[A] \cdot \bar{x} = \bar{b} \quad (2.26)$$

where  $[A]$  is the coefficient matrix,  $\bar{b}$  is the known terms vector and  $\bar{x}$  is the unknown vector.

## 2.2.2 Crank-Nicholson method

As said before, BPM is an initial value problem. Once the initial conditions are set, the evolution of the propagating field can be calculated. In particular, from the knowledge of the field envelope  $F_i$  in a section  $l$  (in the following  $F_i^l$ ) the algorithm calculates  $F_i$  in the following section  $l + 1$  (in the following  $F_i^{l+1}$ ). The choice of the differential scheme is important because it affects both the stability and the performance of the algorithm. Considering, for example, the equation at the partial derivatives:

$$\frac{\partial f(x, y, z)}{\partial z} = a_1 \frac{\partial g(x, y, z)}{\partial x} + a_2 \frac{\partial g(x, y, z)}{\partial y} \quad (2.27)$$

we can adopt two different methodologies to obtain a numerical solution:

- *explicit scheme*: the solution is obtained approximating 2.27 with:

$$\frac{f_{(x,y,z)}^{l+1} - f_{(x,y,z)}^l}{\Delta z} = a_1 \frac{g_{(x+\Delta x,y,z)}^l - g_{(x,y,z)}^l}{\Delta x} + a_2 \frac{g_{(x,y+\Delta y,z)}^l - g_{(x,y,z)}^l}{\Delta y}. \quad (2.28)$$

In this case  $f_{(x,y,z)}^{l+1}$  can be directly calculated knowing the complete distribution of the two functions  $f(x, y, z)$  and  $g(x, y, z)$  at the previous step  $l$ . The approach is very simple to implement, but there are some constraint which must be satisfied to guarantee that the algorithm is stable [42].

- *implicit scheme*:

$$\begin{aligned} \frac{f_{(x,y,z)}^{l+1} - f_{(x,y,z)}^l}{\Delta z} = \frac{1}{2} \left\{ a_1 \frac{g_{(x+\Delta x,y,z)}^{l+1} - g_{(x,y,z)}^{l+1}}{\Delta x} + a_2 \frac{g_{(x,y+\Delta y,z)}^{l+1} - g_{(x,y,z)}^{l+1}}{\Delta y} + \right. \\ \left. + a_3 \frac{g_{(x+\Delta x,y,z)}^l - g_{(x,y,z)}^l}{\Delta x} + a_4 \frac{g_{(x,y+\Delta y,z)}^l - g_{(x,y,z)}^l}{\Delta y} \right\}. \end{aligned} \quad (2.29)$$

In this case, the solution is more complicated because there are more unknowns at the  $l + 1$  step which are related each other. The advantage of this approach is that this solution is always stable for all the values of  $\Delta z$  [43, 44, 42].

Our BPM solves the equivalent problem 2.27 modifying the *Crank-Nicholson* method [45], which is one of the most popular implicit finite difference numerical schemes. This method allows to write equation 2.29 in this way:

$$\begin{aligned} \frac{f_{(x,y,z)}^{l+1} - f_{(x,y,z)}^l}{\Delta z} = \alpha \left\{ a_1 \frac{g_{(x+\Delta x,y,z)}^{l+1} - g_{(x,y,z)}^{l+1}}{\Delta x} + a_2 \frac{g_{(x,y+\Delta y,z)}^{l+1} - g_{(x,y,z)}^{l+1}}{\Delta y} + \right\}^{l+1} \\ + (1 - \alpha) \left\{ a_3 \frac{g_{(x+\Delta x,y,z)}^l - g_{(x,y,z)}^l}{\Delta x} + a_4 \frac{g_{(x,y+\Delta y,z)}^l - g_{(x,y,z)}^l}{\Delta y} \right\}^l \end{aligned}$$

where  $\alpha$  is a weighting factor necessary to stabilize the whole system. From the numerical point of view, the possible values of  $\alpha$  can change from 0.5, which allows very precise solution but causes instability in some cases, to 1 where a numerical attenuation is introduced perturbing the result but assuring algorithm stability [46].

We followed a mixed approach, in which the explicit scheme was used to evaluate the coupling terms of 2.22 and the implicit scheme was used for the other terms. At the point  $x = h$ ,  $y = p$  one can then write:

$$\left( -\frac{\partial F_x(x, y, z)}{\partial z} \right)_{h,p} \cong \frac{F_x^{l+1}(h, p) - F_x^l(h, p)}{\Delta z}. \quad (2.30)$$

The coupling terms  $G_{xy}F_y$  and  $G_{xz}F_z$  are developed at  $l$  step with the explicit scheme while the term  $G_{xx}F_x$  is written using the implicit one. The stability is provided by the  $\alpha$  parameter. After some algebra, the final system turns out to be:

$$\begin{aligned} A_1(h, p)F_x^{l+1}(h+1, p) + A_2(h, p)F_x^{l+1}(h-1, p) + \\ A_3(h, p)F_x^{l+1}(h, p+1) + A_4(h, p)F_x^{l+1}(h, p-1) + \\ A_5(h, p)F_x^{l+1}(h, p) = N_x(h, p) \end{aligned} \quad (2.31)$$

$$\begin{aligned} C_1(h, p)F_y^{l+1}(h+1, p) + C_2(h, p)F_y^{l+1}(h-1, p) + \\ C_3(h, p)F_y^{l+1}(h, p+1) + C_4(h, p)F_y^{l+1}(h, p-1) + \\ C_5(h, p)F_y^{l+1}(h, p) = N_y(h, p) \end{aligned} \quad (2.32)$$

$$\begin{aligned} G_1(h, p)F_z^{l+1}(h+1, p) + G_2(h, p)F_z^{l+1}(h-1, p) + \\ G_3(h, p)F_z^{l+1}(h, p+1) + G_4(h, p)F_z^{l+1}(h, p-1) + \\ G_5(h, p)F_z^{l+1}(h, p) = N_z(h, p) \end{aligned} \quad (2.33)$$

The solution of this system can be obtained using iterative methods [47], in particular for our BPM we have adopted a GMRES solver.

### 2.2.3 Perfect Matched Layer

The equations described so far hold in an infinite domain, corresponding to the transversal section. Their numerical implementation requires that they are limited to the finite computational domain. Proper boundary conditions must then be set in order to simulate in the mathematical model the infinite physical domain. Different approaches have been proposed so far. Absorbing Boundary Conditions (ABC) [46], which use an artificial layer on the boundary to absorb the incident field, and Transparent Boundary Conditions (TBC) [48], which simulate the infinite domain making some assumption on the characteristics of the incident field, have been used

to reduce field reflections but with non satisfactory results. The introduction of anisotropic absorbing layers called Perfectly Matched Layers (PML) [49, 36] has efficiently eliminated the field reflection at computational windows. The idea of Berenger, who first proposed the PML to absorb outgoing radiation [49], was to divide the magnetic field component  $H_z$  into two subcomponents  $H_{zx}$  and  $H_{zy}$  and to operate on them so that the interface between PML and free space could result reflectionless for all wavelengths, polarizations and incident angles.

Later on, Sacks [50] used the anisotropic material properties  $(\epsilon, \mu, \sigma_E, \sigma_H)$  to describe the absorbing PML layer, where  $\sigma_E$  and  $\sigma_H$  are the electric and magnetic conductivity, respectively. Let us then consider a material with complex diagonal relative permittivity and permeability tensors given by

$$\begin{aligned} \bar{\bar{\epsilon}}_r &= \begin{bmatrix} \epsilon_r^x + \frac{\sigma_E^x}{j\omega} & 0 & 0 \\ 0 & \epsilon_r^y + \frac{\sigma_E^y}{j\omega} & 0 \\ 0 & 0 & \epsilon_r^z + \frac{\sigma_E^z}{j\omega} \end{bmatrix} \\ \bar{\bar{\mu}}_r &= \begin{bmatrix} \mu_r^x + \frac{\sigma_H^x}{j\omega} & 0 & 0 \\ 0 & \mu_r^y + \frac{\sigma_H^y}{j\omega} & 0 \\ 0 & 0 & \mu_r^z + \frac{\sigma_H^z}{j\omega} \end{bmatrix}. \end{aligned} \quad (2.34)$$

In order to match the intrinsic impedance of the free space, the condition

$$\frac{\epsilon_0 \bar{\bar{\epsilon}}_r}{\epsilon_0} = \frac{\mu_0 \bar{\bar{\mu}}_r}{\mu_0} \quad (2.35)$$

must be satisfied. Therefore it must be:

$$\bar{\bar{\epsilon}}_r = \bar{\bar{\mu}}_r = \begin{bmatrix} a & 0 & 0 \\ 0 & b & 0 \\ 0 & 0 & c \end{bmatrix} = \bar{\bar{\Lambda}} \quad (2.36)$$

where

$$\begin{aligned} a &= \epsilon_r^x + \frac{\sigma_E^x}{j\omega} = \mu_r^x + \frac{\sigma_H^x}{j\omega} \\ b &= \epsilon_r^y + \frac{\sigma_E^y}{j\omega} = \mu_r^y + \frac{\sigma_H^y}{j\omega} \\ c &= \epsilon_r^z + \frac{\sigma_E^z}{j\omega} = \mu_r^z + \frac{\sigma_H^z}{j\omega}. \end{aligned}$$

By studying the reflection coefficients at the interfaces between the PML region and free space, we find that in certain circumstances reflection can be zero. For the PML region with an interface where  $x = \text{const}$  and  $y = \text{const}$ ,  $\bar{\bar{\Lambda}}$  is required to be [51]:

$$\bar{\bar{\Lambda}}_x = \begin{bmatrix} a & 0 & 0 \\ 0 & \frac{1}{a} & 0 \\ 0 & 0 & \frac{1}{a} \end{bmatrix} \quad (2.37)$$

for  $x = \text{const}$ , and

$$\overline{\overline{\Lambda}}_y = \begin{bmatrix} \frac{1}{b} & 0 & 0 \\ 0 & b & 0 \\ 0 & 0 & \frac{1}{b} \end{bmatrix} \quad (2.38)$$

for  $y = \text{const}$ . The PML tensor is obtained multiplying the previous two tensors for the PML regions at the four corners of the computational window:

$$\overline{\overline{\Lambda}}_{xy} = \overline{\overline{\Lambda}}_x \cdot \overline{\overline{\Lambda}}_y = \begin{bmatrix} \frac{a}{b} & 0 & 0 \\ 0 & \frac{b}{a} & 0 \\ 0 & 0 & \frac{1}{ab} \end{bmatrix}. \quad (2.39)$$

For the full-vectorial formulation we then modify the permittivity and permeability tensors  $\overline{\overline{\epsilon}}$  and  $\overline{\overline{\mu}}$  to

$$\begin{aligned} \overline{\overline{\epsilon}} &= \overline{\overline{\epsilon}} \cdot \overline{\overline{S}}^{-1} \\ \overline{\overline{\mu}} &= \overline{\overline{\mu}} \cdot \overline{\overline{S}} \end{aligned} \quad (2.40)$$

where

$$\overline{\overline{S}} = \begin{bmatrix} \frac{S_y S_z}{S_x} & 0 & 0 \\ 0 & \frac{S_z S_x}{S_y} & 0 \\ 0 & 0 & \frac{S_x S_y}{S_z} \end{bmatrix}. \quad (2.41)$$

The PML parameters ( $S_x, S_y, S_z$ ) are assigned to each PML region as shown in figure 2.1: for the non-PML regions, the PML tensor  $\overline{\overline{S}}$  is an identity matrix, while in the PML regions the parameters are given by:

$$S_i = 1 - j \frac{\sigma_E^{MAX}}{\omega \epsilon_0 \epsilon_r^{PML}} \left( \frac{\rho}{d_i} \right)^m, \quad i = 1, 2, 3, 4 \quad (2.42)$$

where  $\rho$  is the distance from the PML boundary,  $d$  is the thickness of the PML layer and  $m$  controls the profile of the conductivity. Generally, linear ( $m = 1$ ), parabolic ( $m = 2$ ) and cubic ( $m = 3$ ) conductivity profiles are assumed. The maximum electric conductivity  $\sigma_E^{MAX}$  and the permittivity of the PML layers are determined from the required reflection coefficient [52] according to [53]:

$$R_i = \exp \left( - \frac{2\sigma_E^{\max} d_i}{3\epsilon_0 c \sqrt{\epsilon_r^{PML}}} \right) \quad (2.43)$$

where  $R_i$  is the reflection coefficient of the  $i^{\text{th}}$  PML region and  $c$  is the light velocity in vacuum. Typically  $R_i$  is chosen to be about  $10e - 4$  [53] and  $\sigma_E^{MAX}$  to be about  $0.01\Omega^{-1}(\mu m)^{-1}$  when the permittivity is chosen as 1. The parameters ( $S_x, S_y, S_z$ ) are still all equal to 1 for non-PML regions and assigned according to figure 2.1 for

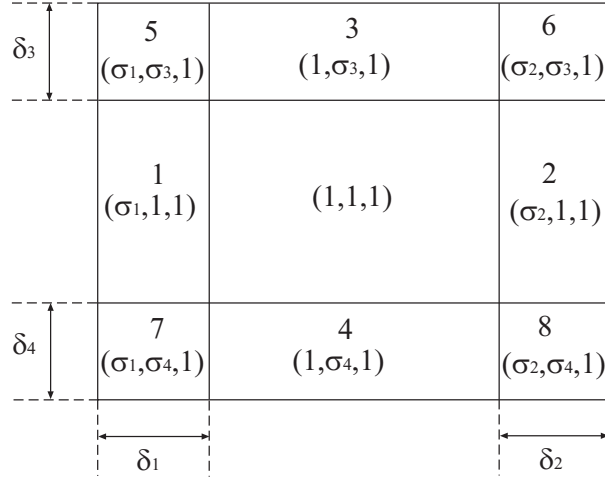


Figure 2.1: Computational domain surrounded by perfectly matched layer (PML).

PML regions. Note that the transformations set by equation 2.40 are intrinsically equivalent to modify the  $\nabla$  operator of 2.11 into

$$\nabla = \hat{x} S_x \frac{\partial}{\partial x} + \hat{y} S_y \frac{\partial}{\partial y} + \hat{z} S_z \frac{\partial}{\partial z}. \quad (2.44)$$

However, this does not introduce extra programming complexity, since all the procedures related to the iterative solver and propagation technique remain unchanged.

## 2.2.4 BPM validation

Two kinds of validation for the 3D BPM algorithm will be discussed: the effect of PML and the effect of Padé approximants.

To test the efficiency of the PML absorber, we calculate first Gaussian beam propagation in the free space with and without absorbing layers. Then we compare these two results with the correct field obtained adopting a larger computational window, chosen to avoid interactions between field and domain boundary. Figure 2.2 shows Gaussian beam propagation in the free-space when boundary condition are absent. The input beam is launched on the  $(x, y)$ -plane. As expected, the beam is reflected when approaching the computational boundary and after some distance the reflection strongly interferes with the original propagating beam. The total power within the computational window is conserved. Errors are large, as it can be observed in the last figure of the sequence.

These results can be compared with those obtained when the free space is surrounded by the anisotropic PML absorber. At the interface between PML and free space, reflection is completely eliminated, as clearly shown in figure 2.3. In this calculation, the transversal mesh size is given by  $\Delta_x = \Delta_y = 0.2 \mu m$ , the propagation

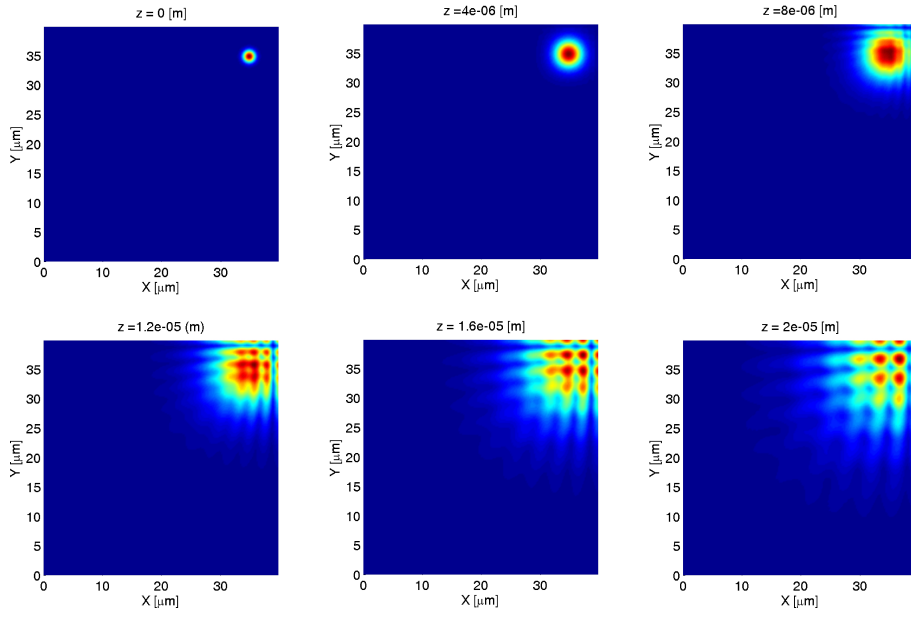


Figure 2.2: From upper left to lower right: gaussian beam intensity at  $z = 0$ ,  $z = 4 \mu m$ ,  $z = 8 \mu m$ ,  $z = 12 \mu m$ ,  $z = 16 \mu m$ ,  $z = 20 \mu m$  (Without PML).

step is  $\Delta_z = 0.1 \mu m$ , and the conductivity distribution inside the PML region has a parabolic profile.

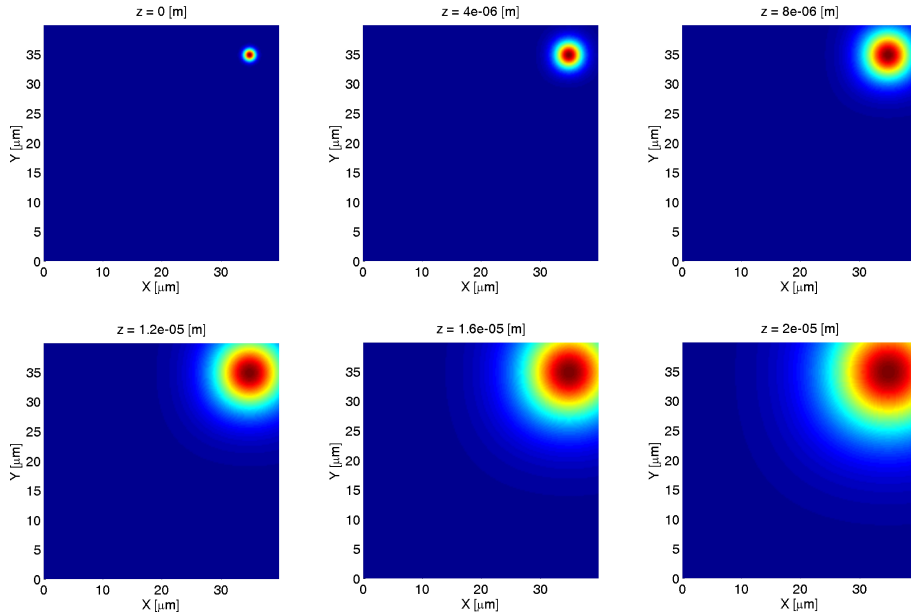


Figure 2.3: From upper left to lower right: gaussian beam intensity at  $z = 0$ ,  $z = 4 \mu m$ ,  $z = 8 \mu m$ ,  $z = 12 \mu m$ ,  $z = 16 \mu m$ ,  $z = 20 \mu m$  (With PML).

Looking at the figures, the field does not seem perturbed by the presence of the PML layers. To check quantitatively this qualitative result, a simulation with a bigger computational windows has been made. In the left part of figure 2.4, a section of the four field profiles ( $y = 35 \mu m$ ) calculated at the same plane of  $z = 20 \mu m$  is plotted. The dashed line refers to the field computed in a  $70 \mu m \times 70 \mu m$  window; the black line refers to the field computed in a  $40 \mu m \times 40 \mu m$  window with 20 PML layers; the red line refers to the field computed in a  $40 \mu m \times 40 \mu m$  window without PML. The oscillations due to reflections when PML are not used appear clearly, while the field distribution obtained using PML practically superimpose to the field computed in the larger domain, thus proving the ability of PML to simulate an infinite computational domain. The right part of figure 2.4 shows differences among the results in terms of relative error between the results obtained in the smaller computational window and those obtained in the larger one. In the PML case the error is of the order of  $10^{-4}$  and in the figure it almost coincides with the x-axis.

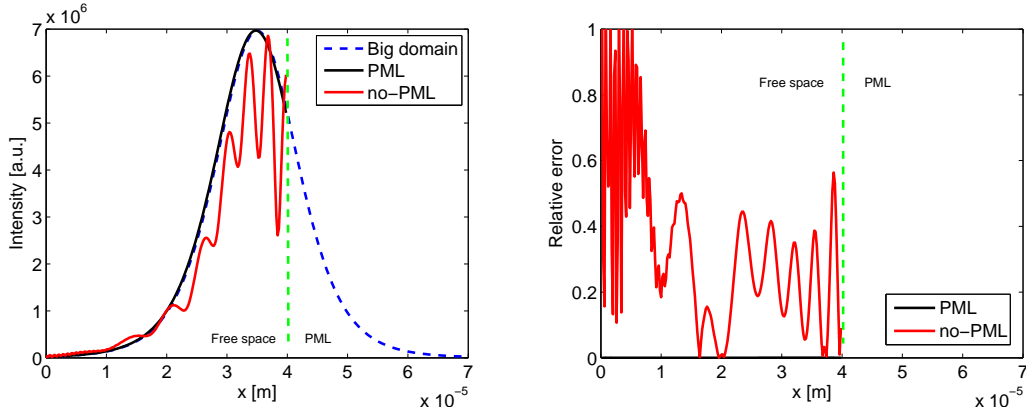


Figure 2.4: In the left part we show the field section at  $z = 20 \mu m$  calculated with PML (black line) and without PML (red line) compared with the numerical result obtained for a large computational window (dashed line). In the right part we show the relative error for the PML and non-PML solution respect the case of big domain.

To confirm absorption in the PML layers, figure 2.5 shows the evolution of the total power in the computational domain during propagation. Power reduction caused during the propagation by the artificial loss of the PML is evident. From the physical point of view this power reduction corresponds to the power radiated outside the computational window.

The second kind of test we have done concern the effect of the Padé approximant introduction. To do that we consider a tilted gaussian beam propagation in free space and we compare the two solutions obtained with the paraxial approximation and with Padé (1,1) with respect to the theoretical field obtained Fourier transforming the initial beam. The calculation domain is the same adopted for the PML validation.

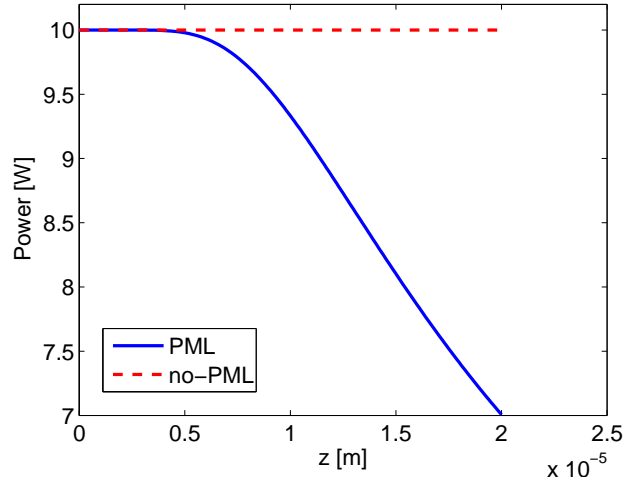


Figure 2.5: Power in the computational window at different propagation steps: constant when PML are not used, decreasing when PML are used.

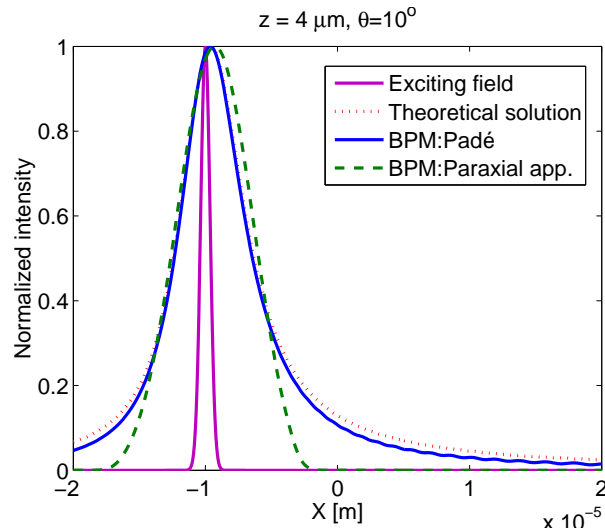


Figure 2.6: Comparison between the solutions obtained with the paraxial approximation and with Padé (1,1) with respect to the theoretical field for a tilted gaussian propagation in free space at  $10^\circ$ .

Figure 2.6 shows the results for a propagation angle of  $10^\circ$ . As one can see only results obtained using the Padé approximants agree quite well with the expected field shape, while this does not happen when the paraxial approximation is used. For larger angles, an higher approximation order with respect to (1,1) is however necessary.

### 2.2.5 Consideration on the non-unitarity of BPM operators

While numerous numerical simulations of optical devices have been performed with explicitly stable one-way scalar finite-difference electrical field propagation methods, electric field polarization evolution in complex waveguiding geometries must be described using the full vectorial finite-element procedures. However, these algorithms intrinsically violate power-conservation [54]. This is due to numerical problems induced in difference calculations by the discontinuities of some of the electric field components at the interfaces between different dielectric materials. To solve this problem we have implemented also a formulation of the fully vectorial BPM with PML and Padé (1,1) based on the vector Helmholtz equations written for the magnetic field instead of the electric field:

$$\nabla^2 \bar{H} + n_0^2 k_0^2 \bar{H} + \frac{1}{n_0^2} \nabla n_0^2 \times (\nabla \times \bar{H}) = 0 \quad (2.45)$$

using the condition:

$$\nabla \cdot \bar{H} = 0. \quad (2.46)$$

The magnetic field distribution does not present any discontinuity at dielectric interfaces. With this approach stable solutions has been obtained even in cases where the E formulation fails. The formal steps necessary to develop the equation to be solved, formally similar to 2.31, 2.32, 2.33, starting from the Helmholtz equation are practically the same used for the E field formulation developed in the last section, and will then not reported, for the sake of brevity.

Figure 2.7 shows the computed fields propagating in a square waveguide ( $n = 1.1$ ) surrounded by air using both the E and H formulation. Note that for the electric field components  $E_x$  and  $E_y$  discontinuities appear at the interfaces between waveguide and air in  $x$  and  $y$  direction, respectively, while the magnetic field is not affected by these discontinuities.

## 2.3 Finite difference mode solver

A further code developed and used during this thesis allows to calculate the modes propagating in a  $z$ -invariant structure. In this case just one section of the structure must be studied, as the *ansatz* of separation of variables can be done and the field propagating along  $z$  is assume to depend on such a coordinate by the translation factor ( $\exp(-j\beta z)$ ).

To implement our mode solver we have adopted the formulation proposed by [55]. The structure is superimposed to a cartesian mesh with not necessarily constant steps. The general case, for an arbitrary point P inside the mesh with neighboring points N,W,S,E is shown in figure 2.8. The used Helmholtz equations follows the  $H$

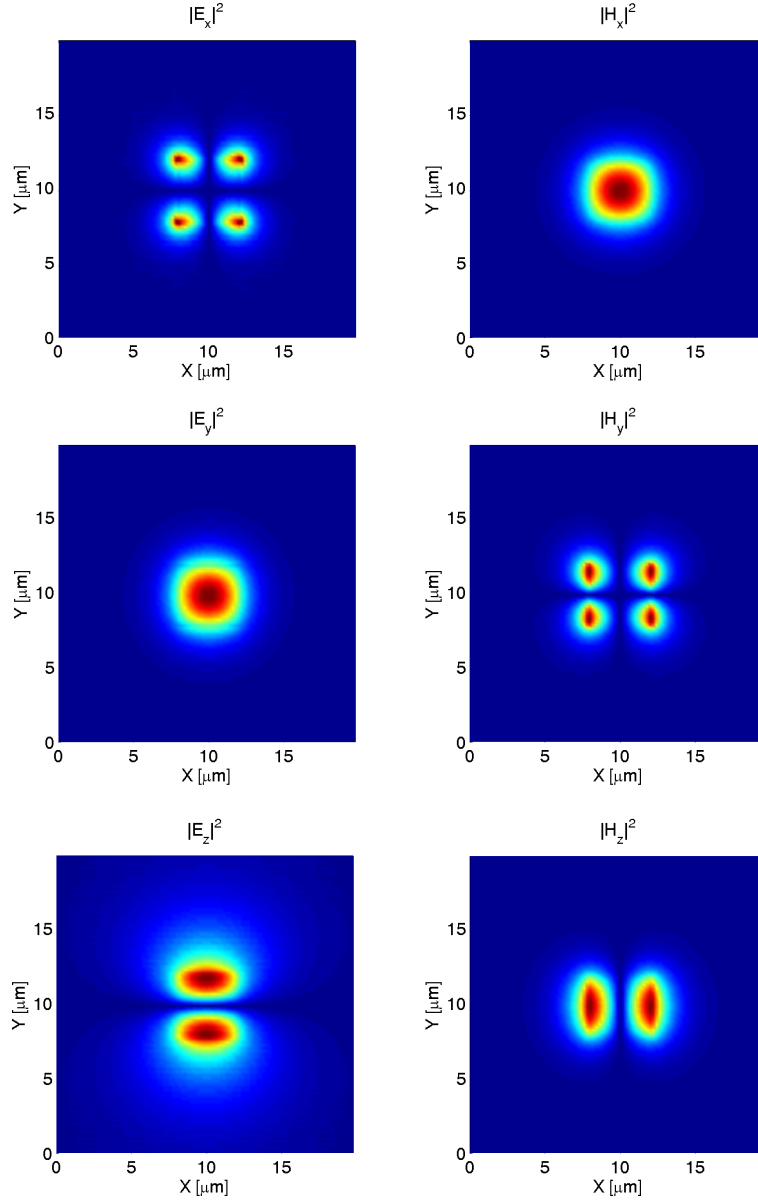


Figure 2.7: Six components of the fundamental mode of a square waveguide with refractive index 1.1 surrounded by air calculated with both the E (left) and H (right) BPM formulations.

scheme for the four subregions ( $\nu = 1, 2, 3, 4$ ):

$$\frac{\partial^2 H_x}{\partial x^2} + \frac{\partial^2 H_x}{\partial y^2} + (\varepsilon_\nu k^2 - \beta^2) H_x = 0 \quad (2.47)$$

$$\frac{\partial^2 H_y}{\partial x^2} + \frac{\partial^2 H_y}{\partial y^2} + (\varepsilon_\nu k^2 - \beta^2) H_y = 0 \quad (2.48)$$

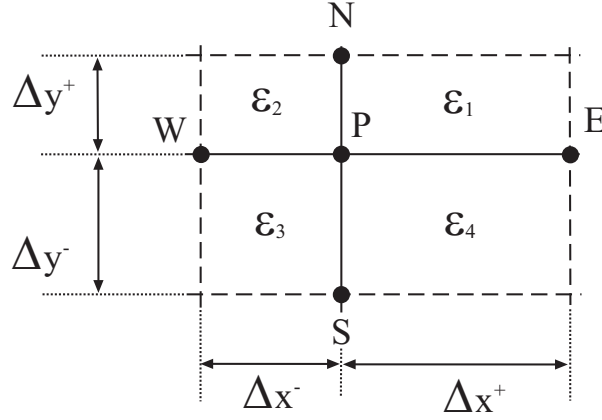


Figure 2.8: Point P and neighboring points in a cartesian mesh with uniform dielectric constant  $\epsilon_1, \epsilon_2, \epsilon_3, \epsilon_4$  of the subregion 1-4.

To obtain the discrete formulation, the differential operators can be developed using a second order Taylor expansion:

$$H_W = H_P - \Delta x^- \frac{\partial H}{\partial x} \Big|_W + \frac{(\Delta x^-)^2}{2} \frac{\partial^2 H}{\partial x^2} \Big|_W + O[(\Delta x^-)^3] \quad (2.49)$$

$$H_E = H_P + \Delta x^+ \frac{\partial H}{\partial x} \Big|_E + \frac{(\Delta x^+)^2}{2} \frac{\partial^2 H}{\partial x^2} \Big|_E + O[(\Delta x^+)^3] \quad (2.50)$$

$$H_S = H_P - \Delta y^- \frac{\partial H}{\partial y} \Big|_S + \frac{(\Delta y^-)^2}{2} \frac{\partial^2 H}{\partial y^2} \Big|_S + O[(\Delta y^-)^3] \quad (2.51)$$

$$H_N = H_P + \Delta y^+ \frac{\partial H}{\partial y} \Big|_N + \frac{(\Delta y^+)^2}{2} \frac{\partial^2 H}{\partial y^2} \Big|_N + O[(\Delta y^+)^3] \quad (2.52)$$

The possibility of choosing different values for  $\Delta x^\pm$  and  $\Delta y^\pm$  allows to reduce the mesh step where the field is expected to concentrate, but should be done with care, as it also influences precision, which decreases for increasing mesh size differences.

The approximated expression for the second order derivative operators can be obtained adding the equation 2.49 to 2.52, 2.49 to 2.51, 2.50 to 2.51 and 2.50 to 2.52 respectively. Replacing the operators in the Helmholtz equations we obtain:

$$\begin{aligned} & \frac{2H_W}{(\Delta x^-)^2} - \frac{2H_P}{(\Delta x^-)^2} + \frac{2}{\Delta x^-} \frac{\partial H}{\partial x} \Big|_W + \\ & + \frac{2H_N}{(\Delta y^+)^2} - \frac{2H_P}{(\Delta y^+)^2} - \frac{2}{\Delta y^+} \frac{\partial H}{\partial y} \Big|_N + \\ & + (\epsilon_2 k^2 - \beta^2) H_P = 0 \end{aligned} \quad (2.53)$$

$$\frac{2H_W}{(\Delta x^-)^2} - \frac{2H_P}{(\Delta x^-)^2} + \frac{2}{\Delta x^-} \frac{\partial H}{\partial x} \Big|_W +$$

$$\begin{aligned}
& + \frac{2H_S}{(\Delta y^-)^2} - \frac{2H_P}{(\Delta y^-)^2} + \frac{2}{\Delta y^-} \left. \frac{\partial H}{\partial y} \right|_S + \\
& \quad + (\varepsilon_3 k^2 - \beta^2) H_P = 0
\end{aligned} \tag{2.54}$$

$$\begin{aligned}
& \frac{2H_E}{(\Delta x^+)^2} - \frac{2H_P}{(\Delta x^+)^2} - \frac{2}{\Delta x^+} \left. \frac{\partial H}{\partial x} \right|_E + \\
& + \frac{2H_S}{(\Delta y^-)^2} - \frac{2H_P}{(\Delta y^-)^2} + \frac{2}{\Delta y^-} \left. \frac{\partial H}{\partial y} \right|_S + \\
& \quad + (\varepsilon_4 k^2 - \beta^2) H_P = 0
\end{aligned} \tag{2.55}$$

$$\begin{aligned}
& \frac{2H_E}{(\Delta x^+)^2} - \frac{2H_P}{(\Delta x^+)^2} - \frac{2}{\Delta x^+} \left. \frac{\partial H}{\partial x} \right|_E + \\
& + \frac{2H_N}{(\Delta y^+)^2} - \frac{2H_P}{(\Delta y^+)^2} - \frac{2}{\Delta y^+} \left. \frac{\partial H}{\partial y} \right|_N + \\
& \quad + (\varepsilon_1 k^2 - \beta^2) H_P = 0
\end{aligned} \tag{2.56}$$

where  $H$  stands for  $H^x$  or  $H^y$ . Applying continuity condition at the boundaries of neighboring cells we can eliminate the first order derivative component of  $H$ . This can be done with the relation  $\nabla \cdot H = 0$  obtaining:

$$H_z = \frac{1}{j\beta} \left( \frac{\partial H_x}{\partial x} + \frac{\partial H_y}{\partial y} \right) \tag{2.57}$$

$$E_z = \frac{1}{j\varepsilon k \sqrt{\mu_0 \varepsilon_0}} \left( \frac{\partial H_y}{\partial x} + \frac{\partial H_x}{\partial y} \right). \tag{2.58}$$

For an horizontal discontinuity we can write (see figure 2.9):

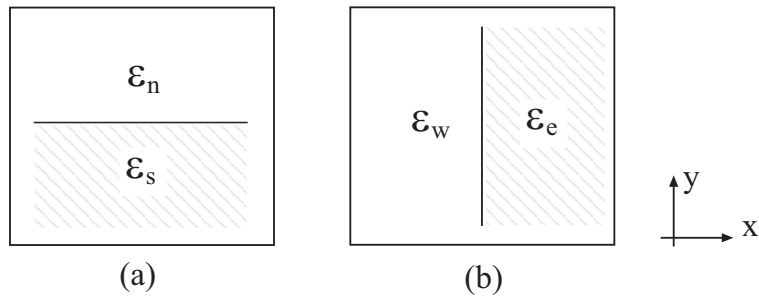


Figure 2.9: Horizontal (a) and vertical (b) discontinuity between neighboring cells.

$$\left. \frac{\partial H_y}{\partial y} \right|_N = \left. \frac{\partial H_y}{\partial y} \right|_S \tag{2.59}$$

$$\varepsilon_n \left. \frac{\partial H_x}{\partial y} \right|_S - \varepsilon_s \left. \frac{\partial H_x}{\partial y} \right|_N = (\varepsilon_n - \varepsilon_s) \left. \frac{\partial H_x}{\partial y} \right| \tag{2.60}$$

while for a vertical one:

$$\left. \frac{\partial H_x}{\partial x} \right|_W = \left. \frac{\partial H_x}{\partial x} \right|_E \quad (2.61)$$

$$\varepsilon_n \left. \frac{\partial H_y}{\partial x} \right|_W - \varepsilon_s \left. \frac{\partial H_y}{\partial x} \right|_E = (\varepsilon_e - \varepsilon_w) \left. \frac{\partial H_x}{\partial y} \right|_E \quad (2.62)$$

These conditions allow to eliminate spurious results which do not correspond to physical solutions. After some simple algebra, it is possible to obtain a linear eigenvalue problem described by the following matrix formulation:

$$\overline{\overline{A}} \cdot \overline{H} \equiv \begin{bmatrix} A_{xx} & A_{xy} \\ A_{yx} & A_{yy} \end{bmatrix} \cdot \begin{bmatrix} H_x \\ H_y \end{bmatrix} = \beta^2 \begin{bmatrix} H_x \\ H_y \end{bmatrix} \equiv \beta^2 \overline{H} \quad (2.63)$$

where  $\overline{\overline{A}}$  is a matrix of elements which depend on the dielectric constant of the structure,  $H_x$  and  $H_y$  are the eigenvector and  $\beta^2$  is the eigenvalue.

This problem is solved by an iterative algorithm [47]. After computing the transverse components  $H_x$  and  $H_y$  the longitudinal components  $H_z$  and  $E_z$  can be computed by 2.57 and 2.58, respectively. The transverse electric field components  $E_x$  and  $E_y$  can be determined with ( $\nabla \times \overline{H} = j\omega\varepsilon_0\varepsilon\overline{E}$ ):

$$E_x = \frac{\beta}{\varepsilon k} \sqrt{\frac{\mu_0}{\varepsilon_0}} H_y - \frac{1}{\varepsilon k \beta} \sqrt{\frac{\mu_0}{\varepsilon_0}} \left( \frac{\partial^2 H_x}{\partial x \partial y} + \frac{\partial^2 H_y}{\partial y^2} \right) \quad (2.64)$$

$$E_y = -\frac{\beta}{\varepsilon k} \sqrt{\frac{\mu_0}{\varepsilon_0}} H_x + \frac{1}{\varepsilon k \beta} \sqrt{\frac{\mu_0}{\varepsilon_0}} \left( \frac{\partial^2 H_x}{\partial x^2} + \frac{\partial^2 H_y}{\partial x \partial y} \right) \quad (2.65)$$

In conclusion we have obtained the all six components of the electromagnetic field.

### 2.3.1 Mode solver validation

In order to validate the implementation of the mode solver we have calculated the field components and the effective index of the propagating mode of the rib waveguide shown in figure 2.10. The wavelength of the propagating field is  $\lambda = 1.55 \mu m$  and the mesh is constituted by  $160 \times 320$  points. Figure 2.11 shows the calculated transversal field components. The value of the obtained effective index has been compared with those obtained using other techniques and the results are compared in table 2.1 where the mesh size  $\Delta x = \Delta y$  used for the calculations is also specified. Results agree quite well. Slight differences can be explained considering that some approximations have been made. First of all, the differential equations 2.47 and 2.48 are replaced by difference equations, and the mesh size influences the result precision. Then, even iterative techniques used to solve the eigenvalue problem are different and cause additional errors. Note finally also that, in the even more general case of graded index structures or structures with contours not parallel to lines of the grid, to be able to solve the problem with the used rectangular mesh, the index profile have to be approximated by stair cases.

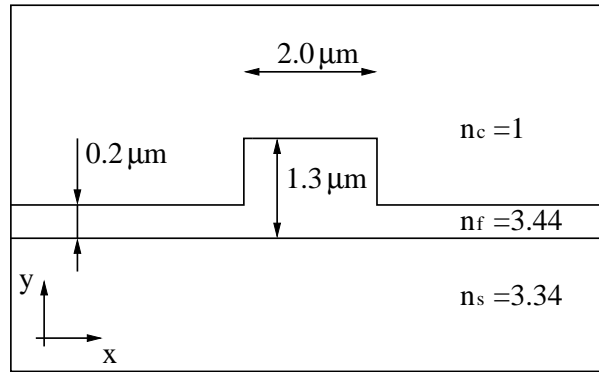


Figure 2.10: Rib waveguide with large refractive index step.

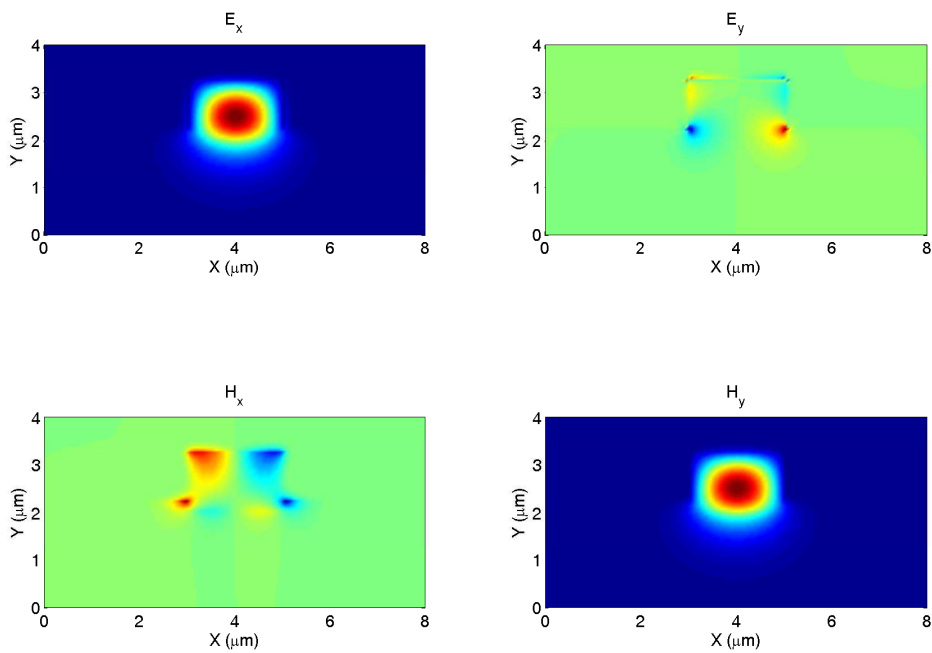


Figure 2.11: Transversal electromagnetic field components of the fundamental mode of the rib waveguide.

Method	$\Delta x = \Delta y$ [ $\mu m$ ]	$n_{eff}$
Robertson [56]	0.033	3.391292
Delage [57]	0.025	3.391320
Vassallo [58]	0.01	3.388669
Stern [59]	0.095	3.386926
This work	0.025	3.384989

Table 2.1: Values of the effective index of the fundamental mode of the test rib waveguide calculated by various numerical approaches.

# 3

## Device fabrication techniques

### 3.1 Introduction

In the two previous chapters we have described the theoretical properties of segmented waveguides and the tools for their numerical modelling. In this chapter, we will describe the techniques used for their fabrication. In particular we will concentrate on device realized in Lithium Niobate, which is one of the most popular materials used for integrated optical waveguides because of its many properties. It exhibits in fact low propagation losses at the telecommunication wavelengths of interest, good non linear properties, which allow efficient frequency conversion operations, and high electro-optical coefficients allowing fabrication of Mach-Zender modulators and other electronically driven optical circuits.

After recalling the main physical features of Lithium Niobate, we will illustrate the various fabrication steps, the photolithography operations and the photomask design of the devices. The samples obtained with this fabrication procedure present good quality shape of the exchanged zone, but require improvements in terms of surface roughness and scattering losses for the segmented waveguides.

### 3.2 Properties of Lithium Niobate

Lithium Niobate, whose chemical formula is  $LiNbO_3$ , is an anisotropic material. This means that its optical characteristics depend on the propagation of the electromagnetic field direction. Anisotropy is one peculiar characteristic of the crystals and it is directly related to the particular atom arrangements.

The Lithium Niobate elementary cell belongs to the hexagonal crystallographic system. We indicate the crystal axes as  $X, Y, Z$ , while  $a, b, c$  are the size of the crystallographic cell and  $\alpha, \beta, \gamma$  are the angles formed between these three axes, as shown in figure 3.1.

From the optical point of view, Lithium Niobate is an uniaxial crystal. This

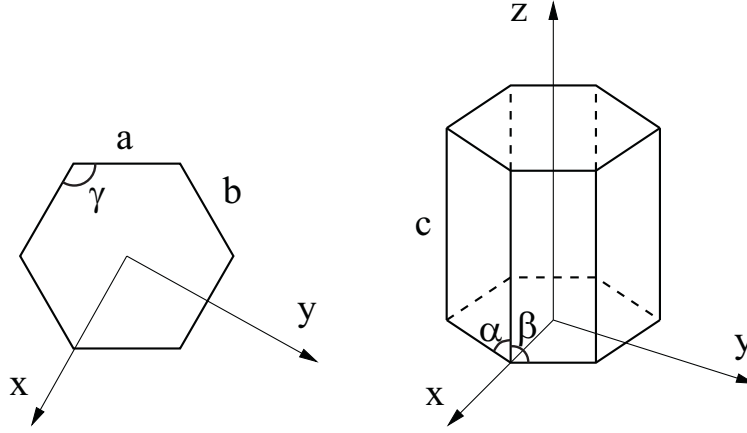


Figure 3.1: Elementary cell of the Lithium Niobate crystal lattice.

means that the permittivity dielectric tensor  $\bar{\bar{\epsilon}}$  written with respect to a Cartesian frame presents non zero terms only on the main diagonal and two of them are equal.

$$\bar{\bar{\epsilon}}_r = \begin{pmatrix} n_1^2(x, y) & 0 & 0 \\ 0 & n_1^2(x, y) & 0 \\ 0 & 0 & n_3^2(x, y) \end{pmatrix}. \quad (3.1)$$

In this way the secular equation, which describes the plane wave propagation in the lattice, becomes [38]:

$$[k^2 - k_o^2 n_1^2] \cdot [k^2 (s_1^2 + s_2^2) n_1^2 + k^2 s_3^2 n_3^2 - k_o^2 n_1^2 n_3^2] = 0 \quad (3.2)$$

where  $k$  is the wavenumber, while  $s_i$  are the cosine directors of the wavevector and  $n_1 = n_2$ ,  $n_3$  are the refractive indices in the  $x$ ,  $z$  directions in the considered reference system. The solution of equation 3.2 can be obtained solving a system in two equations:

$$\begin{cases} k^2 - k_o^2 n_1^2 = 0 \\ \frac{k^2 s_1^2}{n_3^2} + \frac{k^2 s_2^2}{n_3^2} + \frac{k^2 s_3^2}{n_1^2} = 0 \end{cases} \quad (3.3)$$

The first equation does not depend on the considered propagation direction: the corresponding normal surface is then described by a sphere. This means that for any direction, the propagation constant does not change. This kind of wave is commonly named *ordinary*, because everything works like in the isotropic case.

The second equation describes an ellipsoid generated around the rotational  $z$  axis. As a consequence, modifying the propagation direction, the wavenumber  $k$  changes accordingly. This solution is known as the *extraordinary wave*.

The extraordinary and ordinary refractive indices of the Lithium Niobate massive crystals are well approximated, in their wavelength (chromatic dispersion) and

temperature dependencies, by the Sellmeier relations 3.4 [60]:

$$\begin{aligned}
 n_o^2 &= 4.9048 + \frac{0.11775 + 2.2314 \cdot 10^{-8}(T - 24.5)(T + 24.5 + 546)}{\lambda^2 - [0.21802 - 2.9671 \cdot 10^{-8}(T - 24.5)(T + 24.5 + 546)]^2} + \\
 &+ 2.1429 \cdot 10^{-8}(T - 24.5)(T + 24.5 + 546) - 0.027153 \cdot \lambda^2 \\
 n_e^2 &= 4.5820 + \frac{0.09921 + 5.2716 \cdot 10^{-8}(T - 24.5)(T + 24.5 + 546)}{\lambda^2 - [0.21090 - 4.9143 \cdot 10^{-8}(T - 24.5)(T + 24.5 + 546)]^2} + \\
 &+ 2.2971 \cdot 10^{-7}(T - 24.5)(T + 24.5 + 546) - 0.021940 \cdot \lambda^2
 \end{aligned} \tag{3.4}$$

where the wavelength  $\lambda$  is expressed in  $\mu m$  and the temperature  $T$  in  $^{\circ}C$ . In figure 3.2 the extraordinary and ordinary indices are plotted as a function of the wavelength for  $T = 25^{\circ}C$  in the interval of interest. Lithium Niobate is a non centrosymmetric

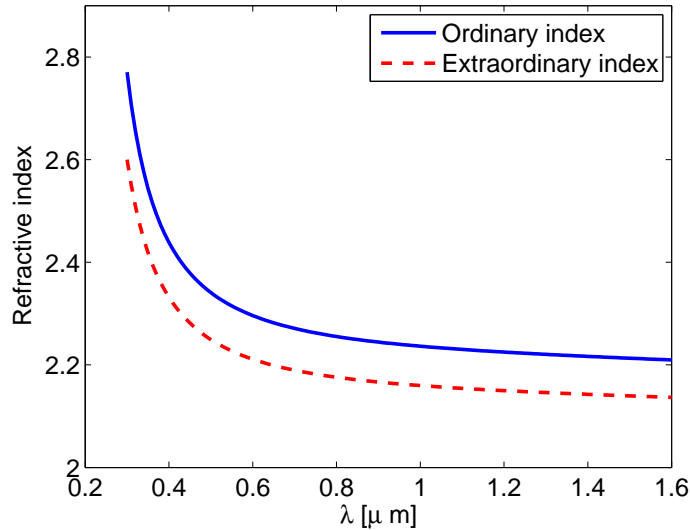


Figure 3.2: Extraordinary and ordinary refractive index of the Lithium Niobate crystal as a function of the wavelength for  $T = 25^{\circ}C$ .

crystal and then can exhibit also second order non linear effects. We will not use this properties and for this reason we refer to specialized books [9] for a complete description of non linearity effects.

### 3.3 Waveguide fabrication

In order to realize optical waveguides in a Lithium Niobate substrate, many techniques have been proposed in the past: out-diffusion [61], titanium indiffusion [62], ion implantation [63], proton exchange [64] and its different implementations (simple Proton Exchange [64], Annealed Proton Exchange, APE [65], Soft Proton

Exchange, SPE [66]). Among the PE techniques, we have chosen the SPE process as it does not perturb the crystalline structure of  $LiNbO_3$  while other ones do [67, 68]. In particular, the ferroelectric domain inversion of Periodically Poled Lithium Niobate (PPLN) devices remains intact after SPE [69].

### 3.3.1 Soft Proton Exchange

The Soft Proton Exchange process (SPE) in Lithium Niobate substrate is an interesting and important technique for the fabrication of integrated optical devices. The most important advantage of this technique is the easier way with which the devices can be realized. The technique is based on the diffusion of hydrogen ions ( $H^+$ ) that penetrate the Lithium Niobate wafer going to tie with oxygen creating a thin layer that represents the transmission channel. At the same time, lithium ions ( $Li^+$ ) escape from the substrate in the opposite direction leaving the space for the hydrogen ions. The diffusion process can be written using the following equation:



where  $x$  represents the normalized proton concentration.

The proton source used with Lithium Niobate is the Benzoic acid ( $C_6H_5COOH$ ) with a fraction of Lithium Benzoate (LB). In order to obtain a waveguide, it is necessary to dispose of a Lithium Niobate substrate cut along one of the three possible plans, we indicate with  $X$ -cut,  $Y$ -cut and  $Z$ -cut (in our case, crystals were  $Z$ -cut  $LiNbO_3$  substrates with diffusion plane orthogonal to the  $Z$  axis). The most important parameters for this process are the percentage of LB in the mixture, the  $T_{spe}$  (time interval in which the substrate remains in contact with the acid) and the temperature at which the process happens. Varying %LB between 0 and 5, the nature of the exchanged layer is strongly modified. It is possible to identify three different regimes, as shown in figure 3.3, corresponding to three different ranges of %LB: Proton Exchange (PE), Multiphase Proton Exchange (MPE) and Soft Proton Exchange (SPE). In the left part of figure 3.3 a low value of %LB is considered ( $0 < \%LB < 1\%$ ): in this regime the index profile is step with maximum value  $\Delta n_e$  between 0.08 and 0.12 at  $\lambda = 632.8nm$ . If %LB is greater than 2.8% the SPE regime is obtained and the shape of the extraordinary index is graded with a maximum  $\Delta n_e = 0.03$  at  $\lambda = 632.8nm$ . The region named MPE is a combination of the other two regimes and shows an index shape intermediate between the step and the graded index.

The PE waveguide allows to obtain strong field confinement improving in this way the non linear and electro-optic effect efficiency, which depends on the local intensity. Unfortunately, these advantages are canceled by the reduction of the non linear and electro-optic coefficients. Contrary to what happens for SPE waveguides, even if the mode is weakly confined, the optical quality provides low propagation losses and preserves the non linear and electro-optic properties of the substrate. The

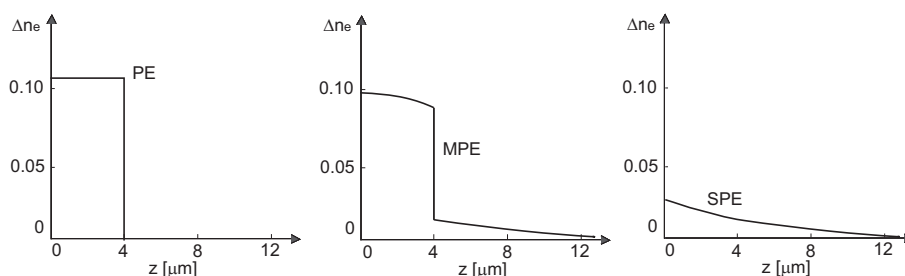


Figure 3.3: Refractive index profile in the depth direction for three different ranges of the LB percentage: (a) PE: ( $0 < \%LB < 1\%$ ), (b) MPE: ( $1 < \%LB < 2.8\%$ ) and (c) SPE: ( $\%LB > 2.8\%$ ).

PE and MPE waveguide properties can be improved through an annealing process. This process is then known as APE (Annealed Proton Exchange). The annealing process consists in warming up the sample in a oven at temperature higher than that of the exchange. The  $H^+$  ions diffuse deeply into the crystal lattice modifying the step profile into a graded one and improving the overall optical qualities. The relation between the proton concentration and the optical quality of the waveguide is quite complex to obtain. Different models have been proposed in [70] and [69]. The crystallographic analysis with X rays and the study of the spectral emissions in the infrared after the exchange have been demonstrated to be of primary importance. The analysis of many optical waveguides with different exchange and annealing parameters allowed to identify seven crystallographic phases of the proton exchanged Lithium Niobate. They are indicated with  $\alpha$ ,  $\kappa_1$ ,  $\kappa_2$ ,  $\beta_1$ ,  $\beta_2$ ,  $\beta_3$ ,  $\beta_4$ . These phases can be evidenced by plotting the component  $\epsilon_{33}$  of the stress tensor of the crystal as a function of the step index  $\Delta n_e$ . The deformation  $\epsilon_{33}$  result almost proportional to the proton concentration.

In figure 3.4 the phase diagram is reported. For each phase the variation function is almost linear but the slopes are different. The  $\alpha$  phase present small  $\Delta n_e$  and  $\epsilon_{33}$  and is obtained with the SPE process. This confirms the fact that with a SPE waveguide the non linear and the electro-optic coefficients are preserved.

The other two parameters of the SPE processes, temperature and exchange time  $T_{spe}$ , influence the size of the diffused layer. P. Aumont [71] in his PhD thesis analyzed the contribution of this parameter in order to fabricate devices with good optical quality. The high temperature increases the speed of the process and reduces the number of dislocations introduced in the crystal during the process. A property of Lithium Niobate is the ability to preserve its regular crystal structure also at high temperatures. The limit temperature of Lithium Niobate is  $T_{Curie} = 1253^\circ\text{C}$  that allows to adopt high temperatures fabrication processes for the device fabrication. In our case the limit is  $300^\circ\text{C}$  imposed by the fabrication technologies. The exchange time acts on the  $n_{eff}$  of the propagating mode with two antagonistic phenomena. The former is the improvement of the exchanged layer and the latter is the reduction

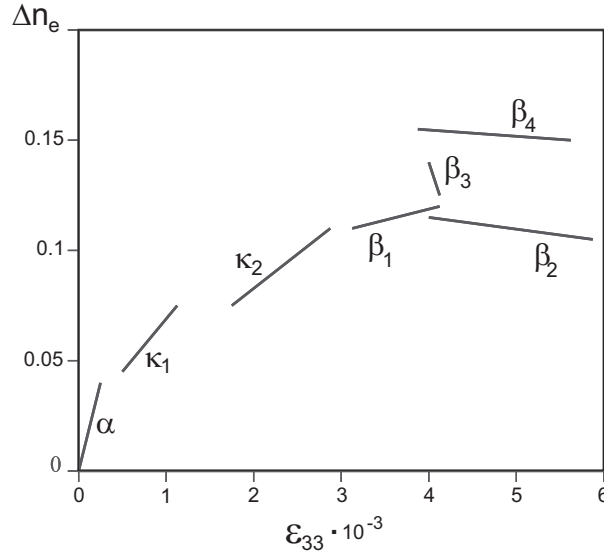


Figure 3.4: Phase diagram for the proton exchanged Lithium Niobate crystal.

of the  $\Delta n_e$ . The higher  $n_{eff}$  can be obtained with exchange time of three days (72 hours).

In order to fabricate the SPE waveguide, we have used the immersion technique that consists in using an ampoule with a throttling in the center. The proton source is placed in the lower part of the ampoule while the masked Lithium Niobate crystal in the upper part (throttling prevents the contact between the two components). The ampoule is then connected to a vacuum pump that can create the desired depressurization. After that the ampoule is closed with a flame. The ampoule is then placed into an iron pipe which protect the environment in the case of explosion and provide an important thermic inertia. The pipe is then placed in the oven at the temperature of  $300^\circ C$ . The fusion temperature of the Benzoic acid is  $160^\circ C$  while for the Lithium Benzoate LB it is much more higher than  $300^\circ C$ . Fortunately, LB is soluble in the liquid Benzoic acid and in this way we obtain a liquid mixture. When the temperature is stabilized we can just turn the pipe in order to put the sample and the proton source in contact. From this moment the exchange begins. After 72 hours we turn off the oven and the pipe is turned once again. When it is cold the sample can be taken out.

### 3.4 Photolithography

In order to fabricate segmented waveguide devices it is necessary to control the diffusion process. This can be done by masking the surface of the Lithium Niobate using photolithography. This word, which in Greek means “writing on a stone with

light”, is used to describe the process by which patterns on a  $LiNbO_3$  substrate can be defined using light. The absence of dust is an essential condition to obtain good results from this technique and for this reason all the step we are going to illustrate are made in the clean room of the Centre de Recherche sur l’Hétéro-Epitaxie et ses Applications (CRHEA) of Valbonne-Sophia-Antipolis with the collaboration of Sorin Tascu (post doctorate at the LPMC of the university of Nice Sophia Antipolis). A schematization of the different steps is shown in figure 3.5. Before the

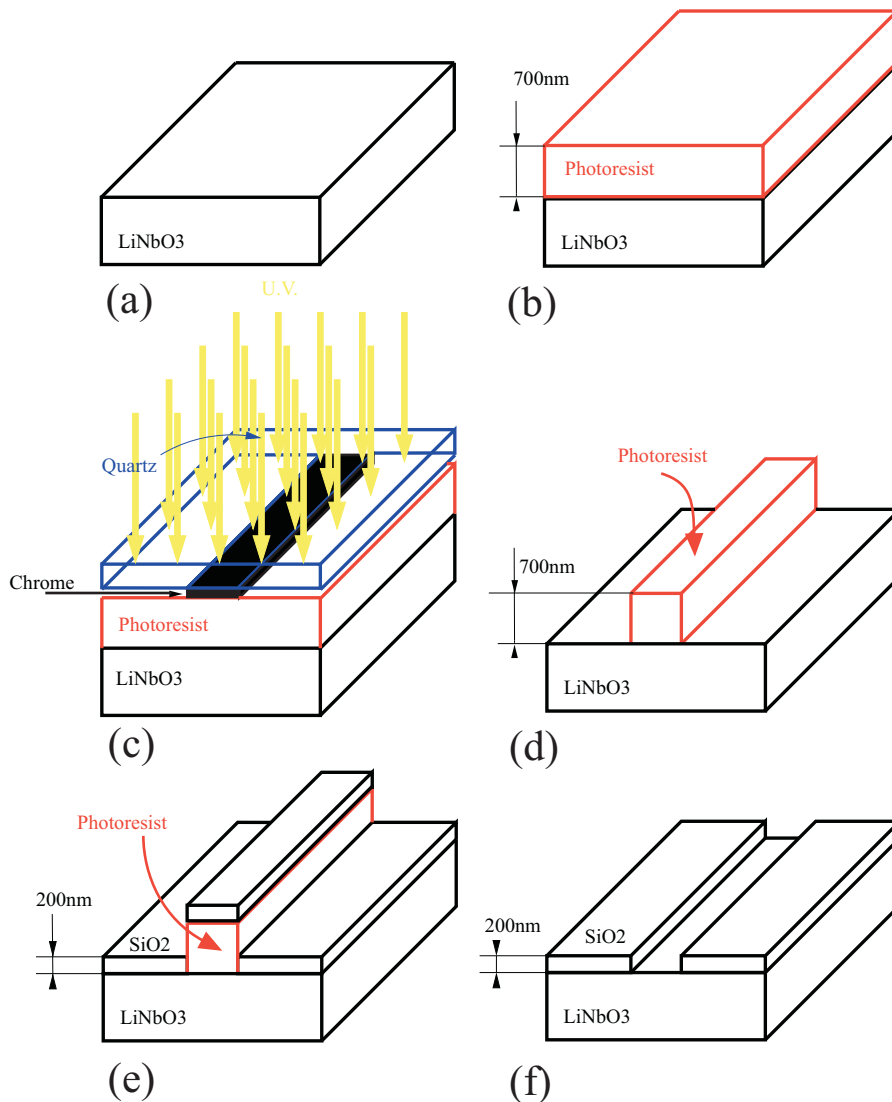


Figure 3.5: Schematization of the photolithography process.

photoresist is applied to the substrate, the surface is cleaned to remove any traces of contamination from the surface of the wafer such as dust, organic, ionic and metal-

lic compounds. The cleaned wafer is subject to priming, to aid the adhesion of the photoresist to the surface of the substrate material.

A 700 nm thick layer of photoresist is applied to the surface using a spin-coating machine (figure 3.6). This device holds the wafer of semiconductor, using a vacuum pump, and spins the photoresist at high-speed for a period of 15-30 seconds. A small quantity of photoresist is put on the center of the spinning wafer. The rotation causes the photoresist to be spread across the surface of the wafer with excess being thrown off. Preparation of the photoresist is concluded by a bake, where the wafer is heated in a oven to partially solidify the photoresist.



Figure 3.6: Picture of the spin coating machine used for the photoresist deposition on the wafer.

The photomask with the shape of our optical devices is created by a photographic process and developed onto a quartz substrate for its mechanical and optical properties.

Alignment between photomask and wafer is critical and must be achieved in  $x$  and  $y$  directions as well as rotationally. Photolithography machines use pattern recognition to achieve a so precise alignment (figure 3.7).

During the exposure process, the photoresist undergoes a chemical reaction. Depending on the chemical composition of photoresist, it can react in two ways when the light strikes the surface. The action of light on a positive photoresist causes it to become polymerized where it has been exposed to the light. A negative photoresist has the reverse property. Exposure to UV-light cause the photoresist to decompose. Preliminary experiments have shown that using a negative photoresist all the dimensions of our structures are reduced by about  $1\mu m$  respect to the photomask reference. This is the reason for which we have fabricated our device using a positive photoresist.

After the develop process the sample is ready for the deposition of 200nm thick  $SiO_2$  layer over all the surface of the wafer. The final  $SiO_2$  mask is obtained with a lift-off process which removes the resit through chemical reaction.



Figure 3.7: Picture of the photolithography machines used for the UV exposition.

### 3.4.1 Photomask design

To draw the photomask we have used Wavemaker [72]. This commercial CAD provides a graphical interface to realize the schematic of optical components, allowing to save the final draft in the standard format (.gds) used by the facilities which produce photomasks. In our case the photomask has been fabricated by Photonics (UK) [73].

Segmented waveguides and tapers are structures constituted by hundreds of segments, each one with different size depending on the device parameters (taper length, width,  $DC$  etc.). It is, therefore, impossible to draw this kind of photomask for a three inches wafer adopting the standard “cut and paste” procedure or similar commands available in the CAD. We have then used the scripting language available in Wavemaker in order to automatize the photomask preparation. In this way, all the “draw” command can be given through an external file instead of the standard graphic interface. We have developed a Fortran program that acquires the descriptions of all the devices we want to put in the photomask from an input file (.txt). This input file follows rules fixed by us, without entering in the details of the single segments. After the execution of our program we obtain a command file (.cmd) compatible with the scripting language of Wavemaker and a control file (.log) which summarizes all the parameters of the plotted devices. A flow chart of this process is shown in figure 3.8

This tool has been very useful during the photomask preparation allowing to obtain very fastly the desired results correctly.

A very important parameter to take into account during the photomask design is the distance to maintain between two neighbouring devices, fabricated on the same substrate, in order to avoid unwanted interferences but at the same time preserving

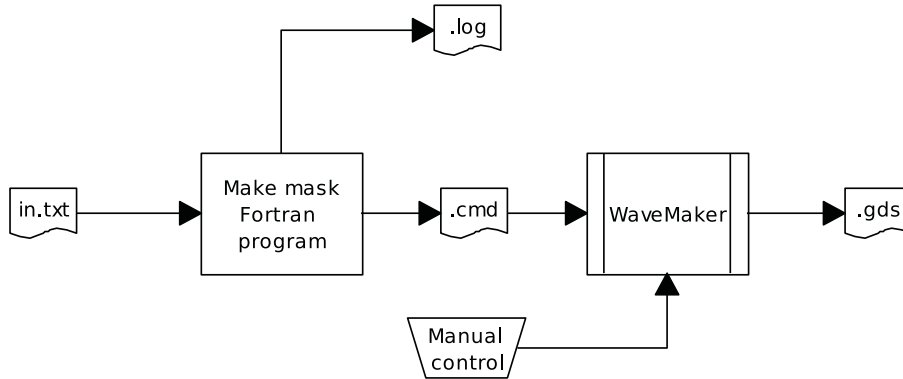


Figure 3.8: Schematization of the photomask preparation using the numerical tools implemented to interface with the CAD Wavemaker.

space. The problem can be resolved by making a study on the coupling interaction occurring between integrated optical waveguides with the complication that in our case the coupled waveguides are segmented.

The coupling phenomena is strongly related to the evanescent tails of the two electromagnetic modes that propagate in the waveguides and must be accurately evaluated. For this reason, we have adopted the 3D BPM for the numerical analysis of this problem. In this case, we can not apply the equivalent waveguide theorem and adopt the mode solver to obtain a precise evaluation of the coupling. The reason is that during the propagation the mode is modulated by the periodic structure [74]. This modulation is not present when modelling the segmented waveguide with an equivalent continuous waveguide: as a consequence, the coupling effect would be perturbed.

The analysis we have made consists in evaluating the coupling effect simply changing the distance between two parallel segmented waveguides. The worst case happens when the field is less confined and the overlap between the two modes is then more important. As a consequence, for the segmented waveguide parameters, we have considered the less confined structure with period  $P = 25 \mu m$ , duty cycle  $DC = 0.4$  and waveguide width  $W = 5 \mu m$  and working wavelength equal to  $1.55 \mu m$ . Using the BPM it is possible to evaluate the power evolution in the two waveguide in the propagation direction  $z$ <sup>1</sup> and then obtain the coupling length  $L_c$ . Figure 3.9 shows the power distribution for two segmented waveguides placed at the center to center distance  $d = 10 \mu m$ .

For the same structure in figure 3.10 the field distributions in horizontal and vertical sections are shown. Note that the energy can completely be transferred from one guide to the other one as the two segmented waveguide are identical.

Repeating the simulation for different distances  $d$  between the two segmented

<sup>1</sup>Note that in the following,  $z$  will refer to the propagation direction, which is different to the crystal axis  $Z$  of the Lithium Niobate substrate

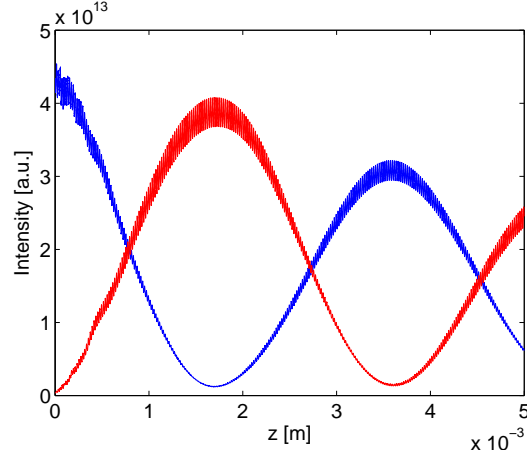


Figure 3.9: Power evolution in the two segmented waveguides for  $d = 10\mu m$ .

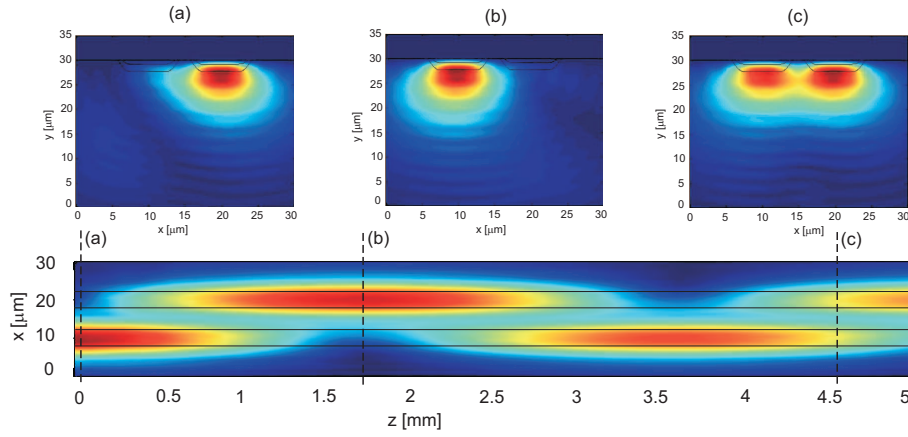


Figure 3.10: Field distribution in two neighbouring segmented waveguides. For  $z = 0$  (a) all the energy is in the right waveguide, then for  $z = L_c$  (b) the energy is completely transferred to the left waveguide, in (c) the coupler is balanced.

waveguide and evaluating the corresponding values of  $L_c$  we obtained the result plotted in figure 3.11. Imposing, as a condition for the optical isolation of the two waveguides, that less than 1% of the power can be transferred after a propagation of  $L_{smp} = 3\text{ cm}$ , it is possible to calculate the minimal coupling length allowed as:

$$\sin^2 \left( \frac{\pi \cdot L_{smp}}{2 \cdot L_c} \right) \leq 0.01. \quad (3.6)$$

This condition fixes  $L_c \geq 0.471\text{ m}$ . From figure 3.11 one can see that this condition imposes a minimal distance between the waveguide  $d \geq 49.7\ \mu m$ . As fabrication imperfections can improve the coupling phenomena a security margin must be considered. In our photomask we have then considered a distance  $d = 60\ \mu m$ .

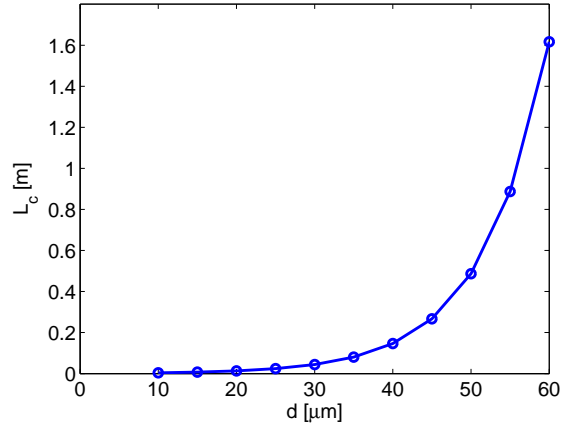


Figure 3.11: Coupling length versus the distance center to center  $d$ .

### 3.5 Fabrication results

After the proton exchange, the sample is extracted from the ampoule and cleaned with acetone and alcohol to get rid of the remaining acid. The deposited mask of  $SiO_2$  is eliminated immersing the sample in BOE acid. Observing the sample with a microscope in transmission or reflection (figure 3.12) it is possible to recognize the waveguides from their increased refractive index. Observing the samples with the

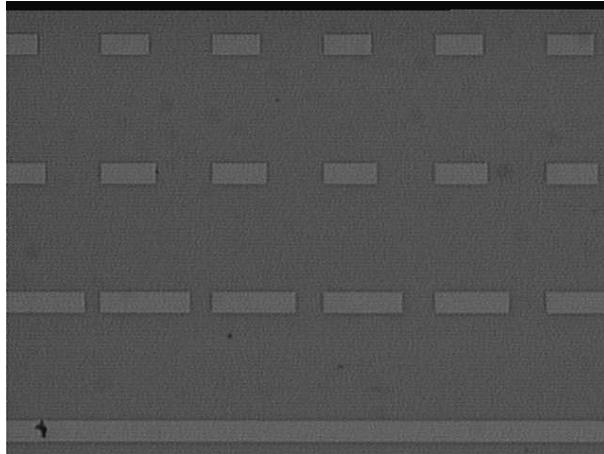


Figure 3.12: Microscope picture of fabricated waveguides obtained in reflection mode.

microscope in dark field we obtain the results shown in figure 3.13. This technique consists in illuminating the sample with a light grazing to the sample surface. This then allows to evidence the presence of scattering sources. For a perfect surface we should obtain a completely dark image. In our case, however, we can note that the

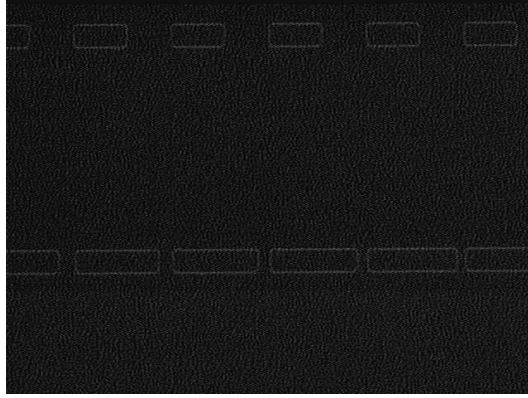


Figure 3.13: Dark field image of two fabricated segmented waveguide.

edges of our waveguides are visible. This result shows the presence of bulges or sinks in the contour of the exchanged zones. This problem has required a more advanced analysis. Using a AFM (Atomic Force Microscope) Sorin Tascu (post doctorate at the LPMC of the university of Nice Sophia Antipolis) confirmed the presence of sinks of about 50 nm of depth. This phenomenon clearly increases the propagation losses of continuous and segmented waveguides. We report in the following table the propagation losses of our fabricated waveguides. The measurement technique adopted for this characterization will be described with more details in the next chapter.

	$P = 15\mu m$		$P = 25\mu m$	
$DC$	$W = 5\mu m$	$W = 7\mu m$	$W = 5\mu m$	$W = 7\mu m$
0.5	2 dB/cm	2.34 dB/cm	4 dB/cm	2.99 dB/cm
0.6	1.71 dB/cm	2.02 dB/cm	2.92 dB/cm	2.02 dB/cm
0.7	1.74 dB/cm	2.16 dB/cm	2.40 dB/cm	2.04 dB/cm
1	1.13 dB/cm	1.34 dB/cm	1.13 dB/cm	1.34 dB/cm

The possible causes to explain this roughness phenomena and the consequently elevated propagation losses respect to smaller expected values are:

- the crystal structure of Lithium Niobate is perturbed during the photoresist deposition;
- the crystal structure of Lithium Niobate is perturbed during the  $SiO_2$  deposition;
- the acid BOE attacks the Lithium Niobate surface during the elimination of the deposited  $SiO_2$  mask;
- the Lithium Niobate crystal structure is fragilized during the SPE process.

The first three possibilities have been rapidly excluded repeating the procedure of photoresist and  $SiO_2$  deposition on the Lithium Niobate substrate. We have then removed the two depositions with acetone and BOE to obtain a perfect surface without any kind of imperfections. The only remaining possibility is then that of the fragilization induced by the SPE. During the exchange the sample is subject to acid contact at high temperatures: this stress is probably too strong for the crystal structure. To confirm this hypothesis PE and APE waveguides have been fabricated as they require reduced exchange time. For both of them no defects appear on the surface. It is then necessary that future work will study in more details this phenomenon to allow fabrication of better quality SPE waveguides with low propagation losses.

### 3.5.1 M-lines characterization

One side of the sample during the SPE being unmasked is completely exchanged and the resulting increase of the refractive index forms a slab waveguide. The presence of this waveguide can be used to determine the optical properties of the device fabricated on the other side of the sample. Using the m-lines techniques [75], it is also possible, in fact, to measure the effective index of the propagating modes of the slab. Then, using the Inverse-WKB (IWKB) technique [76, 77] it is possible to reconstruct the refractive index profile in the vertical direction for the exchanged zones. With the m-lines technique it is also possible evaluate qualitatively the optical properties of the sample under test.

A schematic of the m-lines experimental setup is shown in figure 3.14.

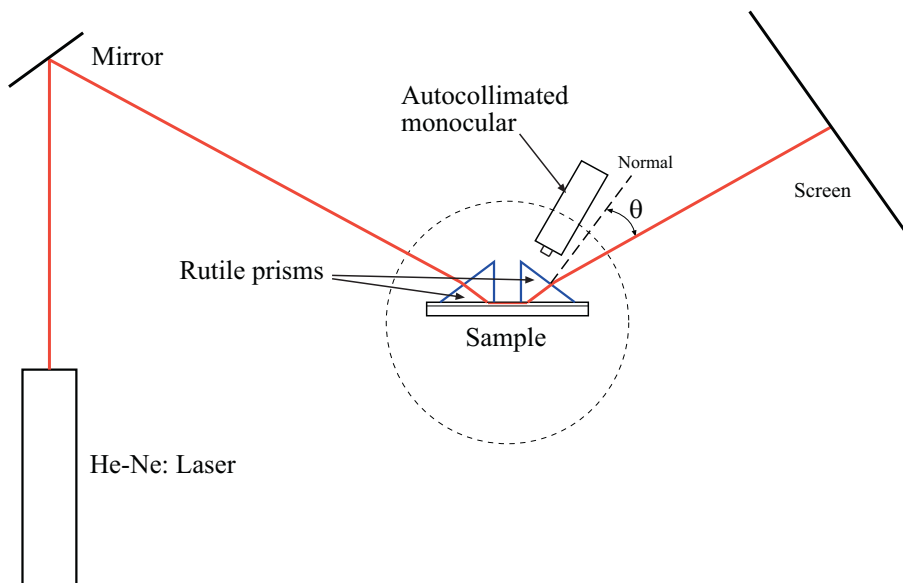


Figure 3.14: Experimental setup for the m-lines characterization.

Two rutile prisms are placed on the slab surface. A  $He - Ne$  laser emits a beam at 632 nm incident the input prism. Inside the prism the beam is total reflected by the interface with the slab waveguide. The total reflection in the prism is associated to an evanescent wave in the small air gap present at the interface between slab and prism. If the air gap is sufficiently small the evanescent field can be coupled into the waveguide slab when the phase matching condition between the two fields is satisfied. This condition can be achieved by modifying the entrance angle of the laser beam. Once the coupling condition is satisfied, the field can propagate into the slab and then can be out coupled by the second prism. Measuring the angle  $\theta$  that the output beam forms with respect to the normal direction of the end face of the prism, it is possible to calculate the effective index of the propagating mode using the relation:

$$n_{eff} = n_{rutile} \cdot \sin \left[ \arctan \left( \frac{\sin \theta / n_{rutile}}{\sqrt{1 - \sin^2 \theta / n_{rutile}^2}} \right) + \theta_p \right]. \quad (3.7)$$

The measurement of this angle can be obtained using an autocollimated monocular which provides a very good resolution of  $\pm 0.015^\circ$ . The systematic error for the effective index measurement is then  $\pm 2.5e - 4$ .

The far field outgoing from the output prism, if projected on a screen, appears as bright lines (from this the name of the technique), which correspond to the excited modes, and a superposed bright point. This image carries the information on the optical quality of the sample. In particular the considered evaluation methods are:

- Width of the bright line: this properties allows to obtain information on the homogeneity of the slab waveguide in the out coupling region. In fact, if inhomogeneities are present, the propagating constant can be locally modified and fluctuations of the output angle appear. As a consequence the line appears large.
- Central point very bright: it proves that during propagation in the slab waveguide the laser beam has not been perturbed by diffusion. In this case propagation losses will be relatively small.
- Selectivity in the mode excitation: for the angle which satisfies the phase matching condition, just one mode must be in propagation and just one line must appear. The presence of energy in other modes at the same time proves intermodal coupling related to strong diffusion.

The first result obtained using the m-lines technique is the characteristic function of the SPE process. First of all, we have fabricated some slab waveguides with different percentages of LB with exchanges of 72 hours at a temperature of  $300^\circ C$ . The waveguides have been then characterized at 632 nm. Figure 3.15 shows the

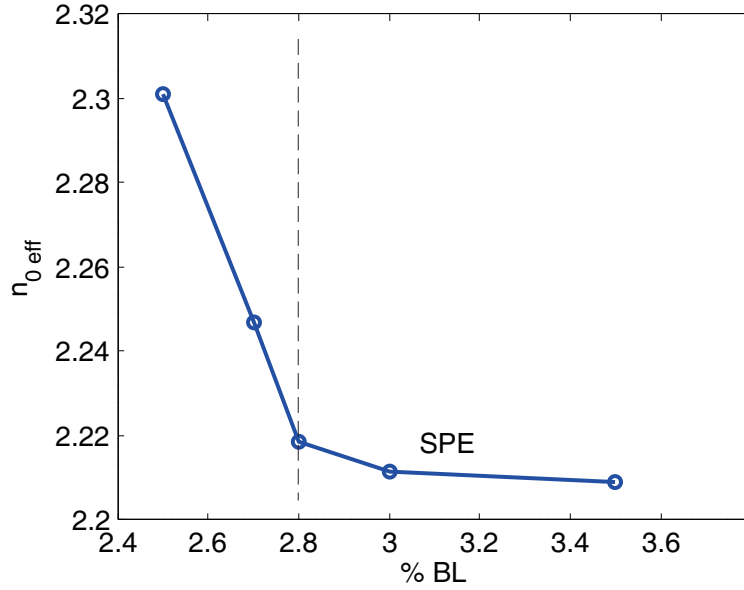


Figure 3.15: Effective index of the fundamental mode versus the percentage of LB for planar waveguide, deduced from the m-lines measurement at 632nm.

values of the effective index of the fundamental mode as a function of the percentage of LB. The high values of the effective index obtained with low percentages of LB are related to deeply perturbed crystalline structures. For LB percentages larger than the threshold value of 2.8%, the crystalline phase is not modified and we consider only this regime for the fabrication of our devices. This is the so called SPE regime.

Starting from the results obtained with the m-lines technique it is possible to identify the point of the index profile for which the effective index is equal to the local refractive index. This numerical elaboration can be made using the IWKB algorithm. A version of this numerical tools was available at the LPMC. Making an interpolation of the obtained point, it is possible to obtain the complete index profile. The precision of this interpolation depends on the number of the available points, i.e. the number of modes. With a *He – Ne* laser at 632 nm our waveguide presents 3 to 4 modes in the SPE regime. In the following table, we present the results obtained with the m-lines technique and the IWKB for slab waveguide fabricated with 2.8% and 3.5% of LB.

M-lines thecnique			IWKB
LB percentage	Angle [deg]	effective index @ $632.8\mu m$	Deep [ $\mu m$ ]
2.8 %	10.926	2.21848	1.48
	9.841	2.20874	2.651
	9.383	2.20459	4.882
	9.227	2.20318	8.93
3.5 %	9.888	2.20916	2.182
	9.374	2.20451	3.822
	9.181	2.20276	7.562

Using interpolation techniques we have reconstructed the two profiles shown in figure 3.16.

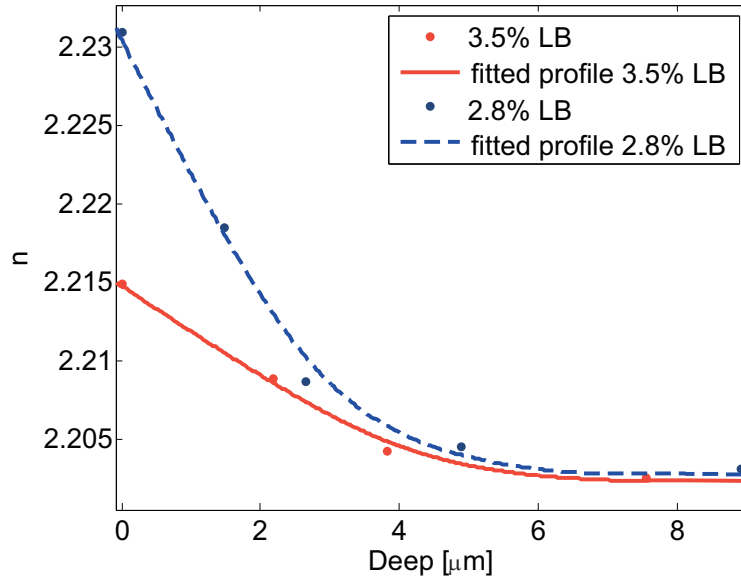


Figure 3.16: Index profile reconstructed using the IWKB algorithm after the m-lines measurement on SPE waveguide with different LB percentage: LB%=3.5 (red line), LB%=2.8 (blue dashed line).

## 3.6 Polishing

In order to couple energy into an optical waveguide different techniques have been developed. One of these solutions has been already presented describing the m-lines experimental setup. It consists in using two prisms as shown in figure 3.17. For channel waveguides this solution is very difficult to use as alignment is not simple. Another solution proposed in the past [78] uses diffracting gratings at the

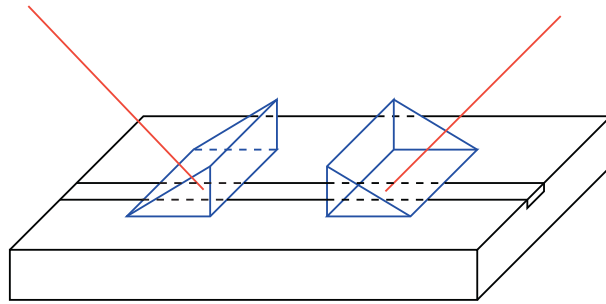


Figure 3.17: Scheme of the prism coupling technique.

two waveguide ends. The radiating characteristic of the grating allows to collect and emit the light with a particular angle respect the surface of the sample. The drawback of this solution (schematically shown in figure 3.18) is its complexity: it requires, in fact, the design of the gratings.

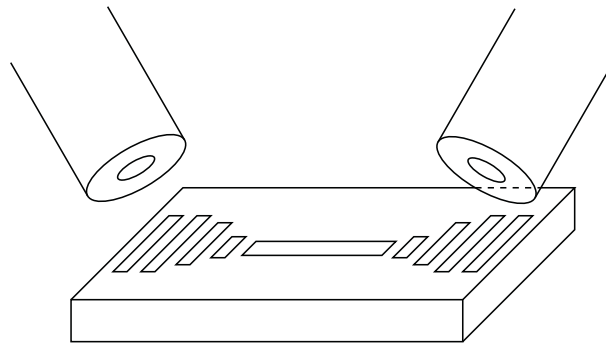


Figure 3.18: Scheme of out plane coupling through diffraction grating.

A further alternative to these solutions is the so called end fire coupling. In this technique the waveguide mode is directly coupled with the external components (fibers or microscope objective) through the end face of the sample. The advantage

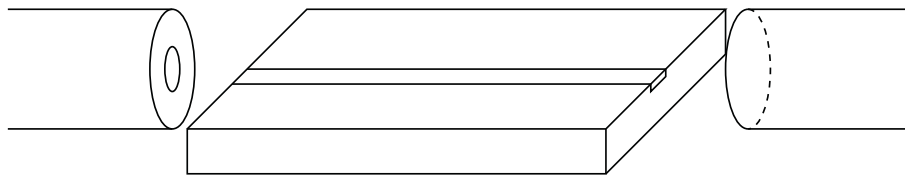


Figure 3.19: Scheme of end fire coupling.

of this solution is that it does not require additional structures in the optical device and the alignment is quite simple to obtain. The drawback is that the two end faces must be polished before the characterization of the sample, adding a further step in the fabrication process and that radiating mode of the structure can be excited.

The polishing technique we have used consists to fix vertically the sample between two piece of glass inside a metallic support. The presence of the two pieces of glass provides a better stability to the sample and improves the edge quality. The metallic support is then mounted into a Sample Mounting Fixture (SMF) to apply uniform pressure to the sample during polishing. The SMF is then placed on a rotating plate and its position is controlled by a mechanical arm. Suitable abrasive products must be put on the plate to improve grinding and polishing of the sample end face. In our case, we have adopted dust of alumina mixed in water. The procedure consists to start the polishing with big grains of alumina for an approximative result since using small grain of alumina and a chemical attack for the final step. The table summarizes the polishing time corresponding to the size of the alumina grains adopted:

Step	Alumina size [ $\mu m$ ]	Time [min]
1	20	15
2	9	30
3	5	30

The polish procedure with alumina is only mechanical and can be realized with a machine shown in the left part of figure 3.20. The last step requires a more accurate



Figure 3.20: Pictures of the two polish machine used for the alumina (left) or chemical (right) step.

surface polishing and can be obtained using a particular plate (see right part of figure 3.20), adding a liquid product that attacks chemically the end face of the sample. Care is required to avoid the presence of big grains that can produce deep scratches which would prevent good quality samples.



# 4

## Characterization techniques

### 4.1 Introduction

Once devices have been fabricated, they must be characterized to measure the most important parameters which determine their performances. For linear devices, propagation losses, effective group index  $N_{eff}$  and mode size of the propagating field are among the most important ones, as they influence maximum allowed device length, dispersion properties and coupling efficiency with other components. Measurements techniques should be precise, simple to manage, non destructive and allow easy upgrade to guarantee the accuracy and sensitivity required by the continuous technology advancements. The purpose of this chapter is that of presenting, after a rapid summary of the measurement techniques proposed so far, the main features of an all-in-one experimental set up [79] with specific mention to the values of precision we obtained. Then, to show its proper functioning and versatility, measurement result on different devices (fiber and integrated optical waveguide), will be reported and discussed.

### 4.2 Measuring attenuation, effective group index and mode size

As mentioned in the introduction, we are interested in measuring propagation losses, effective group index and mode size of the propagating field in the linear devices we have fabricated to evaluate the overall device performances. In order to evaluate such parameters, different measurement techniques have been proposed in the past, but each of them allows one measurement at a time, which may be a problem when these features should be evaluated for the same device. It is then worthwhile to rapidly summarize the different techniques proposed so far, illustrating advantages and problems in order to show how it is possible to unify all of them in a single set up.

Propagation losses can be evaluated in a conceptually very simple way using the so called insertion losses technique [80]. The Device Under Test (DUT) is inserted between two identical fibers. The transmitted power is measured and attenuation is obtained comparing this value to that resulting from direct connection of the two fibers. Such technique is conceptually very simple, but requires the knowledge of the overlap integral between the fiber mode and that of the DUT input and output sections. Moreover, systematic errors can come from alignment problems and possible formation of parasitic air cavities between the fiber and the sample interface that can perturb the transmission power measurement. Some of these problems are eliminated by the so called back coupling method [81]. This technique assumes that all guided field outgoing the DUT can be reflected and coupled back into it by a proper optical system. If such an operation is lossless, only Fresnel losses occur. Overall transmission losses can then be determined comparing the intensities of the launched beam and that of the back reflected light after double passing the DUT. The precision of this technique critically depends on the quality of both the input beam splitter and the output reflecting optical system. A further method is based on the assumption that the power laterally scattered by the DUT is linearly proportional to the guided one. Measuring its evolution during propagation (with a camera or any other sensor) allows an indirect evaluation of DUT attenuation [82, 74]. This measurement technique is simple, but has problems both in high loss devices because of the presence of scattering centers and in low loss devices, where very long samples are required for loss evaluation. A fourth method used for propagation losses measurement is the so called Fabry-Perot resonance technique [83]. The sample acts as a cavity whose quality factor and finesse depend on the propagation losses. A tunable laser source with narrow linewidth allows spectral characterization of the cavity parameters providing also its propagation losses, after some data processing. This technique requires careful sample preparation and alignment procedures to avoid again parasitic air cavities outside the DUT. It works well for low losses measurements (under 3-4 dB/cm) and its precision depends on the sample length.

The second parameter to be measured is the effective group index  $N_{eff}$  of a propagating mode [84], which establishes the dispersive behavior of an optical waveguide. Fiber suppliers are interested in such a parameter and many measurement setups have been then proposed so far: for example, the so called time of flight measurement [85, 86] or other interferential techniques [87, 88]. But they are not fully general as they cannot be used for integrated optical devices. Today, the interest for measuring such a parameter is still strong as, for example, photonic crystal waveguides [89, 90, 91, 92] can be used for slow light guidance [93, 94] and the  $N_{eff}$  measurement is then fundamental for their characterization. A method to evaluate  $N_{eff}$  in integrated optical waveguides is based on a spectral measurement of the field mode size [95, 96]. The precision of this method depends on the accuracy of the mode size measurement and on how good is the approximation of the relation

between the waveguide dispersion and the mode size. A different approach is based on the characterization of the Fabry-Perot cavity formed by the sample, as previously discussed talking about propagation loss measurements. In this case, in fact, the distance between the resonance peaks depends on the value of  $N_{eff}$  [97].

Finally, the field distribution of the modes guided by the DUT is most of the time obtained by measuring the near field by a camera [98]. Problems of this setup come from nonlinearity and inhomogeneity of the sensor, aberrations of the lens used to magnify the near field image and difficult calibration of the whole measurement setup. To overcome these problems, the near field is evaluated scanning the DUT end-face with a  $1\text{-}\mu\text{m}$ -diameter pinhole in a  $2.5\text{-}\mu\text{m}$ -thick steel sheet mounted on a single-mode fiber connected to the detector [99]. The price to pay is a much longer measurement time, requiring setup and source thermal stabilization. Far field measurements and subsequent Hankel transform to reconstruct the near field have also been proposed [100]. They eliminate the risks connected to close and moving parts, which may damage optical surfaces, but are not precise, as the evanescent part of the plane wave spectrum composing the near field is not present in the far field and so the field reconstruction is not precise.

As one can see, measurement procedures to evaluate all these parameters are cumbersome, time consuming and are affected by systematic errors depending on each particular setup. So we have conceived and realized an all-in-one measurement setup to evaluate propagation losses, effective group index  $N_{eff}$  and mode size of the propagating field of both optical fibers and integrated optical waveguides. This solution, which will be described in the next section, reduces measurement time, saves space and allows optimizing all the setup parameters only once, thus providing measurements results affected by the same measurement errors. This also allows simpler upgrade to higher measurement precision, when needed.

The setup is conceived also to collect all the best features of the previously illustrated ones. The loss and effective group index measurement principle is based on the Fabry-Perot cavity. The mode size measurement is based on the idea proposed in [99], but with improvements in terms of precision of the results and simplicity of the experimental setup because only a monomode fiber has been used to perform the scan.

## 4.3 Experimental setup

The schematic of the measurement setup is shown in figure 4.1. The laser source is a tunable external cavity laser emitting between  $1.5\ \mu\text{m}$  and  $1.6\ \mu\text{m}$  (NetTest Tunics Plus) with an automatic power control system and a linewidth as narrow as 150 kHz. To allow polarization controlled measurements, the laser output is connected to a polarization maintaining fiber, monomode at the working wavelengths. The other fiber end is fixed on a piezoelectric positioning system. Such system allows

controlling the position of the fiber on the  $x$ - $y$  plane in a range of  $25 \mu\text{m} \times 25 \mu\text{m}$  with step of 16 nm. With micrometric controls, it is also possible to adjust the horizontal ( $\Theta_h$ ) and vertical incidence angles ( $\Theta_v$ ) of the fiber with respect to the optic axis. On the other side of the DUT, a SMF28 fiber is fixed on a similar piezoelectric positioning system with the same features as the previous one in order to collect the output signal. The SMF28 fiber output is connected to an InGaAs detector for the intensity measurement. The piezoelectric stages and the detector are connected to a control station that allows the interface with a Personal Computer (PC) through a GPIB port. A Labview® [101] program controls all the measurements and provides

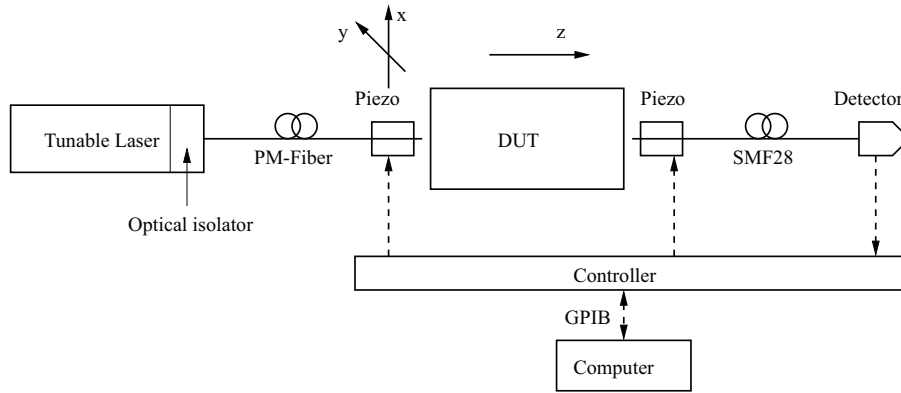


Figure 4.1: Schematic of the all-in-one experimental setup to measure propagation losses, effective group index and mode size of an optical fiber or an integrated optical device (DUT: Device Under Test).

rapid and reproducible data collection. The remote control of the measurement from the PC offers many advantages, not only related to increased reproducibility and precision. For example, there is no need for operators to get close or touch the components. This avoids mechanical changes due to temperature variations in the setup, which are critical when long measurements must be performed. Figure 4.2 shows a screenshot of the program interface. The DUT is surrounded by air and its end-faces form a Fabry-Perot cavity. As said before, once the cavity parameters are known, values of both propagation losses and  $N_{eff}$  can be obtained. Moreover, the possibility to scan the output section of the DUT by moving the SMF28 fiber allows also obtaining information on the shape of the field that propagates through the sample. In the following subsections, more details on the different measurement techniques integrated in this setup will be provided.

### 4.3.1 Loss measurements

The Fabry-Perot based technique to evaluate propagation losses  $L$  is based on the fact that the guided mode of the DUT is partially reflected at the end-faces of

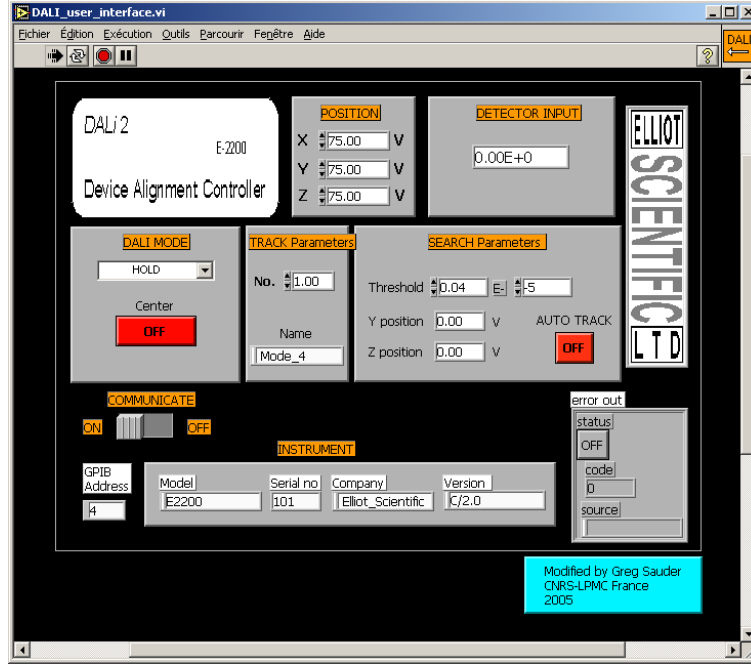


Figure 4.2: Screenshot of the Labview® program used to control the experimental setup.

the sample. This is due to the difference between the refractive index of air and the effective index of the propagating mode,  $n_{eff}$ , defined as the ratio between the propagation constant  $\beta$  and the wavenumber  $k_0$ . The waveguide behaves then as a resonant cavity and modes propagating in both directions interfere according to their relative phases. Resonance conditions depend on wavelength. Their periodic occurrence can be evidenced by a spectral scanning of the transmission characteristics. Such a transmission spectrum is characterized by the so called contrast  $C$ , which is defined as:

$$C = \frac{I_{\max} - I_{\min}}{I_{\max} + I_{\min}} \quad (4.1)$$

being  $I_{\max}$  and  $I_{\min}$  the maximum and the minimum output intensities respectively. Assuming orthogonally polished end-faces with respect to the waveguide, the propagation losses  $L$  (evaluated in dB) can be obtained by measuring  $C$  and using [83]:

$$L = 4.34 \left[ \ln \frac{1 - \sqrt{1 - C^2}}{C} - \ln(R) \right] \quad (4.2)$$

where  $R$  is the end-face (Fresnel) reflection coefficient:

$$R = \frac{(n_{eff} - 1)^2}{(n_{eff} + 1)^2}. \quad (4.3)$$

Using the experimental setup of figure 4.1, the contrast measurement is performed by varying the signal wavelength of the laser and recording the detected output intensity. The minimum and the maximum of measurement coincide respectively with  $I_{\min}$  and  $I_{\max}$  of 4.1. In order to obtain a correct measurement, some conditions should be fulfilled. First of all, the laser must be stable in power and wavelength and no mode-hopping should occur. This is true for the NetTest Tunics Plus laser using APC fiber connectors we used. Moreover, the only cavity of the system must be formed by the DUT. Thus, the input and output fibers must be tilted with respect to the waveguide at an angle in order to eliminate the parasite air cavities formed by the end-faces of the sample and the fibers. In our setup, both the tilt angles were set to  $\Theta_h = \Theta_v = 2^\circ$ . These non perfect alignments contribute however to increase the coupling losses with the sample, though they do not perturb the contrast measurement. In order to check this, we realized a contrast measurement of an integrated optical waveguide, maintaining or not the output fiber perfectly aligned to the optical axis. Figure 4.3 shows the effect of the distance between the output fiber and the end-face of the sample on the output intensity when a wavelength scanning is performed. The left part of figure 4.3 refers to the case of fibers with no tilt. The contrast changes abruptly, when, during the wavelength scanning, at 1550.1 nm, we have modified the distance. The right part of the same figure reports the results obtained, with the same procedure, when the fibers are tilted. In this case the intensity varies, but there is no change in the contrast.

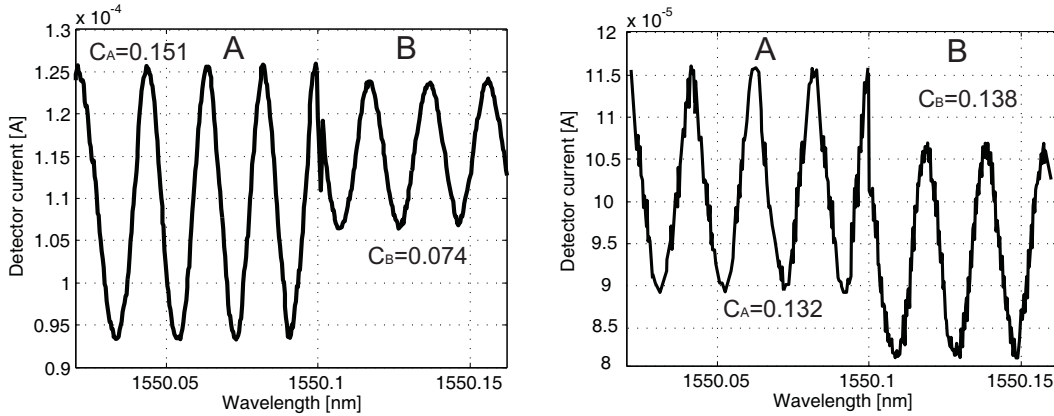


Figure 4.3: Interference fringes of a Fabry-Perot cavity obtained with fibers aligned (left) or not (right) to the waveguide. Regions A (before 1550.1 nm) and B (after 1550.1 nm) refer to different distances between the output fiber and the sample end-face.

A further problem in the correct evaluation of  $C$  comes from the possible presence of non zero angles  $\psi_{x,i}$ ,  $\psi_{y,i}$ ,  $\psi_{x,o}$ ,  $\psi_{y,o}$ , formed by the waveguide with the end-faces of the sample. Corrective terms must be introduced in 4.2 to take into account these

angles [80]:

$$R = \frac{(n_{eff} - 1)^2}{(n_{eff} + 1)^2} \cdot \sqrt{L_{x,i}L_{x,o}}\sqrt{L_{y,i}L_{y,o}} \quad (4.4)$$

In this equation

$$\begin{aligned} L_{x,i} &= e^{(-\beta_i^2 w_{y,i}^2 \psi_{x,i}^2)} & L_{x,o} &= e^{(-\beta_o^2 w_{y,o}^2 \psi_{x,o}^2)} \\ L_{y,i} &= e^{(-\beta_i^2 w_{x,i}^2 \psi_{y,i}^2)} & L_{y,o} &= e^{(-\beta_o^2 w_{x,o}^2 \psi_{y,o}^2)} \end{aligned} \quad (4.5)$$

being  $\beta_i$  and  $\beta_o$  the input and output wavevectors respectively, while  $w_{x,i}$ ,  $w_{x,o}$ ,  $w_{y,i}$ ,  $w_{y,o}$  are the mode size in the x and y direction at the input and output end face of the sample. As these angles can be easily evaluated with a precisions of  $0.1^\circ$ , the effect of the angle measurements uncertainty on the determination of the propagation losses can be practically eliminated. In conclusion, the main contribution to the overall measurement error comes from the noise introduced by the acquisition system when evaluating the contrast  $C$ . Note however that, contrary to what happens using most of the classical methods of measuring waveguide losses, the error decreases for decreasing attenuation as the contrast increases accordingly. For devices with very low propagation losses the limit of this technique then comes basically from the precision determining the  $n_{eff}$  of the propagating mode and the noise of the experimental setup for the contrast evaluation. This noise depends on the adopted setup and its evaluation can be obtained by repeating the same measurement and observing the dispersion of the results. With our setup, exploiting the features of the remote control, we obtain a fluctuation of the contrast value in reaped measurements of just 0.5%.

### 4.3.2 Group index and dispersion measurements

With the same configuration of the experimental setup used for loss measurement we can obtain also the effective group index  $N_{eff}$  of the propagation mode in a waveguide, with  $N_{eff}$  defined as:

$$\frac{c}{v_g} = N_{eff}(\lambda_0) = n_{eff}(\lambda_0) - \lambda_0 \frac{\partial n_{eff}(\lambda_0)}{\partial \lambda_0} \quad (4.6)$$

where  $c$  is the speed of light in vacuum,  $v_g$  is the group velocity and  $\lambda_0$  is the free space wavelength. As we can see,  $N_{eff}$  takes into account both propagation and dispersion characteristics. The value of  $N_{eff}$  comes from the knowledge of the free spectral range  $\Delta\lambda$  of the transmission spectrum [84]. To determine the relationship between  $N_{eff}$  and the measurement results, one can start from the resonance conditions corresponding to maximum power transmission:

$$2 \cdot \frac{2\pi}{\lambda_0} \cdot n_{eff}(\lambda_0) \cdot L = 2m\pi \quad (4.7)$$

where  $L$  is the sample length and  $m$  is an arbitrary integer constant. At  $\lambda_0 + \Delta\lambda$  it then holds:

$$2 \cdot \frac{2\pi}{\lambda_0 + \Delta\lambda} \cdot n_{eff}(\lambda_0 + \Delta\lambda) \cdot L = 2(m - 1)\pi. \quad (4.8)$$

Subtracting 4.8 from 4.7 and considering  $\Delta\lambda \ll \lambda_0$  we get:

$$\begin{aligned} 1 &= \frac{2}{\lambda_0} n_{eff}(\lambda_0) L - \frac{2}{\lambda_0} \left(1 - \frac{\Delta\lambda}{\lambda_0}\right) \left(n_{eff}(\lambda_0) + \Delta\lambda \frac{\partial n_{eff}(\lambda_0)}{\partial \lambda_0}\right) L = \\ &= \frac{2L \cdot \Delta\lambda}{\lambda_0^2} \left(n_{eff}(\lambda_0) - \lambda_0 \frac{\partial n_{eff}(\lambda_0)}{\partial \lambda_0}\right) = \frac{2L \cdot \Delta\lambda}{\lambda_0^2} N_{eff}. \end{aligned} \quad (4.9)$$

Measuring  $\Delta\lambda$  and the sample length, we then can then calculate  $N_{eff}$  as:

$$N_{eff} = \frac{\lambda_0^2}{2L \cdot \Delta\lambda}. \quad (4.10)$$

The relative error  $E_r$  of this measurement is:

$$E_r(N_{eff}) = 2 \cdot E_r(\lambda_0) + E_r(L) + E_r(\Delta\lambda) \quad (4.11)$$

where  $E_r(\lambda_0)$ ,  $E_r(L)$  and  $E_r(\Delta\lambda)$  are respectively the relative errors associated to the values of  $\lambda_0$ ,  $L$  and  $\Delta\lambda$ . In this equation  $E_r(L)$  is determined by the instrument used to evaluate the length of the sample,  $E_r(\lambda_0)$  is defined as the ratio between the laser linewidth and  $\lambda_0$  while  $E_r(\Delta\lambda)$  can be calculated as:

$$E_r(\Delta\lambda) = \frac{2\delta}{\Delta\lambda} \quad (4.12)$$

where  $\delta$  is the wavelength resolution of the laser.  $E_r(\Delta\lambda)$  can be reduced considering two resonances separated by more than one period  $\Delta\lambda$  or using a laser with better resolution. Both  $E_r(\Delta\lambda)$  and  $E_r(\lambda_0)$  depend on the precision on the laser wavelength but in our case  $E_r(\lambda_0)$  is negligible respect to  $E_r(\Delta\lambda)$  because of the narrow linewidth of the laser. In many cases, it may also be of interest to know the wavelength dependence of the effective group index  $N_{eff}$  as it is related to the second order dispersion of the effective index. In fact, deriving equation 4.6 with respect to  $\lambda_0$  one obtains:

$$\frac{\partial N_{eff}(\lambda_0)}{\partial \lambda_0} = \frac{\partial n_{eff}(\lambda_0)}{\partial \lambda_0} - \frac{\partial n_{eff}(\lambda_0)}{\partial \lambda_0} - \lambda_0 \frac{\partial^2 n_{eff}(\lambda_0)}{\partial \lambda_0^2} = -\lambda_0 \frac{\partial^2 n_{eff}(\lambda_0)}{\partial \lambda_0^2} \quad (4.13)$$

which provides the desired relation:

$$\frac{\partial^2 n_{eff}(\lambda_0)}{\partial \lambda_0^2} = -\frac{1}{\lambda_0} \frac{\partial N_{eff}(\lambda_0)}{\partial \lambda_0}. \quad (4.14)$$

Repeating the  $N_{eff}$  measurement at different wavelengths and then calculating the slope of the interpolating function allows to show the possible presence of a zero

dispersion condition of the DUT. For example, considering the two wavelengths  $\lambda_{01}$  and  $\lambda_{02}$  (with free spectral ranges given by  $\Delta\lambda_{01}$  and  $\Delta\lambda_{02}$  respectively) and applying 4.10, the slope of  $N_{eff}(\lambda_0)$  is:

$$\begin{aligned} \frac{\partial N_{eff}(\lambda_0)}{\partial \lambda_0} &\approx \frac{N_{eff}(\lambda_{01}) - N_{eff}(\lambda_{02})}{\lambda_{01} - \lambda_{02}} = \frac{\frac{\lambda_{01}^2}{2L \cdot \Delta\lambda_{01}} - \frac{\lambda_{02}^2}{2L \cdot \Delta\lambda_{02}}}{\lambda_{01} - \lambda_{02}} = \\ &= \frac{\Delta\lambda_{02} \cdot \lambda_{01}^2 - \Delta\lambda_{01} \cdot \lambda_{02}^2}{(2L \cdot \Delta\lambda_{01} \cdot \Delta\lambda_{02})(\lambda_{01} - \lambda_{02})}. \end{aligned} \quad (4.15)$$

The evaluation of the relative error of 4.15 is more cumbersome than that of 4.10. From 4.15, after some algebra, one first gets:

$$\begin{aligned} E_r \left( \frac{\partial N_{eff}(\lambda_0)}{\partial \lambda_0} \right) &= E_r (\Delta\lambda_{02} \cdot \lambda_{01}^2 - \Delta\lambda_{01} \cdot \lambda_{02}^2) + \\ &+ E_r ((2L \cdot \Delta\lambda_{01} \cdot \Delta\lambda_{02})(\lambda_{01} - \lambda_{02})). \end{aligned} \quad (4.16)$$

This formula can be simplified. As said before,  $E_r(\lambda_0)$  is negligible with respect to  $E_r(\Delta\lambda)$ . This allows to consider  $\Delta\lambda_{01}$  and  $\Delta\lambda_{02}$  constant and develop the first term of 4.16 as:

$$E_r (\Delta\lambda_{02} \cdot \lambda_{01}^2 - \Delta\lambda_{01} \cdot \lambda_{02}^2) = \frac{2\delta (\lambda_{01}^2 + \lambda_{02}^2)}{\Delta\lambda_{02} \cdot \lambda_{01}^2 - \Delta\lambda_{01} \cdot \lambda_{02}^2}. \quad (4.17)$$

Assuming  $\Delta\lambda_{01} \approx \Delta\lambda_{02} \approx \Delta\lambda$  this reduces to

$$E_r (\Delta\lambda_{02} \cdot \lambda_{01}^2 - \Delta\lambda_{01} \cdot \lambda_{02}^2) = \frac{2\delta (\lambda_{01}^2 + \lambda_{02}^2)}{\Delta\lambda \cdot (\lambda_{01}^2 - \lambda_{02}^2)} \approx E_r (\Delta\lambda) \frac{(\lambda_{01}^2 + \lambda_{02}^2)}{(\lambda_{01}^2 - \lambda_{02}^2)} \quad (4.18)$$

and the second term of 4.16 becomes:

$$E_r ((2L \cdot \Delta\lambda_{01} \cdot \Delta\lambda_{02})(\lambda_{01} - \lambda_{02})) = E_r (L) + 2E_r (\Delta\lambda). \quad (4.19)$$

The total relative error is then:

$$E_r \left( \frac{\partial N_{eff}(\lambda_0)}{\partial \lambda_0} \right) \approx E_r (\Delta\lambda) \cdot \left[ \frac{(\lambda_{01}^2 + \lambda_{02}^2)}{(\lambda_{01}^2 - \lambda_{02}^2)} + 2 \right] + E_r (L). \quad (4.20)$$

This result evidences the importance of the laser resolution in this kind of measurements. Note that  $N_{eff}$  is polarization dependent, i.e. it differs in quasi-TE and quasi-TM guided modes. It is then necessary to have a tight control on the polarization of the source both to launch only the desired one into the waveguide and to keep it constant during the whole measurement. In fact, if the sample can guide both quasi-TE and quasi-TM modes (for example Titanium indiffused  $LiNbO_3$  waveguides), the presence of both polarizations causes an error on the evaluated  $\Delta\lambda$  and therefore on  $N_{eff}$ . However, this is not a problem if the sample under test is insensitive to the polarization (for example a perfectly circular optical fiber) or if it can

guide only a single polarization (for example a single polarization fiber or a Proton Exchanged  $LiNbO_3$  waveguide) as the lack of polarization stability of the emitted field simply introduces an additional attenuation which depends on the wavelength but does not affect the correctness of the  $\Delta\lambda$  measurement.

It is then important to evidence if the source presents polarization instability. To this purpose, one can simply replace the sample with a polarizer and observe the detected signal. Using our setup we obtained the result reported in figure 4.4. The continuous line is obtained letting the filter pass only the TM polarization, while the dashed one is obtained with a  $90^\circ$  rotation, which allows propagation of the TE polarization. Strong oscillations occur, with phase opposite curves (the TM polarization is fully transmitted when the TE one is completely attenuated) instead of constant values, which should be observed for stable polarization. These oscillations are due to polarization changes related to spectrally dependent physical phenomena occurring in our laser and should not be confused with the Fabry-Perot resonances mentioned before. Note in fact that these plots are obtained with a wavelength scale much larger than that used for attenuation measurements. Here one period corresponds roughly to 3-4 nm, while, in loss measurements (see figure 4.3) periods are about two orders of magnitude smaller. In conclusion with our laser the measurement is still correct if the structure is insensible to the polarization or if guides only a single polarization. If source polarization control is needed, a single polarization input fiber can be used in the setup instead of the polarization maintaining one we used.

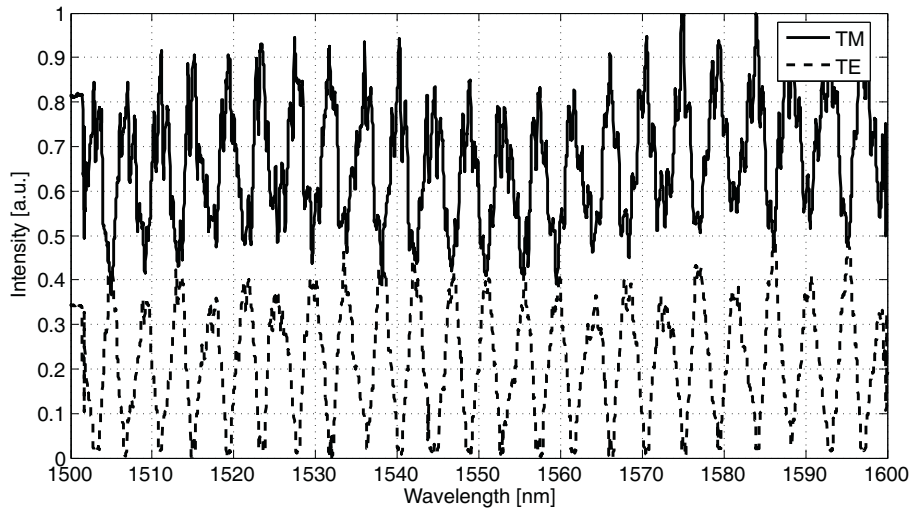


Figure 4.4: Transmitted light intensity through a polarizer oriented to transmit TM (continuous line) and TE (dashed line) polarization versus the wavelength. Polarization roughly varies in the range  $\pm 45^\circ$  around the average value.

### 4.3.3 Mode size measurements

As mentioned before, the near field intensity measurement is made by scanning the output section of the DUT with a SMF28 fiber and detecting the collected light. This kind of measurements provides results which depend not only on the shape of the near field of the DUT but also on that of the scanning fiber. The result of the scanning procedure is then given by:

$$S(x, y) = \left| \int \int \Psi_g(\tau_x, \tau_y) \cdot \Psi_f^*(x - \tau_x, y - \tau_y) d\tau_x d\tau_y \right|^2 \quad (4.21)$$

where  $\Psi_f$  and  $\Psi_g$  are respectively the fiber mode and the mode of the waveguide under test,  $x$  and  $y$  indicating the relative position on the scanning plane. However we are interested in the normalized cross-correlation function  $X(x, y)$  which is expressed as

$$X(x, y) = \frac{\left| \int \int \Psi_g(\tau_x, \tau_y) \cdot \Psi_f^*(x - \tau_x, y - \tau_y) d\tau_x d\tau_y \right|^2}{\int \int |\Psi_g(\tau_x, \tau_y)|^2 d\tau_x d\tau_y \cdot \int \int |\Psi_f(\tau_x, \tau_y)|^2 d\tau_x d\tau_y} \quad (4.22)$$

Its maximum value, corresponding to the best coupling efficiency, added to the Fresnel losses, provides the total coupling loss. To evaluate  $X(x, y)$ ,  $\Psi_f$  and  $\Psi_g$  must then be reconstructed. Assuming a Gaussian profile for the fiber mode  $\Psi_f$  [102], we can obtain its pattern simply scanning another SMF28 fiber:

$$S(x, y) = \left| \int \int \Psi_f(\tau_x, \tau_y) \cdot \Psi_f^*(x - \tau_x, y - \tau_y) d\tau_x d\tau_y \right|^2 = |\Psi_f|^2 \quad (4.23)$$

Once  $\Psi_f$  is known,  $\Psi_g$  can then be extracted from the measured  $S(x, y)$  using a simple decorrelation routine. To obtain correct results with this kind of measurement, source power and wavelength stability should be guaranteed. This may be a problem as the measurement time is long.

A further problem comes from the presence of the air gap between the fiber and the waveguide. Such a gap cannot be eliminated, as it is necessary to allow displacements of the scanning fiber, but forms a parasitic cavity which perturbs the measurement, as seen before when discussing the propagation loss measurements. Moreover, the size of the air gap changes during the scanning procedure, as the scanning plane is never perfectly parallel to the end-face of the sample. This induces a further, varying, perturbation of the transmitted power.

To understand the procedure we envisaged to avoid or at least reduce these problems, let us consider first, for example, an horizontal scanning, done with  $\Theta_v \neq 0$  to avoid the effect of the parasitic cavity. Results depend however also on the value of  $\Theta_h$ . In fact, in 4.21, if  $\Theta_h \neq 0$ , the projection of  $\Psi_f$  on the scanning plane should be considered. This reduces the width of  $S(x, y)$  introducing an error in the measurement, which can be eliminated if  $\Theta_h = 0$ .

This condition can then be found simply performing some scans for varying values of  $\Theta_h$  and looking for the value corresponding to the maximum width of  $S(x, y)$ . As an example we show in figure 4.5 the results of such a measurement using a SMF28 fiber as DUT.

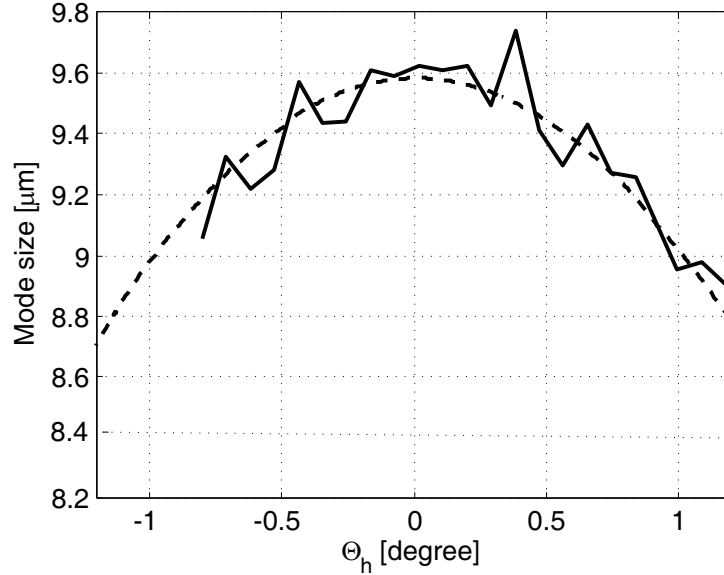


Figure 4.5: Width of the fiber mode measurement versus the angle  $\Theta_h$  (continuous line) and its interpolation with a parabolic function (dashed line). The perfect alignment is obtained for  $\Theta_h = 0$  where the width is maximum.

Reciprocally, for vertical scans,  $\Theta_h \neq 0$  should be assumed and the just described procedure is followed to set  $\Theta_v = 0$ . Figure 4.6 shows results for vertical and horizontal cross-correlation measurements obtained on a SMF28 using our setup. The two fields have the same width, evaluated according to Petermann's definition [103], equal to  $9.6 \pm 0.5 \mu\text{m}$  at  $\lambda = 1.55 \mu\text{m}$ . This value is in agreement with the specification of the fiber manufacturer, which guaranties a mode width of  $10.4 \pm 0.8 \mu\text{m}$  [104], confirming the correctness of the procedure.

The precision of this technique depends on the noise introduced by the decorrelation algorithm and on the accuracy of the positioning system. For what concerns the former cause of noise, it is known that the routine that allows reconstructing the  $\Psi_g$  from cross-correlation measurements consists in a simple iterative algorithm which introduce a noise on the field profile measurement estimated to be around  $\pm 2\%$ . For what concerns the latter problem, piezoelectric stages with open loop power supply without any kind of position control were used in our experimental setup. Without a feedback from the position probes, measurements are affected by the imperfections of the piezoelectric adjusters such as hysteresis and temporal drift which increase systematic error of about  $\pm 0.5 \mu\text{m}$  in the mode size measurements. These errors

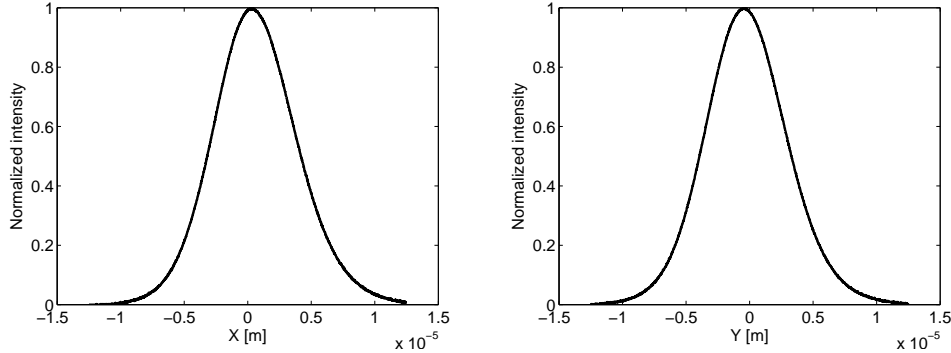


Figure 4.6: Horizontal (left) and vertical (right) cross-correlation measurements of a SMF28 sample.

can be reduced by characterizing the piezoelectric stages and then introducing the proper corrections after the measurement. This has been done for example for data reported in figure 4.5 where the r.m.s. noise induced error was estimated to be lower than  $\pm 0.1 \mu m$ .

Using a setup with feedback from position probes the systematic error of the measurement can be reduced to the value due to the decorrelation noise, which for a mode size measurement is equivalent to  $\pm 0.02 \mu m$ . Compared with other near field reconstruction techniques this solution can reach higher precisions with the only drawback that the measurement is not obtained in real time but can take a few minutes for the scan procedure.

## 4.4 Results

In this section, results of different measurements performed with the setup described so far are illustrated and commented to show both its possibilities and versatility. The test for the propagation loss measurement has been made on integrated optical waveguides fabricated in  $LiNbO_3$  with the soft proton exchange technique (SPE). Figure 4.7 shows the output intensity versus wavelength. The measured contrast is 0.146 which corresponds to total losses of  $2.4 \text{ dB}$ . The sample is  $2.169 \pm 0.0005 \text{ cm}$  long and the propagation losses are then  $1.1 \pm 0.1 \text{ dB/cm}$ , which corresponds to the expected value for this technology. The accuracy was obtained repeating the measurement and observing the dispersion of the results. Note that the error depending on the evaluation of the angle formed by the waveguide with the end-faces of the sample turns out to be approximately  $5e - 4 \text{ dB}$ , confirming its negligible importance.

In order to validate the  $N_{eff}$  measurement with our experimental setup, we have used a piece of standard fiber (SMF28)  $25.91 \pm 0.025 \text{ mm}$  long. In order to eliminate the cladding modes we have immersed the sample in a proper index matching liquid.

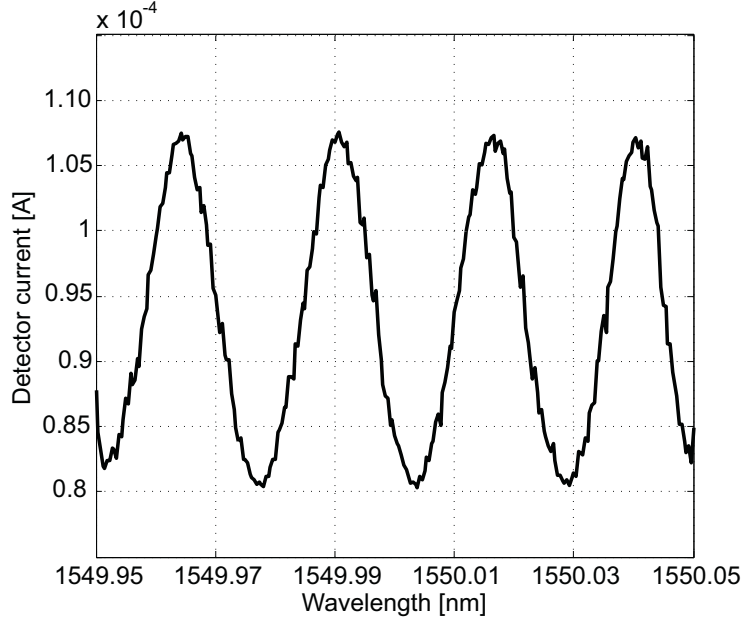


Figure 4.7: Interference fringes of a integrated optical waveguide which forms a Fabry-Perot cavity with its end-faces. The contrast of this oscillation is related to the propagation losses.

The measurement has been obtained by varying the wavelength of the laser between  $\lambda_{min} = 1552 \text{ nm}$  and  $\lambda_{max} = 1554 \text{ nm}$  with step equal to the wavelength resolution  $\delta = 0.001 \text{ nm}$  obtaining a  $\Delta\lambda = 31.54 \pm 0.015 \text{ pm}$  which corresponds to  $N_{eff} = 1.4698$ . The relative error 4.11 of this measurements is  $E_r(N_{eff}) = 2.9e-3$  and is obtained by adding the contributions of both  $E_r(L) = 1.9e-3$  and  $E_r(\Delta\lambda) = 1e-3$ .  $E_r(\lambda_0)$  is in fact negligible with our laser. The fiber data sheet reports  $N_{eff} = 1.4682$  confirming the result obtained with our measurement.

Another example of  $N_{eff}$  measurement has been made for segmented waveguides fabricated on a  $LiNbO_3$  substrate with the SPE technique [66]. Such waveguides present a periodic variation of the refractive index in the propagation direction. As said in the first chapter, one of the most important parameters of these waveguides is the duty cycle  $DC$ , defined as the ratio between the length of the high index segment and the period. Reducing the  $DC$  the  $N_{eff}$  must be reduced too. This properties has been experimentally confirmed and the results reported in figure 4.8 at  $\lambda = 1.55 \mu\text{m}$ .

An example of dispersion slope measurement has been made for the same integrated optical waveguide used for the propagation losses test. Figure 4.9 shows the  $N_{eff}$  measurement obtained at the three wavelengths 1.5, 1.55 and 1.6  $\mu\text{m}$ . The dotted line is the linear interpolation of the results. Measuring the slope of the interpolated curve we obtain a value of  $\partial N_{eff}/\partial\lambda = -0.0225 \pm 0.0025 \mu\text{m}^{-1}$ . The

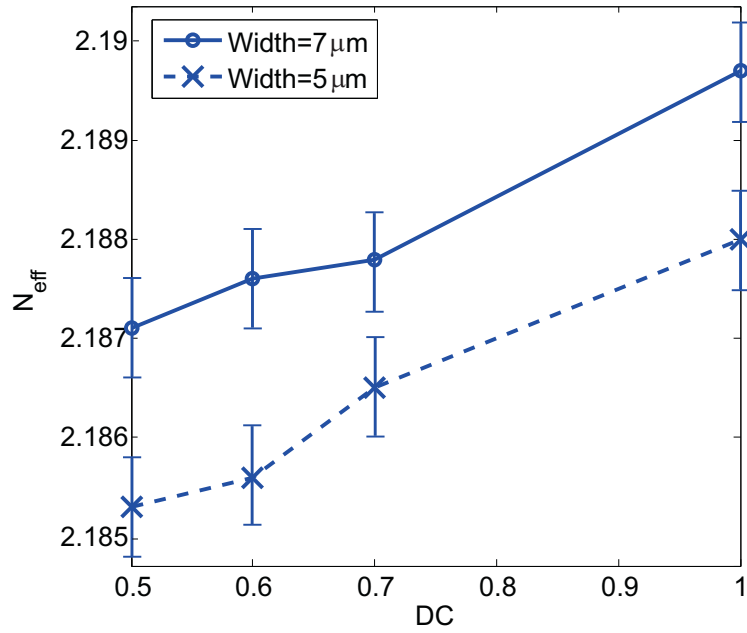


Figure 4.8: Effective group index measurement for segmented waveguide with  $P = 15\mu m$  and  $W = 5\mu m$  (dashed line) and  $7\mu m$  (continuous line).

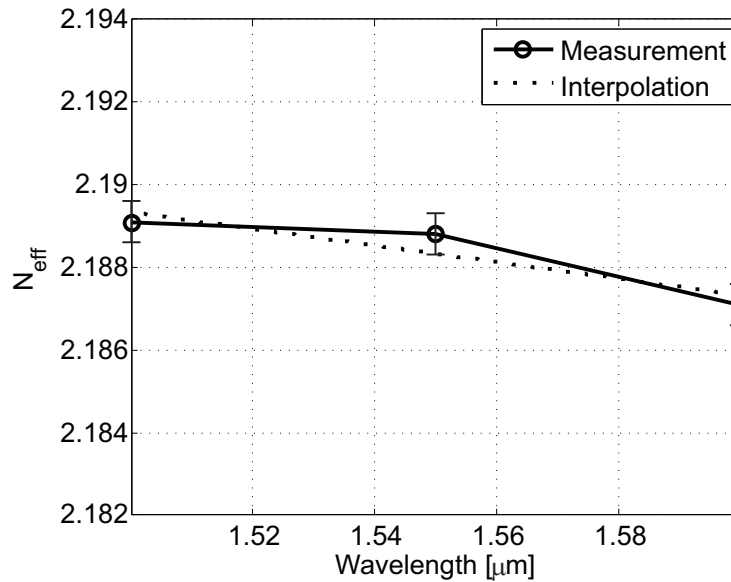


Figure 4.9: Effective group index measurement versus the wavelength. Dotted line represents the linear interpolation to consider for slope evaluation.

chromatic dispersion of an optical device is related to the material and to the guiding dispersion. In our case, simulations has shown that the second term is negligible.

Material dispersion can be easily evaluated with the Sellmeier equation for  $LiNbO_3$ . In particular calculating  $\partial N_{eff}/\partial\lambda$  at  $1.55 \mu m$  we obtain  $-0.0233 \mu m^{-1}$  confirming the measurement.

For the mode field shape measurement and the evaluation of the overlap with an optical fiber we have used as sample the segmented waveguides fabricated on a  $LiNbO_3$  substrate with the SPE technique. Reducing the  $DC$  of the waveguide, one reduces the confinement and the mode size increases. This property can be exploited to reduce the coupling losses between an integrated waveguide and a fiber, as shown in [33]. With our measurements, we have reconstructed the mode in the segmented waveguides for different values of  $DC$  and calculated the overlap with a SMF28 fiber. The reconstructed field is shown in figure 4.10 for a continuous waveguide and is in good agreement with the simulations obtained by modeling the waveguide with a full vectorial 3D BPM [35].

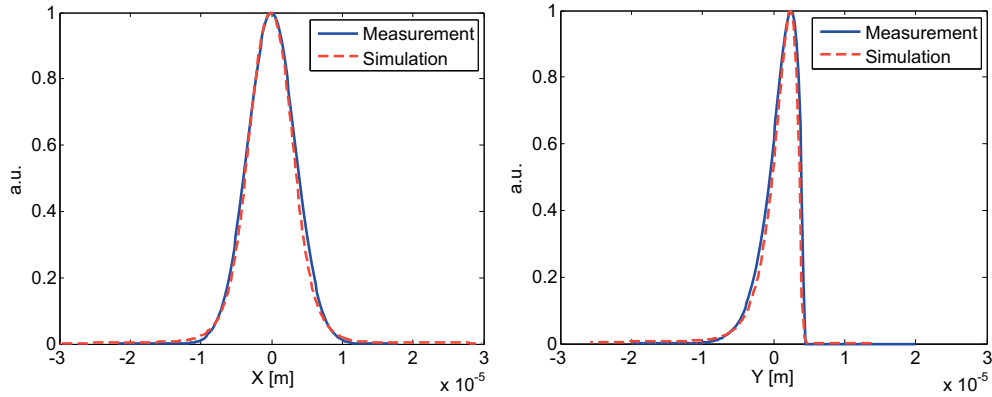


Figure 4.10: Horizontal (left) and vertical (right) mode profile of continuous waveguide.

We have then repeated the measurement for segmented waveguides with different  $DC$  and calculated the overlap integral with the mode fiber obtaining the result of figure 4.11. We can notice that a  $DC$  reduction increases the overlap and induces a coupling losses decrease. In our setup, piezoelectric stage is affected by hysteresis phenomena estimated on the order of 8% of the commanded motion. This uncertainty, added to the contribution of the decorrelation algorithm induces an error on the overlap measurement of less than  $\pm 0.04$ .

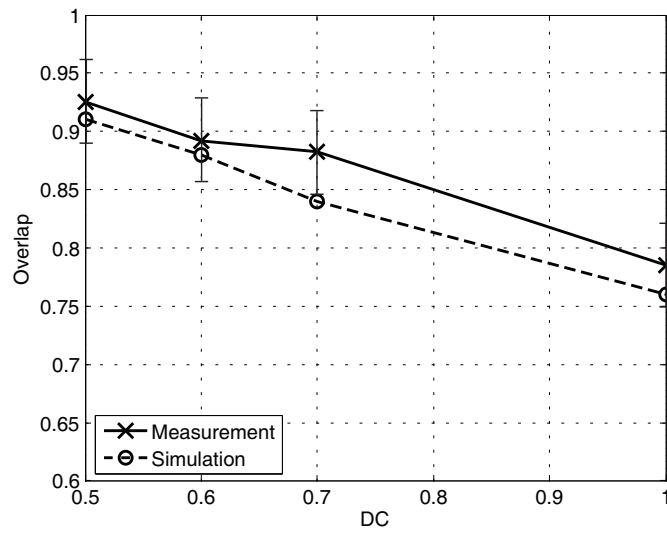


Figure 4.11: Overlap between the segmented waveguide mode and the SMF28 mode for different  $DC$ . Measurements (continuous line) are compared to simulation results (dashed line).



# 5

## Segmented Waveguide Taper

### 5.1 Introduction

As mentioned in the introduction of this thesis, insertion losses have always been a major problem in Integrated Optics. Reducing the insertion losses is important for telecom and sensors applications and is mandatory in the case of Quantum Communication where the information is carried by single photons and where amplifiers are not allowed.

Coupling losses are due to misalignments between the two waveguides, Fresnel reflection and mode mismatch. Misalignments between fiber and IO device can be avoided using careful aligning procedures. Fresnel reflection losses, due to the different values of the refractive indices of the IO waveguide and the optical fiber, can be reduced using index matching fluids or antireflection coatings at the end-face of the sample. Mode mismatch losses are due to different mode sizes in the IO waveguide and the fiber. They are particularly important in the case of active electro-optic (EO) or nonlinear (NL) devices where the component efficiency is a growing function of the mode confinement. In these cases, designing the waveguide to optimize its coupling with low confinement telecom single mode fibers is far from being optimum, but is the more commonly used technique [105] since we are still missing a practical and cost effective solution allowing longitudinal variation of the transversal section of the waveguide mode. This mode size transformer (taper) should be adiabatic, as short as possible, in order to realize the best trade off between propagation losses and coupling efficiency. In the literature a lot of solutions for the design of a taper has been proposed [106, 107, 108]. Among them, the segmented waveguide configuration seems the most suitable as it does not introduce additional steps in the fabrication process [34, 109, 110, 33, 111, 112]. In principle, this technique is rather general, and can be adapted to any material or waveguide fabrication technique. Nevertheless, as the excess losses induced by the segmentation depend very much on material and waveguide fabrication technique, each case has to be carefully studied experimentally. In this chapter, we present a study devoted to waveguides

realized in  $Z$ -cut wafers of  $LiNbO_3$  that are commonly used for their good non-linear properties, allowing for example the fabrication of efficient optical frequency converters and photon pair sources required for quantum communication at telecom wavelength [113]. The reported results [114] show that when pushing the SPE parameters to obtain waveguides with the maximum  $\Delta n$ , which allows maximum field confinement, tapers showing an overall reduction of the insertion losses with respect to the untapered waveguide can be successfully realized. The chapter is organized as follows. In the next section, the numerical taper design are described. Then, the fabrication processes and different characterization techniques used to evaluate the improvements of the taper are illustrated. Finally, the experimental results obtained with different fabrication parameters of the taper are presented.

## 5.2 Numerical design of the taper

The tested devices are constituted by a taper that transforms the highly confined mode of a continuous waveguide (CWG) to that confined by a segmented one (SWG) as shown in figure 5.1. To understand the features of the mode of such a waveguide

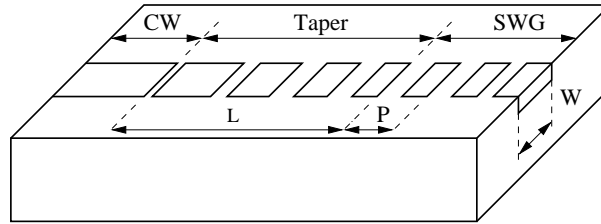


Figure 5.1: Schematic of the tested devices.

one should remind (Chapter 2) that SWG behavior can be described using the so called equivalent waveguide theorem for periodic structures [115, 116, 74]. For wavelengths far away from the band gap, a SWG is equivalent to a continuous waveguide with the same depth and same width but with a surface index equal to:

$$n_{eq} = n_{sub} + \Delta n \cdot DC \quad (5.1)$$

where  $n_{sub}$  is the substrate index and  $DC$  is the duty cycle. In the case of a taper the  $DC$  is varying from  $DC = 1$  (continuous waveguide) to smaller  $DC$  with constant period  $P$  so that the surface index of the equivalent waveguide is reduced as well as the mode confinement. Once the desired mode size is reached, the  $DC$  is kept constant down to the end of the sample to stabilize the mode size after the transformation in the taper.

The numerical modelling of this structure is made with the tools presented in chapter 2. The project of all the taper parameter is obtained following the three steps:

- Numerical modelling of continuous and segmented waveguide in Lithium Niobate fabricated with the SPE techniques using the mode solver and the BPM tools.
- Calculation of the best segmentation parameter ( $DC$ ,  $P$  and  $W$ ) of the SWG in order to maximize the overlap between the SWG mode and the mode of a standard fiber SMF28.
- Evaluation of the taper length  $L$  and  $DC$  variation function during the propagation which allow an adiabatic transformation of the mode.

### 5.2.1 Numerical modelling of Lithium Niobate waveguides

Results presented at the end of chapter 3 show the index profile, evaluated with the IWKB algorithm, for our planar waveguides fabricated with SPE technique in Lithium Niobate substrate. This vertical index profile can be easily fitted with basic functions such as exponential or gaussian and used to describe the index distribution inside our numerical tools. This approach is not completely correct if the m-lines measurement and the IWKB profile reconstruction is made at wavelengths far from those of interest for the numerical analysis. In our case, in fact, the experimental characterization is made at  $632\text{ nm}$ , in order to have multimode structures, while the numerical analysis is made at  $1.55\mu\text{m}$ . Moving from  $\lambda = 632\text{ nm}$  to  $\lambda = 1.55\mu\text{m}$ , in fact, dispersion changes refractive index values. The indices of the substrate and the exchanged zone vary in different ways with respect to wavelength and it is very difficult to obtain the total dispersion behavior for a graded index waveguide. Moreover, the field at  $632\text{ nm}$  is well confined and the interaction with the air interface is very different with respect to the mode at  $1.55\mu\text{m}$ . These kind of considerations are the base of a model proposed by Fabrizio Fogli [117](PhD student of the university of Bologna in collaboration with the LPMC university of Nice - Sophia Antipolis). He proposed a index profile of a SPE waveguide in deep ( $y$  axis) that follows this function:

$$f(y) = e^{-\left(\frac{y}{p}\right)^{0.6}} \quad (5.2)$$

where  $p = 0.615\mu\text{m}$  has been empirically estimated .

For a planar waveguide the index distribution in the horizontal direction is considered constant but for channel waveguide also lateral diffusion in the region protected by the photolithography mask must be evaluated. For a z-cut Lithium Niobate substrate P.Aumont [71] has experimentally and numerically confirmed the

presence of a lateral diffusion modelled by a gaussian function in this way:

$$g(x) = \begin{cases} e^{-\left(\frac{x-\frac{W}{2}}{p}\right)^2}, & x > \frac{W}{2} \\ 1, & \frac{W}{2} \leq x \leq \frac{W}{2} \\ e^{-\left(\frac{x+\frac{W}{2}}{p}\right)^2}, & x < \frac{W}{2} \end{cases} \quad (5.3)$$

where  $t = 1.2 \mu m$  represents the half width at  $1/e$  of the gaussian profile and  $W$  is the waveguide width imposed by the photomask. Combining the vertical and the horizontal profile, we obtain the index distribution for a continuous waveguide:

$$n(x, y) = n_s + \delta n_{\max} \cdot f(y) \cdot g(x) \quad (5.4)$$

where  $n_s$  is the substrate index and  $\delta n_{\max}$  the maximum index variation at the surface. For a well confined waveguide  $\delta n_{\max}$  has been estimated equal to 0.071. This structure can be analyzed with the mode solver. Figure 5.2 shows the intensity of the fundamental mode at  $1.55 \mu m$  for the three components  $E_y$  and  $E_x$  and  $E_z$  ( $E_y$  is the main component).

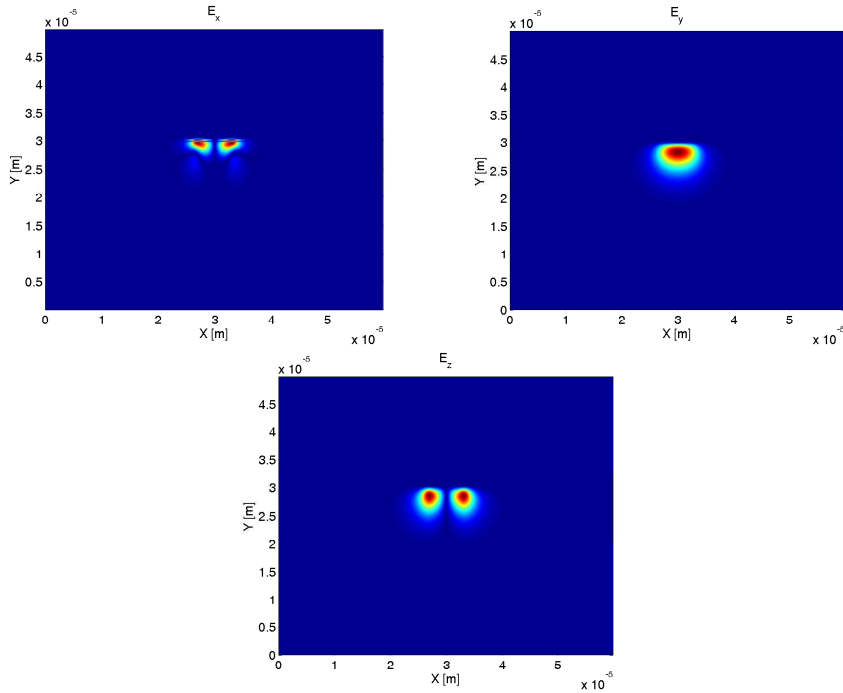


Figure 5.2: Three electric field components of the SPE waveguide calculated with the mode solver.

The computational window is  $60 \mu m \times 50 \mu m$ , large enough to prevent border effects induced by the absence of PML. The mesh discretization has been fixed at

$\Delta x = \Delta y = 0.2 \mu m$  as the best trade off between the accuracy of the results and the computational time has been obtained for that mesh as shown in the next table. This model is in quite good agreement with the m-lines measurement performed at

$\Delta x = \Delta y$	x points	y points	$n_{eff}$	Elapsed time [s]	Precision
0.05	600	800	2.1435705	3360	ref.
0.1	300	400	2.1427007	240	4.06e-4
0.2	150	200	2.1424178	35	5.38e-4
0.4	75	100	2.1422174	5	6.32e-4
0.5	60	80	2.1419813	2	7.42e-4

$1.55 \mu m$  with just one mode is in propagation. Once the mode guided by the straight waveguide has been calculated, it is possible to model the segmented waveguide behavior. The Beam Propagation Method is the best numerical tool to analyze this kind of longitudinal varying structure. The fundamental assumptions to obtain correct BPM solutions are satisfied for *SPE* : *LiNbO<sub>3</sub>* waveguides, in fact, the index variation is weak and the field intensity can not change very fast during the propagation on distance compared to the wavelength. Moreover, the low contrast longitudinal changes do not allow the excitation of back propagating modes.

In view of realistic simulations of these waveguides, the refractive index modelling include both the effects of lateral and longitudinal proton diffusion. As we use *Z*-cut Lithium Niobate crystal substrate, we can say that lateral and longitudinal diffusion are identical and induce the same index profile. The profile can than be written in *z* direction as:

$$h(z) = \begin{cases} e^{-\left(\frac{z}{t}\right)^2}, & z < z_i \\ e^{-\left(\frac{z-z_i}{t}\right)^2}, & z_i \leq z < 2z_i \\ 1, & P(1 - DC_m) \leq z < P \end{cases} \quad (5.5)$$

where  $z_i$  is the the point corresponding to the mid masked zone. Moreover  $DC_m$  is the mask duty cycle defined as the ratio between the length of the mask segment and the period. Adopting the longitudinal index profile of equation 5.5 Pierre Aumont [71] in his PhD work calculated the transmission in the SPE segmented waveguides, concluding that the reflections in the Bragg region are extremely weak for periods larger than  $8\mu m$ , due to the strong lateral diffusion of the fabrication process. Note that, if the segments were square like shape, then the high order contribution of the refractive index grating formed by the segments could be efficient. But because of the strong lateral diffusion, the segments are not at all square like shape but much more smooth, so the high orders are extremely unefficient. For example, in a waveguide with length equal to  $2.5cm$ ,  $P = 8\mu m$ , the nearest Bragg peak at wavelength  $1.55\mu m$  reduces the transmission from 1 to 0.9997 which is not a detectable

variation. With the same structure, the length of the waveguide should be  $14\text{cm}$  in order to obtain a 1% attenuation. In our PSW the periods are always larger than  $8\mu\text{m}$  and the reflectivity can only be smaller. For this reason we have no limitation on the device operating bandwidth and we could use the BPM to study this kind of structure.

In case of intersection between two neighboring gaussian profiles, each profile is considered independently as depicted in figure 5.3. This choice has been made by Pierre Aumont comparing the effective index measurements obtained with simulations at different index profiles and different  $DC_m$ . An important consequence derived by

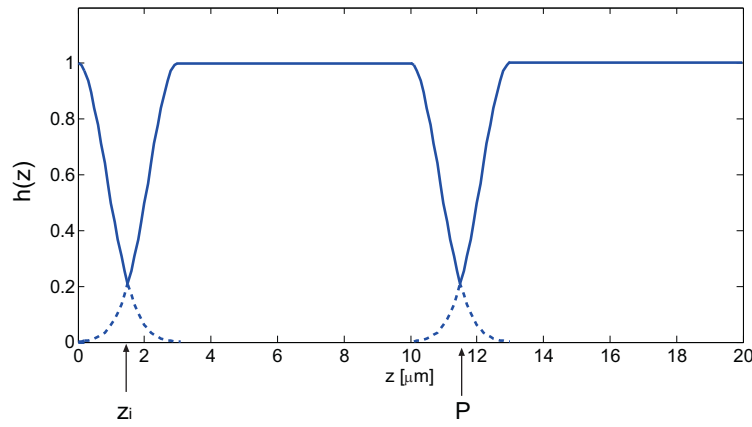


Figure 5.3: Longitudinal refractive index profile for a SPE segmented waveguide with period  $P = 10 \mu\text{m}$  and  $DC_m = 0.7$ .

the presence of a longitudinal diffusion is that the  $DC$  must be redefined as:

$$DC = \frac{\int_0^P h(z) dz}{\int_0^P 1 dz} \quad (5.6)$$

which, after some algebra, becomes:

$$DC = DC_m + \sqrt{\pi} \frac{t}{P} \text{erf} \left[ \frac{P(1 - DC_m)}{2t} \right] \quad (5.7)$$

which can be useful when using the equivalent waveguide theorem. When we introduce this segmented waveguide model in the 3D BPM we can use the same mesh used in the mode solver. Concerning the longitudinal step, we have fixed  $\Delta z = 0.2 \mu\text{m}$ . This value has been chosen as before as the best compromise between precision and CPU time which is proportional, for a fixed propagation length, to the inverse of  $\Delta z$ . The following table shows the computational times for different values of  $\Delta z$

and the corresponding precisions obtained for the power evolution in a  $2\text{mm}$  length segmented waveguide with  $P = 15\mu\text{m}$ ,  $W = 5\mu\text{m}$  and  $DC_m = 0.5$ . I consider the result obtained for  $\Delta z = 0.1\mu\text{m}$  as a reference (Ref. in the table) for the precision evaluation.

$\Delta z[\mu\text{m}]$	Elapsed time [s]	Precision
0.1	14520	Ref.
0.2	7260	$5.68\text{e-}5$
0.4	4020	$2.84\text{e-}4$
0.5	3360	$4.26\text{e-}4$
1.0	2340	$1.82\text{e-}3$

### 5.2.2 Segmented waveguide design

The SWG positioned at the end of the sample determines the dimensions of the output mode. Modifying its parameters ( $DC$ ,  $P$  and  $W$ ) we can then improve the coupling efficiency to the fiber mode.

The parameter we need to maximize is the overlap integral between the output field of the SWG  $\psi_{SWG}$  and the fiber mode  $\psi_f$ , defined as:

$$I = \frac{|\iint \Psi_{SWG} \cdot \Psi_f^* dS|^2}{\iint |\Psi_{SWG}|^2 dS \cdot \iint |\Psi_f|^2 dS}. \quad (5.8)$$

The fiber mode  $\psi_f$  can be easily obtained using the mode solver because the structure is  $z$ -invariant. Considering a standard SMF28 single mode fiber [?] the result is shown in figure 5.4.

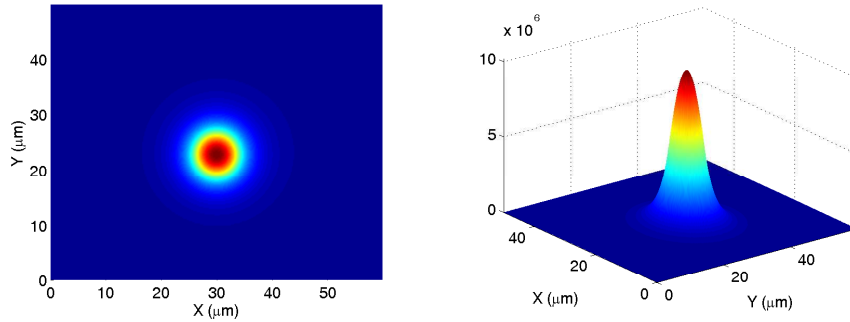


Figure 5.4: Calculated fundamental mode intensity in a standard SMF28.

In order to obtain a good precision when determining the propagating field in the segmented waveguide, instead of the mode solver, we have used the 3D BPM. The transversal model of the integrated waveguide is the same of the previous model

analyzed in section 5.2.1 for the *SPE* :  $LiNbO_3$  waveguides. The transversal computational window is less critical because the BPM uses PML layers.

For the simulations, we have considered segmented waveguides with periods  $P = 15 \mu m$  and  $P = 25 \mu m$ . Figure 5.5 shows the overlap integral  $I$  between the fundamental mode of the SMF28 and the mode of the segmented waveguide as a function of the  $DC_m$  for period  $P = 15 \mu m$  and  $P = 25 \mu m$ .

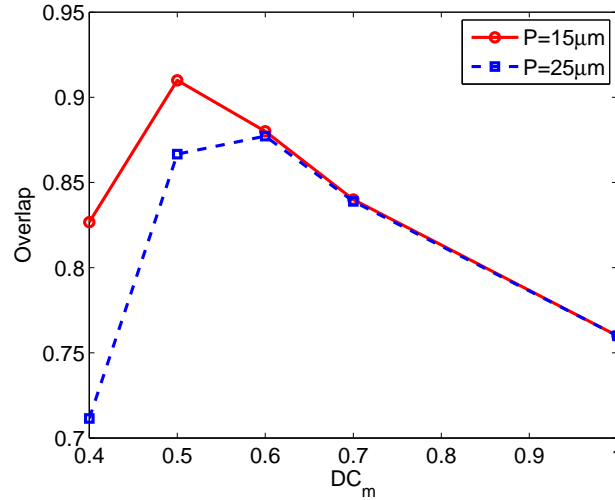


Figure 5.5: Overlap integral  $I$  between the fundamental mode of the SMF28 and the mode of the segmented waveguide as a function of the  $DC_m$  for  $P = 15 \mu m$  and  $P = 25 \mu m$ .

For a continuous waveguide ( $DC = 1$ ) the calculated overlap is 0.76. Reducing the  $DC$  this overlap increases as a better match between the segmented waveguide mode and the fiber mode. Reducing the period  $P$ , the maximum overlap is obtained in correspondence of a smaller  $DC_m$ . This behavior is explained by the presence of the longitudinal diffusion. In fact plotting  $DC$  versus  $DC_m$  for  $P = 15 \mu m$  and  $P = 25 \mu m$  (left part of figure 5.5) we obtain two shifted curves which can be used to express the overlap as a function of  $DC$  (right part of figure 5.5). With this consideration, the maximum for the two curves is obtained for the same value of  $DC = 0.64$ .

As said before, the coupling losses, are related to the overlap between the two modes  $\psi_g$  and  $\psi_f$ , but also to the effect of the Fresnel reflections at the interface. When we couple an optical fiber with an integrated waveguide an air gap is formed. Neglecting the multiple reflections in the air gap, the attenuation induced by the passage of the electromagnetic field through these three different materials can be evaluated using the following relation [38]:

$$T_f = \frac{4n_1n_2}{(n_1 + n_2)^2} \cdot \frac{4n_2n_3}{(n_2 + n_3)^2} \quad (5.9)$$

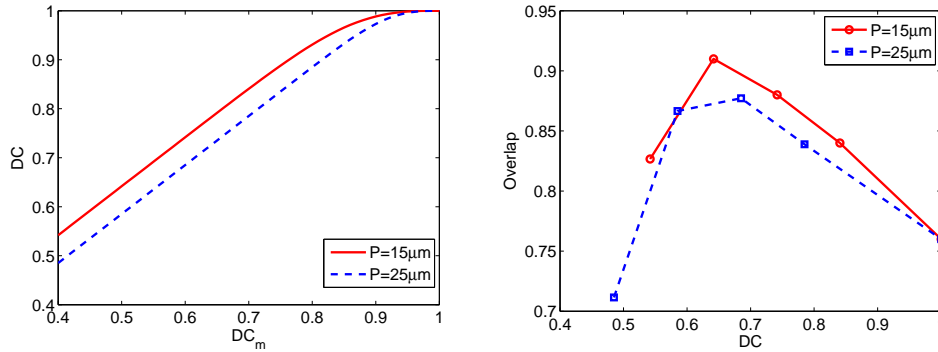


Figure 5.6: In the left part: relation between the  $DC$  and the  $DC_m$  for  $P = 15 \mu\text{m}$  and  $P = 25 \mu\text{m}$ . In the right part: Overlap integral  $I$  between the fundamental mode of the SMF28 and the mode of the segmented waveguide as a function of the  $DC$ .

where  $n_1$  is the effective index of the propagating mode in the segmented waveguide,  $n_2$  is air (or the index of added liquid) and  $n_3$  is the fiber effective index. The values of  $n_1$  versus the  $DC_m$  can be obtained using the BPM, the result is shown in figure 5.7. Considering  $n_2 = 1$  the values of  $T_f$  as a function of  $DC_m$  is shown in figure 5.8.

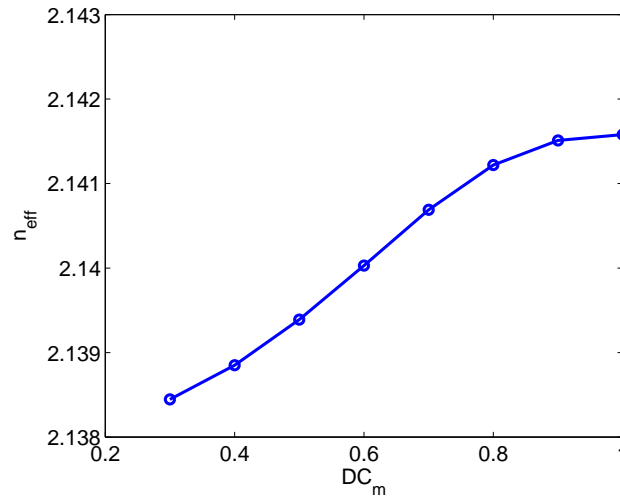


Figure 5.7: Evaluation of the effective index in the segmented waveguide as a function of  $DC_m$ .

Note that reducing  $DC_m$  the Fresnel reflections are reduced too, but this variation is relatively small and does not modify the optimal values of  $DC_m$  obtained considering the overlap integral.

It is now necessary to consider how the width of the waveguide  $W$  can modify

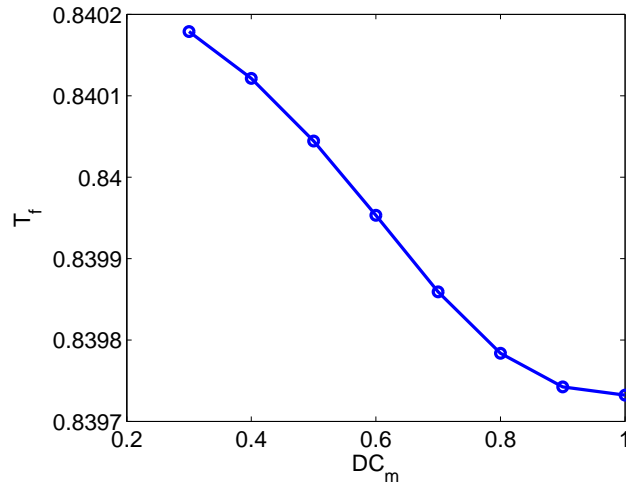


Figure 5.8: Fresnel transmission coefficient versus  $DC_m$  considering a segmented waveguide coupled to a fiber optic trough an air gap.

the overlap with the fiber mode. To do that, we have considered the parameters which provide the best performance  $DC_m = 0.5$  and  $P = 15 \mu m$  and we have evaluated the overlap integral  $I$  varying  $W$ . Figure 5.9 shows the obtained results. For  $W < 3.5 \mu m$  the waveguide mode approaches the cutoff condition and for  $W >$

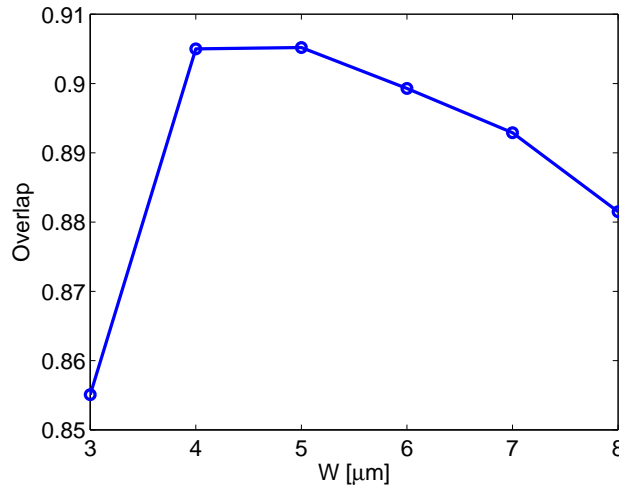


Figure 5.9: Overlap integral versus the waveguide width ( $W$ ).

$8 \mu m$  the mode presents a strong ellipticity and the waveguide becomes multimode. For  $3.5 < W < 8 \mu m$  the overlap variation is not very large and the maximum is obtained for  $W = 5 \mu m$ .

Another important parameter, we would like to calculate with the BPM analysis,

is the propagation loss. This evaluation can be easily done calculating the total power of the computational window during the propagation and fit the result with an exponential. Such kind of evaluation has been made for the segmented waveguides with period  $P = 15 \mu\text{m}$ ,  $W = 5 \mu\text{m}$  for different  $DC_m$ . The obtained results has then been compared to the measured propagation losses presented in chapter 3. From figure 5.10 we note disagreement between the two results. This happen

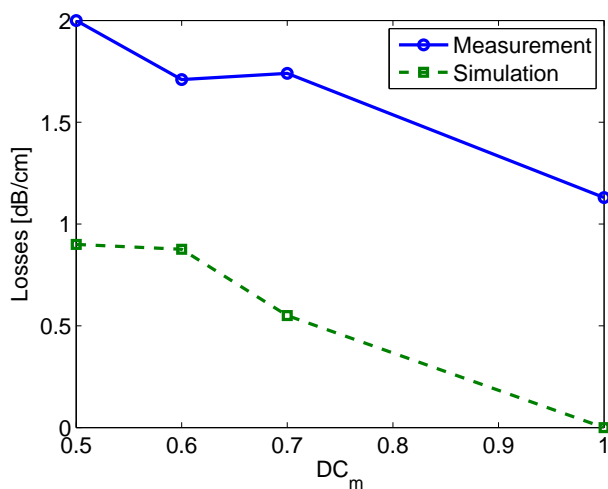


Figure 5.10: Comparison between calculated and measured propagation losses as a function of  $DC_m$  for segmented waveguides with period  $P = 15 \mu\text{m}$  and  $W = 5 \mu\text{m}$ .

because we can not consider in the BPM model the roughness at the surface of the real component. A proposed solution is to introduce complex dielectric constant in the BPM and assign an absorption profile to the waveguide. The problem is to determine the right complex profile for which the scattering losses are equal to the artificial absorption losses.

The concluding of this discussion on segmented waveguides design, we have found that the best coupling with a SMF28 can be obtained for  $P = 15 \mu\text{m}$ ,  $DC_m = 0.5$  and  $W = 5 \mu\text{m}$ .

### 5.2.3 Taper design

In this section we will now address the problem of designing a tapered SWG. The aim of the taper is to transform (see figure 5.11) the fundamental mode of a continuous waveguide into the fundamental mode of the segmented waveguide that provides the best coupling with the mode fiber. As expressed by the equivalent waveguide theorem, the  $DC$  is the parameter we have to change in order to modify the segmented waveguide properties. This parameter can be modified playing with  $DC_m$  and  $P$ . With the design of the final PSW (positioned at the interface with the

fiber), we have fixed the parameters  $W$ ,  $DC_m$  and  $P$  at the end of the taper. The optimal  $W$  of the PSW is equal to  $5\mu m$ , which is a good value also for a continuous waveguide. For this reason we do not need to modify its value in the taper. In the case of continuous waveguide which requires different values of  $W$  a variation of the taper width should be introduced. For the mode shaping we can play with both  $DC_m$  and  $P$ . If we choose to modify  $P$  we have two possible choices:

1. Move from a continuous waveguide to a PSW with  $DC_m$  constant;
2. Move from a continuous waveguide to a PSW modifying both  $DC_m$  and  $P$ .

Solution 1 has the problem that for  $DC$  near to 1,  $P$  must reach higher values and this causes the increase of the total taper length (and of losses accordingly). Solution 2 has not the problem of solution 1 but the taper design results rather complicated as both  $DC_m$  and  $P$  must change in order to obtain a slow variation of the real  $DC$ . In conclusion, the best taper design is obtained modifying the  $DC_m$  with a constant period  $P$ .

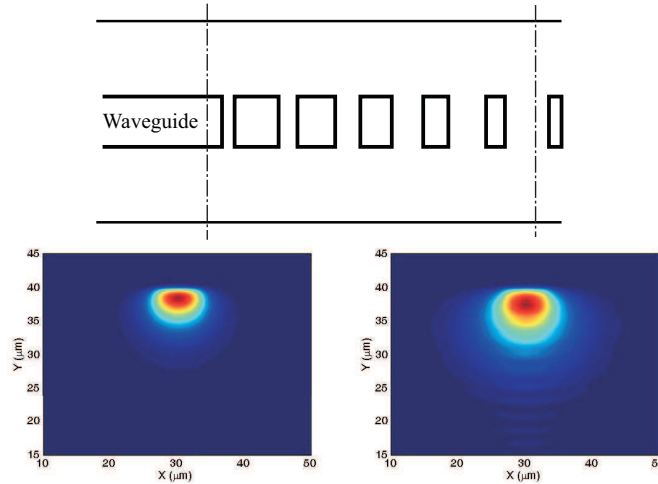


Figure 5.11: Schematic representation of the taper structure for the mode transformation.

The 3D BPM has been used also for the taper analysis. The goal of the taper is to perform such mode transformation minimizing losses and device length. Taper losses are due to two contributions. The former is related to the fact that the structure is  $z$ -variant and during mode transformation some radiating modes can be excited thus increasing the propagation losses. This problem, in our case, is increased by fabrication imperfection and for this reason it is very difficult to quantify their values. The latter contribution is related to the mismatch between the mode at the output of the taper and the mode of the segmented waveguide, as it happens in a general coupling problem.

The parameters to determine for a complete definition of the taper structure are the length  $L$  and the  $DC_m$  variation function in the longitudinal axes. We have considered two  $DC_m$  variation functions: the linear and the cubic ( $DC_m^{lin}$  and  $DC_m^{cub}$ ) defined by:

$$\begin{aligned} DC_m^{lin}(z) &= 1 - \left( \frac{1 - DC_m}{L} \right) z \\ DC_m^{cub}(z) &= 1 - \left( \frac{1 - DC_m}{L^3} \right) z^3. \end{aligned} \quad (5.10)$$

In order to determine which of them provide the better performances, we have calculated the overlap between the field at the output of the taper and the mode of the segmented waveguide as a function of the taper length  $L$ . Figure 5.12 shows

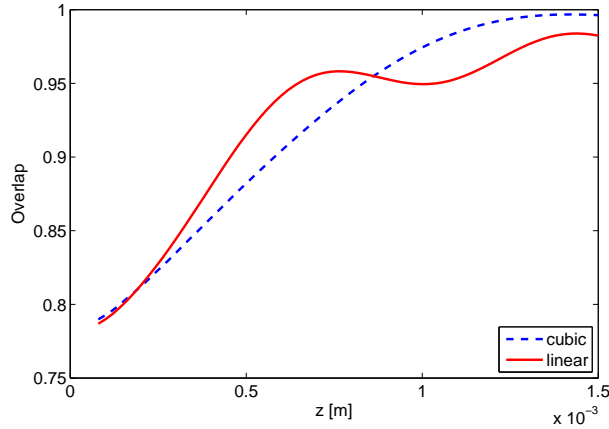


Figure 5.12: Overlap between the field at the output of the taper and the mode of the segmented waveguide as a function of the taper length  $L$  for a linear (red line) and cubic (blue dashed line) variation of the  $DC_m$ .

that the cubic taper can provide a practically perfect overlap at  $L = 1400 \mu m$  while the linear one requires longer taper lengths. This result confirms results previously published in literature [34]. The need to reduce taper length comes not only from the need of compactness, but also from the larger propagation losses induced by longer devices. This is then a trade off which must be determined: propagation losses, can be reduced with a taper length reduction, while the overlap with the segmented waveguide mode is improved increasing the taper length. Such a trade off cannot be determined using the BPM because, as said before, surface imperfections cannot be included in the numerical model. Figure 5.13 provides anyway a good hint. Propagation losses in fact can only reduce the value of the optimal  $L$ . To better explain this point we have considered a taper with constant propagation losses equal

to  $2.5 \text{ dB/cm}$ . Figure 5.13 shows the propagation and the overlap losses and their combination to obtain the total losses as a function of the length  $L$ . Note that the

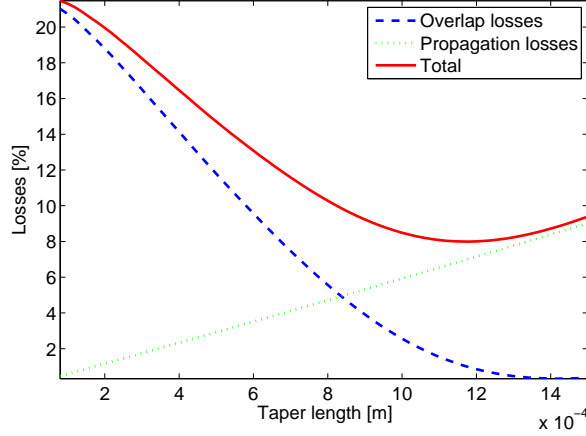


Figure 5.13: Propagation (green dotted line) and overlap losses (blue dashed line) as a function of the taper length  $L$ . The red line represents the total of the two contributes.

length of the total losses minimum (red line) is no longer  $1400 \mu\text{m}$  but reduced to  $1190 \mu\text{m}$  once the propagating losses term is considered. In conclusion the numerical analysis of the taper shows that changing the  $DC_m$  from  $DC_m = 1$  to  $DC_m = 0.5$  with a segmentation period  $P = 15 \mu\text{m}$ , the better solution is to use a cubic  $DC_m$  longitudinal variation function and a length between  $1000$  and  $1400 \mu\text{m}$ , depending on the propagating losses. The overlap with the SMF28 pass from  $76\%$  to  $92\%$  ( $0.82 \text{ dB}$ ) and from this improvement we must subtract the loss introduced by the taper and the segmented waveguide respect the continuous waveguide. The worst case of taper losses equal to  $2.5 \text{ dB/cm}$  induce a reduction of  $0.36 \text{ dB}$  but more reasonably we can imagine a reduction between  $0.1 \text{ dB}$  and  $0.2 \text{ dB}$ , which allow an insertion losses overall reduction between  $0.62 \text{ dB}$  and  $0.72 \text{ dB}$ .

To conclude the numerical analysis we can study the wavelength dependence of the optimum design for improved coupling with SMF28. Modifying the working wavelength, at the output of the taper, the mode shape changes in a different way respect to the fiber mode. This means that, in order optimize the taper design for different wavelengths, its parameters must be recalculated. We have done some simulations for  $\lambda = 1.31 \mu\text{m}$  instead of  $1.55 \mu\text{m}$ . With such a wavelength reduction, at the output of the taper, the mode size is strongly reduced with respect to the fiber. The next table shows the overlap as a function of the  $DC_m$  for period  $P = 15 \mu\text{m}$  and  $W = 5 \mu\text{m}$  at  $\lambda = 1.31 \mu\text{m}$ .

Note that the maximum value of the overlap is now obtained for  $DC_m = 0.4$  and its value is smaller with respect the overlap of  $0.92$  calculated at  $\lambda = 1.55 \mu\text{m}$  and  $DC_m$  equal to  $0.5$ . It is possible to conclude that with a wavelength reduction, the

$DC_m$	Overlap
0.3	0.8756
0.4	0.8950
0.5	0.8366

optimum design can be obtained reducing the final  $DC_m$  of the segmented waveguide taper and similarly with a wavelength increase the optimum design can be obtained for higher  $DC_m$ . Concerning the taper length no important variations have been observed in this wavelength range.

### 5.3 Device Fabrication

Samples are fabricated on a *Z*-cut  $LiNbO_3$  substrate with the SPE and photolithography techniques described in chapter 3. The SPE has been used with two different values of LB percentage. A first sample has been fabricated with 3.5% of LB, which gives a small index variation and a second one with 2.8% of LB to create SPE guides with the maximum index variation. In both cases waveguides are monomode at  $1.55 \mu m$ , the standard telecommunication wavelength and therefore the preferred wavelength for long distance quantum communications. As said before, the parameters we can choose when designing the taper are its length ( $L$ ), the segmentation period ( $P$ ), the final duty cycle ( $DC_m$ ) and the waveguide width ( $W$ ). Tapers with 48 possible combinations of these parameters were then fabricated on the same substrate. The following table summarizes the values of the parameters used for the tapers present on the sample.

$P[\mu m]$	$DC_m$	$W[\mu m]$	$L[\mu m]$
15	0.5	5	100
25	0.6	7	600
	0.7		1000
			1400

The last fabrication step is the end-face polishing to allow end-fire coupling of the sample with the input and output fiber. A particular care is devoted to the control of the angle between the end-face and the waveguides which has to be  $90^\circ$  in order to use the Fabry-Perot technique to measure propagation loss [83].

### 5.4 Experimental setup

In this section, we describe the device characterizations of the fabricated samples using the experimental setup described in chapter 4. This system can be used not only to evaluate separately the integrated optical waveguide propagation losses and

the mode overlap integral but also their combined effect, comparing the overall coupling efficiencies using tapered and untapered structures. The three characterization steps can be summarized as follows:

- The propagation losses are measured using the Fabry-Perot cavity technique [83]. Measuring the power transmitted through the system at different wavelengths, one obtains fringes whose contrast is directly related to the propagation losses.
- The overlap integral between waveguide and fiber modes can be evaluated via the measurement of the mode cross-correlation. Such a function is measured by exciting the waveguide under test with a constant power at a fixed wavelength and recording the power collected by the output fiber, while it scans, with 16 nm steps, a  $25 \mu\text{m} \times 25 \mu\text{m}$  window centered on the waveguide output. Such measurement is similar to that described in [99] and provides many information. First of all we can quantify how critical the fiber to waveguide alignment is. A sharp cross-correlation function corresponds to a low tolerance to alignment errors, while a smooth cross correlation function allows some alignment errors without dramatic impact on the coupling losses. Moreover, knowing the cross-correlation function and the fundamental mode pattern  $\psi_f$  of the SFM28 fiber, it is possible to reconstruct the waveguide mode field distribution  $\psi_w$  through a simple deconvolution operation. This finally allows evaluating the intensity overlap integral 5.8. Evaluating this integral for different tapers allows then to determine the combination of parameters which gives the better mode matching.
- The overall coupling efficiency improvement, which depends on the combined effect of taper induced propagation losses and waveguide to fiber mode matching improvement can be evaluated comparing the maximum power transmitted through the different waveguides present on the sample under test. For each waveguide, the throughput power is measured optimizing contemporarily the positions of both input and output fibers with piezo-controlled stages.

## 5.5 Results

We have first characterized the sample obtained with 3.5% of LB. Figure 5.14(a) presents the mode size as a function of the  $DC_m$  of the segmented waveguides. For  $DC_m = 1$ , corresponding to a continuous waveguide, we found mode sizes bigger than the fiber mode size (dashed line). This indicates that the field is less confined in the waveguide than in the fiber. In this case we found an overlap of 85%, which cannot be improved by the use of a taper. The losses measured for the continuous waveguide are  $1.5 \text{ dB/cm}$ . They are mainly caused by surface scattering. The weak

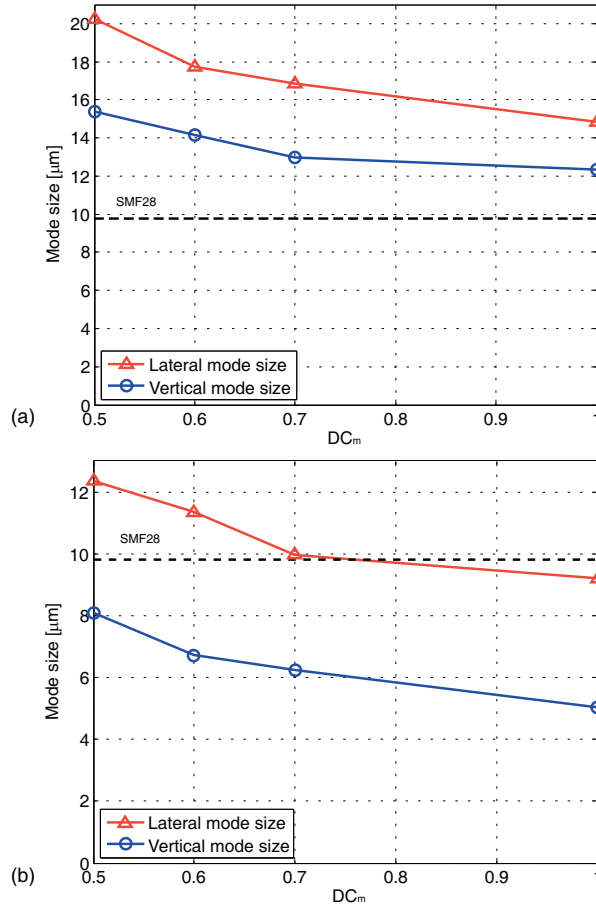


Figure 5.14: Measurement of the lateral and vertical mode sizes (at  $1/e$  of the field maximum) of segmented waveguides as a function of  $DC_m$  with  $W = 5\mu m$  and  $P = 15\mu m$  for two samples fabricated with 3.5% (a) and 2.8% (b) of LB. The dotted line refers to the mode size of the output fiber SMF28.

confinement of the mode allows a strong interaction with surface imperfections and is responsible for these rather high scattering losses. In this case high performances cannot reasonably be obtained for non-linear or electro-optical components. In fact, even if coupling losses are small, the weak mode confinement does not allow strong localized field intensity.

The second sample was fabricated performing SPE with 2.8% of LB, condition which corresponds to the maximum index increase achievable with this technique. In this case a stronger confinement is expected. This is confirmed by the results shown in Figure 5.14(b), where the mode size of the segmented waveguide is reported as a function of the  $DC_m$ . The field is more confined and this contributes to reduce the losses down to  $1\text{ dB/cm}$ . As said before, the drawback of a smaller mode size is the increase of the coupling losses related to the reduction of the mode-fiber

overlap. Figure 5.15 shows that for  $DC_m = 1$  the overlap is 78% but the use of a segmented waveguide taper can improve it up to 92% for  $DC_m = 0.5$ ,  $W = 5 \mu m$  and a period  $P = 15 \mu m$  (continuous line). This corresponds to an improvement of  $0.71 \text{ dB}$  in logarithmic scale. This experimental result agrees with the numerical prediction obtained using a 3D BPM [35] (dashed line in figure 5.15). However, this result is not the real performance improvement, which can be obtained using tapered and segmented waveguides, as they induce extra propagation losses which are not taken into account in the overlap integral. These extra propagation losses are due to imperfect mode transformation and scattering losses at the segments edges. So, the use of a segmented waveguide taper becomes effective if the mode matching improvement is larger than the propagation loss increase. Using the Fabry-Perot cavity technique, illustrated in the previous section, taper and segmented waveguide introduction was found to cause a loss increase of only  $0.04 \text{ dB}$  with respect to the continuous waveguide. The total improvement obtained in terms of waveguide to fiber coupling is then  $0.71 - 0.04 = 0.67 \text{ dB}$ . The precision of this result is estimated to be around  $\pm 0.2 \text{ dB}$ . The overall improvement was also measured using the approach described in chapter 4. The results are reported in the following table where  $P_t$  and  $P_{CWG}$  are output powers measured at the end of the waveguides with and without taper respectively. Negative results correspond to the cases where the overlap improvement does not even compensate for the additional losses. The optimum length of the taper depends on the segmentation parameters and the table reports the results for the lengths that provide the best performances. We obtained the overall best result with a  $1400 \mu m$  long taper associated to a  $2600 \mu m$  long segmented waveguide, with  $P = 15 \mu m$ ,  $W = 5 \mu m$  and  $DC_m = 0.5$ . In that case, an overall increase of  $0.78 \text{ dB}$  of the transmitted power was observed with respect to the continuous waveguide. The precision of this measurement is around  $\pm 0.1 \text{ dB}$ . These two different measurements give results, which taking into account the uncertainties, are equal and confirm the practical interest of segmented waveguide tapers realized using the SPE process. It is worth noting that the test structures realized for this study have taper at one end only. Therefore, the benefit for a real component with a taper at both ends will be doubled. Further improvement can also be obtained working on the taper length, which can be reduced by reducing the segmentation period.

$P[\mu m]$	Taper length $L[\mu m]$	$DC_m$	$10 \log(P_t/P_{CWG})$ $[W = 5 \mu m]$	$10 \log(P_t/P_{CWG})$ $[W = 7 \mu m]$
15	1400	0.5	0.78 dB	0.06 dB
	1000	0.6	0.22 dB	-0.25 dB
	600	0.7	0.19 dB	0.20 dB
25	1400	0.5	-0.53 dB	0.37 dB
	1400	0.6	0.15 dB	0.43 dB
	600	0.7	0.51 dB	0.47 dB

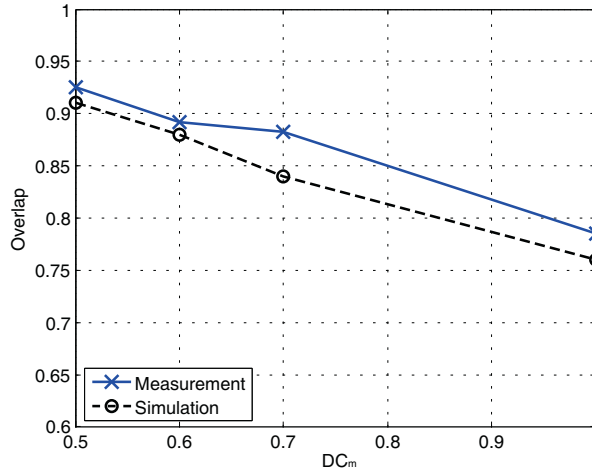


Figure 5.15: Overlap between the segmented waveguide mode and the SMF28 mode for different  $DC_m$ . Measurements (continuous line with crosses) are compared to simulation results (dashed line with circles).

Besides the reduction of the insertion losses, the use of segmented waveguide tapers offers the advantage of a wider cross-correlation function with the mode fiber. Figure 5.16 shows the sections of the measured bidimensional cross-correlation function between SMF28 and continuous waveguide (continuous line) and between SMF28 and segmented waveguide with  $DC_m = 0.5$  and  $W = 5 \mu m$  (dashed line). The resolution of these measurements is  $16 \text{ nm}$ , and is limited by the piezoelectric positioning system we used. The wider cross-correlation function, obtained using segmented waveguide, is the signature of a less critical alignment, which is important for industrial applications as it relaxes the constraints on the fiber pigtailling process and therefore its cost.

## 5.6 Tapers in quantum relay

These results are not only important in view of their practical applications in classical devices but promise also a lot of attracting features for many applications. For example, the so called quantum cryptography systems use a cryptography key, shared through a quantum channel, assuring a secure link between two individuals [6, 118]. In quantum communication the information is carried by single photons. For this reason, optical amplifiers can not be used, as in classical systems, to increase system performances (maximum distance of connection and bit-rate) and one can then only reduce losses. Moreover, as detectors are noisy and fibers lossy, the signal-to-noise ratio decreases with distance, and the maximum distance for a given fidelity is thus limited. Quantum relays have been used by Guillaume Bertocchi [119, 120] to overcome this problem using the photon entanglement in time bin [121]. Figure

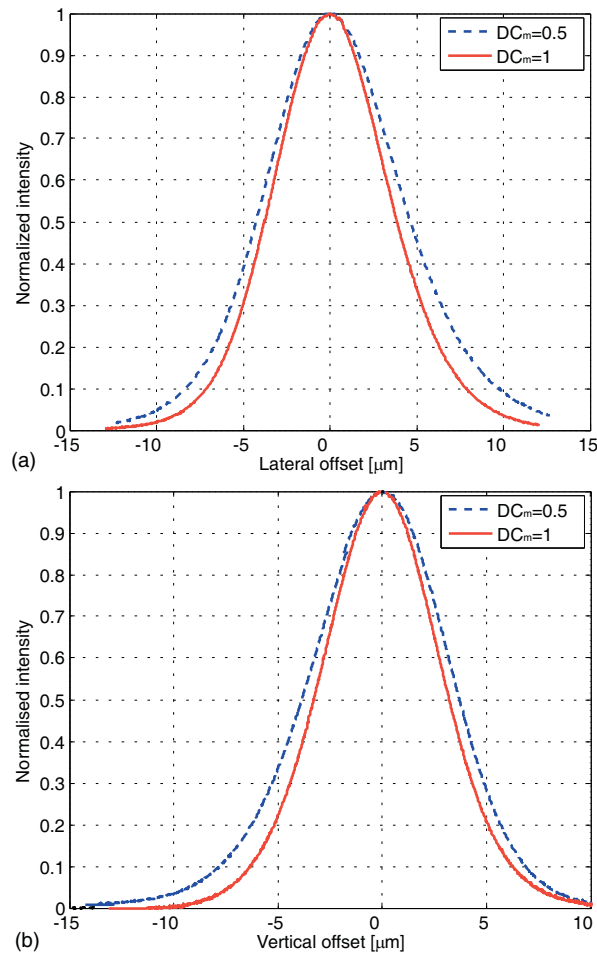


Figure 5.16: Lateral (a) and vertical (b) section of bidimensional cross-correlation function between SMF28 and continuous waveguide (continuous line) and between SMF28 and segmented waveguide (dashed line) with  $P = 15\mu\text{m}$ ,  $W = 5\mu\text{m}$  and  $DC_m = 0.5$ .

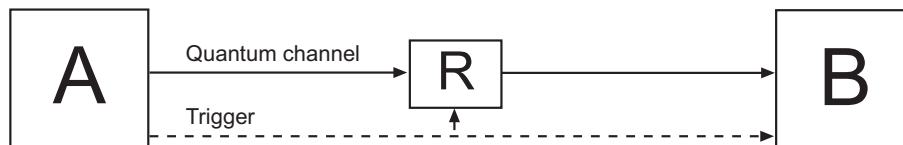


Figure 5.17: Quantum communication system with relay.

5.17 shows a schematic representation of the system. A is the photon source. When a single photon is transmitted on the quantum channel a second electrical trigger is launched too. In order to the maximum allowed distance between A and B a quantum relay R is placed before the receiver B. The quantum relay is based

on the photon teleportation phenomena [122]. A scheme of the integrated device realized by Bertocchi is shown in figure 5.18. Photons at  $0.775 \mu\text{m}$  come from

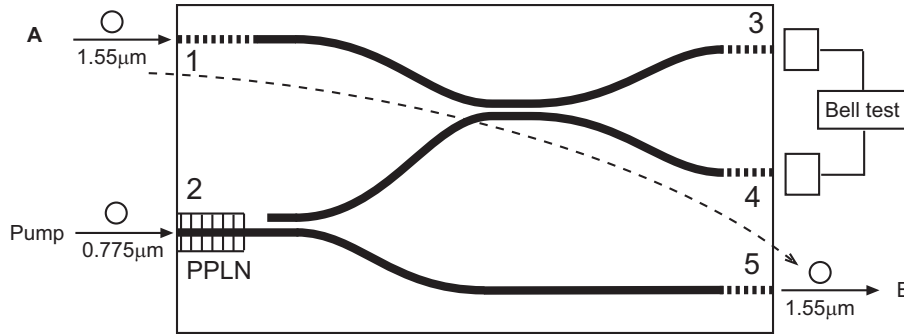


Figure 5.18: Schematic of the quantum relay.

the port 2; a Periodically Poled Lithium Niobate (PPLN) stage converts a single input photon into two photons at  $1.55 \mu\text{m}$ . This entangled pair is separated by a splitter and one photon is sent to a further coupler which perform the interaction with the photon coming from port 1. It is then necessary to perform a coincidence measurement of the two photons at the output of the second beam splitter (Bell state measurement). When a coincidence occurs we have the teleportation of the quantum state from input photon of port 1 to the output photon of port 5. The advantage is that an identical copy of the input photon is created and sent to B obtaining an improvement in terms of the signal to noise ratio. The performances of quantum relay are extremely penalized by system losses. In this case four of the five port interact with standard telecommunication fibers (ports 1,3,4,5) at  $1.55 \mu\text{m}$  and the presence of tapers to improve coupling efficiency is mandatory. Preliminary results obtained by Bertocchi with classical characterization techniques of this device confirm an insertion losses reduction of  $0.64 \pm 0.25 \text{ dB}$  when a taper is present. This value is in good agreement with ours results.



# 6

## Segmented waveguide mode filter

### 6.1 Introduction

In this chapter a further application of segmented waveguides will be presented: the so called mode filters. These devices eliminate the higher order modes propagating in a multimode waveguide. They can be used, for example, in frequency conversion applications based on non linear effects, where a pump at a lower wavelength should interact with a signal to generate an idler with a new wavelength. Usually the waveguide becomes multimode at the pump frequency and the contribution of the higher order modes can perturb the output spectrum. After illustrating the working principles of these devices and a simple model based on the Couple Mode Theory which proved very useful both for device design and analysis, some results proving the good performances of these devices will be presented and discussed [123].

### 6.2 Mode filter operation

Using the equivalent waveguide theorem for segmented waveguides we can argue that it is possible to tailor the device characteristics in such a way that if many modes are propagating in a waveguide, only the fundamental mode is preserved, while all the other modes are led to cutoff. That theorem suggests in fact that the cutoff wavelength of the propagating mode can be reduced by modifying the  $DC$  [19]. Figure 6.1, shows the cutoff wavelengths of the fundamental and the first higher order modes as a function of the  $DC$  of the segmented waveguide. Assuming, for example, a working wavelength of  $0.85 \mu m$ , one can see that, for  $DC < 0.39$ , the higher order mode is no longer guided, while the fundamental one still propagates until the  $DC$  becomes 0.29.

So, for a fixed wavelength, it is then possible to determine the  $DC$  interval for which only the fundamental mode can propagate. The transition between the multimode continuous waveguide to the segmented waveguide and vice versa can not

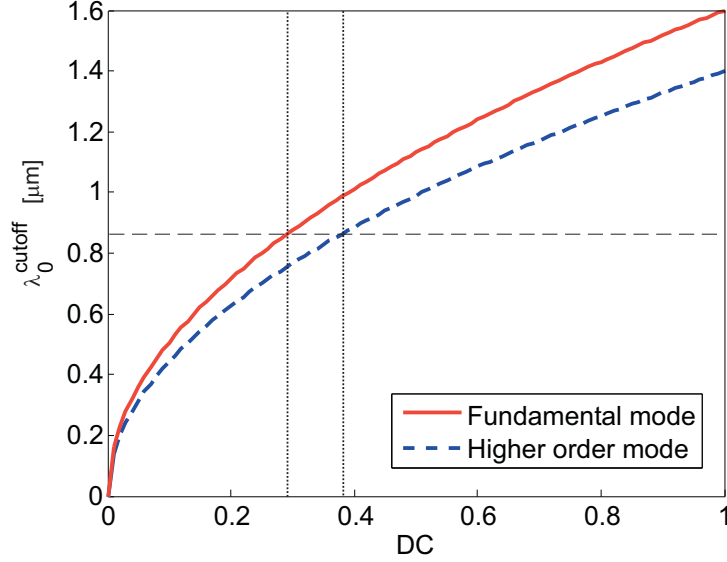


Figure 6.1: Cutoff wavelength for two modes of a segmented waveguide as a function of the duty cycle  $DC$ .

be abrupt but tapered to minimize losses. Moreover, in this case, the taper avoids the formation of unwanted higher order mode after the filtering process. A rapid transformation after the segmented waveguide can excite once again the modes of the multimode structure making useless the filter.

A schematic representation of a mode filter based on segmented waveguides proposed by Chou et al. [34] is shown in figure 6.2. In this solution, the segmented waveguide (SWG), which works as a mode filter, is placed at the entrance of the sample in order to obtain the double advantage of filtering the higher order modes and also of improving the overlap between the external mode fiber and the fundamental mode of the segmented waveguide.

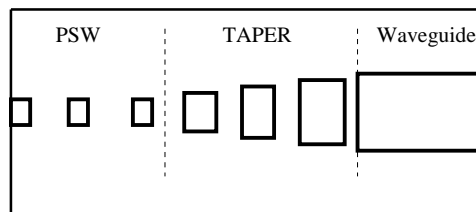


Figure 6.2: Schematic representation of a mode filter based on segmented waveguide proposed by Chou et al. [34].

The experimental results presented by Chou et al. are interesting, but in their

work the rules used for the taper design are not discussed. Knowledge of these rule would be important for best design and minimization of the excitation of the higher order mode. For this reason, we have developed a model based on the coupled mode theory (CMT) and the equivalent waveguide theorem able to study the coupling phenomena inside a segmented waveguide taper. This allows to predict the behavior of the taper and to fix its parameters to obtain the desired features.

### 6.3 Coupled Mode Theory for segmented waveguide mode filters

A continuous straight dielectric waveguide transmits any of its guided modes without coupling their energy to any other guided or radiation mode, as modes are mutually orthogonal [37]. It is possible to extend this orthogonality condition for modes of ideal segmented waveguide [24]. But any imperfection of the waveguide, such as a local change of its refractive index destroys the condition of perfect straightness or an imperfection of the interface between two regions with different refractive index of a segmented waveguide couples modes each other (guided and radiation). Imperfections of this type are unavoidable.

In our case both unwanted imperfections and segmentations with variable  $DC$  are present. Then, the modes that propagates trough a taper are not orthogonal and coupling phenomena occurs. The coupled mode theory (CMT) [38] can be used to understand how to design a taper in order to reduce the excitation of higher order modes. Such a theory is based on some simplifying assumptions. Usually, we call *unperturbed* structure, the structure for which we know a complete set of solutions, for example the continuous waveguide. Then, we consider a second structure, the so called *perturbed structure*, which is very similar to the unperturbed one, but with unknown solutions. In our case this second structure is the taper with imperfections. This second structure can be obtained modifying the unperturbed one by a physical or geometrical parameter that we call  $\Delta\epsilon$  defined as the difference between the dielectric distribution for the two structures. In the following we indicate with suffix 1 the unperturbed solutions, while we use the suffix 2 for the perturbed solutions. In harmonic regime and without sources, the Maxwell equations for the unperturbed structure can be written as:

$$\begin{aligned}\bar{\nabla} \times \bar{E}_1 &= -j\omega\mu\bar{H}_1 \\ \bar{\nabla} \times \bar{H}_1 &= j\omega\epsilon\bar{E}_1\end{aligned}\tag{6.1}$$

while, in the case of perturbed structure, they become:

$$\begin{aligned}\bar{\nabla} \times \bar{E}_2 &= -j\omega\mu\bar{H}_2 \\ \bar{\nabla} \times \bar{H}_2 &= j\omega(\epsilon + \Delta\epsilon)\bar{E}_2.\end{aligned}\tag{6.2}$$

Indicating with  $(\bar{E}_\nu(x, y), \bar{H}_\nu(x, y))$  the complete set of solutions for the unperturbed structure, considering only small perturbations, it can also be assumed that, the unknown field of the perturbed structure can be expressed as:

$$\bar{E}_{2t}(x, y, z) = \sum_{\nu} (a_{\nu} + b_{\nu}) \bar{E}_{t\nu}(x, y) \quad (6.3)$$

$$\bar{H}_{2t}(x, y, z) = \sum_{\nu} (a_{\nu} - b_{\nu}) \bar{H}_{t\nu}(x, y) \quad (6.4)$$

where the unknown coefficients:

$$a_{\nu}(z) = A_{\nu}(z) e^{-j\beta_{\nu}z} \quad (6.5)$$

$$b_{\nu}(z) = B_{\nu}(z) e^{j\beta_{\nu}z} \quad (6.6)$$

refer to the modes, which propagate in the positive direction and negative direction of the  $z$  axis. Note also that the mode propagation constants are assumed not to depend on the propagation coordinate  $z$  because of the small perturbations, while the mode amplitude depends on  $z$  as we are looking for coupling effects.

For simplicity we will assume also that no radiation mode is considered (this is compatible with the hypothesis of small perturbations) and that only two guided modes can propagate. After some well known algebra (see for example [38]) the equations to be solved to determine the unknown amplitude coefficients are found to be:

$$\begin{aligned} \frac{dA_1}{dz} &= -j\kappa A_2 e^{-j(\beta_2 - \beta_1)z} \\ \frac{dA_2}{dz} &= -j\kappa^* A_1 e^{-j(\beta_1 - \beta_2)z} \end{aligned} \quad (6.7)$$

where

$$\kappa = \frac{\omega}{4} \int \int_{-\infty}^{\infty} \Delta\epsilon \bar{E}_{t\nu} \cdot \bar{E}_{t\mu}^* dx dy \quad (6.8)$$

is the so called coupling coefficient between the transversal component of the mode of the perturbed structure  $\bar{E}_{t\mu}$  and the  $\nu$ -th mode of the unperturbed structure. In our case the only value to consider for  $\nu$  and  $\mu$  are for both of them 1 and 2.

The solution of the equations 6.7 is:

$$\begin{aligned} A_1 &= e^{j\frac{\Delta\beta}{2}z} \cdot (A_1' e^{jS_1 z} + A_1'' e^{-jS_1 z}) \\ A_2 &= e^{-j\frac{\Delta\beta}{2}z} \cdot (A_2' e^{jS_2 z} + A_2'' e^{-jS_2 z}) \end{aligned} \quad (6.9)$$

where

$$\Delta\beta = \beta_1 - \beta_2 \quad (6.10)$$

	Type	Parameter
Depth profile	Exponential	2.2 $\mu m$ (@1/e)
Width profile	Gaussian	3 $\mu m$ (@1/e)
$\delta n$		0.018

Table 6.1: Parameters of the refractive index profiles used to calculate  $\Delta\beta$ .

and  $S$  is defined as:

$$S = \sqrt{\left(\frac{\Delta\beta}{2}\right)^2 + |\kappa|^2}. \quad (6.11)$$

Constants  $A'_1, A''_1, A'_2$  and  $A''_2$  can be determined imposing the initial exciting condition for the two modes. The taper is placed after the mode filter and for this reason the power of the higher order mode is zero  $A_2(z=0) = 0$  and all the power is in the fundamental one. The guided powers of the two modes in the taper are found to be:

$$P_1(z) = |A_1(z)|^2 = P_0 \left[ \left(\frac{\Delta\beta}{2S}\right)^2 \sin^2(Sz) + \cos^2(Sz) \right] \quad (6.12)$$

$$P_2(z) = |A_2(z)|^2 = P_0 \frac{|\kappa|^2}{S^2} \sin^2(Sz) \quad (6.13)$$

where  $P_0$  is the initial section power.

To characterize the coupling phenomena it is then necessary to know both the values of  $\Delta\beta$  between the two propagating modes and of the coupling coefficient  $\kappa$ .  $\Delta\beta$  can be calculated with good approximation starting from the equivalent waveguide theorem and using a mode solver. Determining  $\kappa$  is a more difficult problem as the value of the coupling coefficient is related to the structure imperfections.

In particular, for what concerns the calculation of  $\Delta\beta$ , we have considered the model of the SPE waveguides obtained with the m-lines measurement and the IWKB method presented in chapter 3. The index profile has then been modified considering the dispersion relation for both the substrate and the  $\delta n$  for the working wavelength  $\lambda = 840 \text{ nm}$ , which has been used in the measurement. The details of the used profiles are summarized in table 6.1. This waveguide for  $DC_m = 1$ <sup>1</sup> and  $\lambda = 840 \text{ nm}$  is multimode, using the mode solver and the equivalent waveguide theorem it is possible to calculate the evolution of the effective index of the modes during propagation along the taper. In figure 6.3 for example is shown the effective index evolution for a cubic taper which passes from  $DC_m = 0.3$  to  $DC_m = 1$  with  $L = 2000 \mu m$ . Note that, at the beginning of the structure, only one mode is in propagation, the second

<sup>1</sup>See chapter 5 for the difference between  $DC$  and  $DC_m$ .

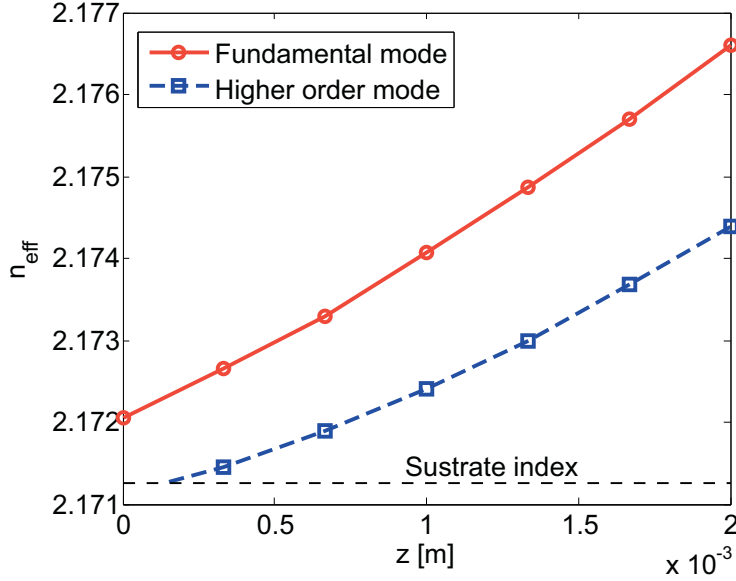


Figure 6.3: Effective index of the fundamental (red line) and higher order (blue dashed line) modes in propagation trough a cubic taper. The mode transformation is obtained passing from  $DC_m = 0.3$  to  $DC_m = 1$  with  $L = 2000 \mu m$ .

one come out from the cutoff condition for  $z > 0.2 \text{ mm}$ . The relative distance between the two effective indices during propagation is increased and as a consequence also  $\Delta\beta$  increase. Figure 6.4 shows the evolution of  $\Delta\beta$  in the taper.

The coupling coefficient  $\kappa$  has been evaluated assuming a sinusoidal profile to approximate the waveguide surface roughness, using the results published by Marcuse in [124]. This model provides value of the coupling coefficient of about  $\kappa = 4000m^{-1}$  in the case of continuous waveguide with perturbation amplitude equal to 1% of the transversal waveguide size. We have used this value of  $\kappa$  only for tapers of theoretically infinite length and for this reason it will be indicated as  $\kappa_\infty$  in the following. In this case in fact, the  $DC$  variation is so slow that we can consider only the effect of the roughness. Reducing the taper length, this value of  $\kappa$  must be increased to take into account also the perturbation induced by the variable  $DC$ .

Using equation 6.12 it is then possible to calculate the power evolution of the higher order mode in the taper with  $L = 2000 \mu m$ . This is shown in figure 6.5. In the taper, the higher order mode intensity presents decreasing oscillations during propagation. This result is related to the  $\Delta\beta$  evolution between the two modes previously described: for increasing  $\Delta\beta$ , in fact, coupling decreases.

For a taper design a more interesting result is the evolution of the mode intensity at the output of the taper as a function of its length. Repeating the calculation for different values of  $L$  and observing the output power, we obtain the results reported in figure 6.6, for three different values of  $\kappa_\infty = 5000, 4000, 3000m^{-1}$ . Note that

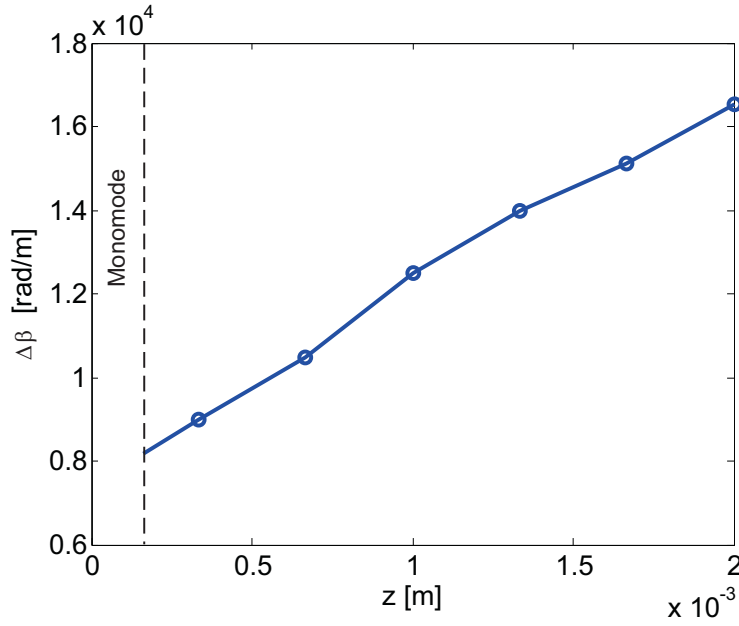


Figure 6.4:  $\Delta\beta$  between the two modes in propagation trough the taper. For  $z < 0.2 \text{ mm}$   $\Delta\beta$  is not defined because the taper is monomode.

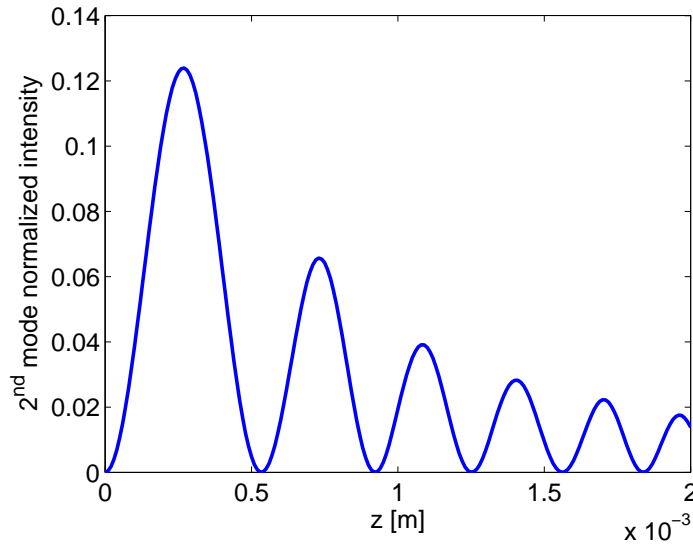


Figure 6.5: Power evolution of the higher order mode in the taper with  $L = 2000 \mu\text{m}$  and  $\kappa_\infty = 4000\text{m}^{-1}$ .

the slope of the  $\Delta\beta$  evolution depends on the value of the taper length  $L$  and this explains the difference between figure 6.5 and figure 6.6. The figure shows clearly that the oscillations are not constant and depend strongly on  $\kappa_\infty$ . These results

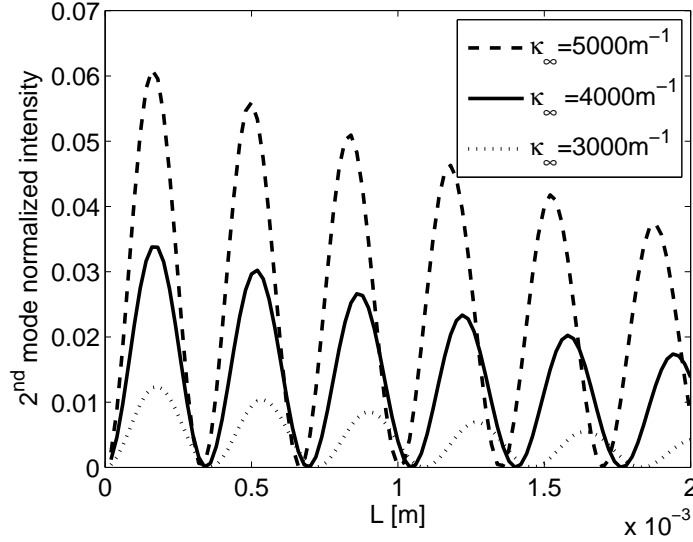


Figure 6.6: Power evolution of the higher order mode at the output of the taper as a function of the length  $L$  for  $\kappa_{\infty} = 4000m^{-1}$  (continuous line),  $\kappa_{\infty} = 5000m^{-1}$  (dashed line) and  $\kappa_{\infty} = 3000m^{-1}$  (dotted line).

also suggest that even a relatively short taper, if correctly designed, can prevent the excitation of the higher order mode. To do so, one must simply choose  $L$  in correspondence of an higher order mode minimum. However, this solution is critical because of the difficulty to evaluate correctly  $\kappa_{\infty}$ . In many cases, it is then much better to design a longer taper working with strongly attenuated oscillations. In this case, even if we don't know exactly the  $\kappa_{\infty}$  value, the higher order mode excitation results small.

## 6.4 Experimental results

In order to confirm the working principle of a segmented waveguide mode filter we have fabricated the devices sketched in figure 6.7. With respect the structure

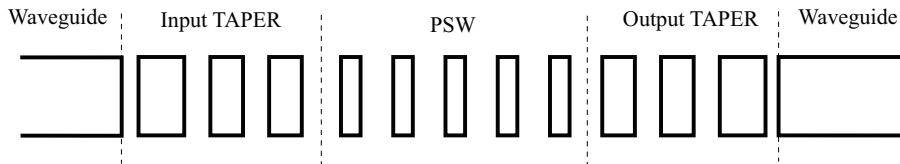


Figure 6.7: Scheme of the fabricated mode filter. The segmented waveguide (SWG) is placed between two continuous waveguide with two tapers to optimize coupling.

proposed by Chou et al. [34], the segmented waveguide is between two continuous

$DC_m$	$P$ [ $\mu m$ ]	$W$ [ $\mu m$ ]	$L$ [ $\mu m$ ]
0.3 - 0.4 - 0.5	10 - 15 - 25	5 - 7	100 - 600 - 1000 - 1600 - 2000

Table 6.2: Geometrical parameters of the taper.

waveguides and not at the edge of the sample. The input and output tapers are equal and the segmented waveguide is 5 mm long in order completely eliminate the mode at cutoff. These devices have been fabricated with different characteristic parameters. The values of the period  $P$ , the duty cycle  $DC_m$  and the taper length  $L$  combined to fabricate different structures are summarized in the following table 6.2.

In the sample, we have also fabricated continuous and segmented waveguides (without tapers) in order to evidence respectively the multimodality and the filter effect.

A schematic representation of the experimental setup adopted to characterize the properties of our mode filters is shown in figure 6.8. The source is a diode laser,

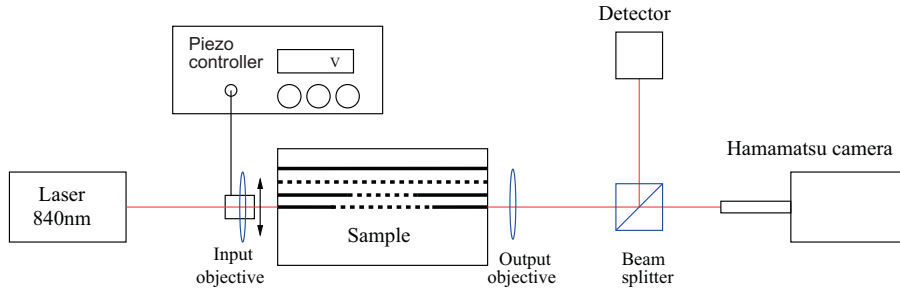


Figure 6.8: Experimental setup adopted to characterize the fabricated mode filters.

emitting at  $\lambda = 840 \text{ nm}$ . The incident beam is end fire coupled to the sample with an input microscope objective. The output signal is collected by an other microscope objective and then split by a semi-reflecting mirror. One beam is sent to an infrared camera (Hamamatsu) and the other one is sent to a detector for the evaluation of the transmitted power. The camera allows to visualize in real time on a monitor the shape of the near field and evaluate the possible presence of higher order modes. The input microscope objective is mounted on a piezoelectric stage. This system controls accurately the position of the objective allowing to modify the exciting condition of the waveguides.

The characterization procedure determines the signal power at the output of the sample as a function of the input objective position and records, at the same time, the camera images. Figure 6.9 shows the results we have obtained comparing the transmitted power in the case of continuous waveguide and of waveguide with mode filter and input and output tapers with  $L = 600 \mu m$ . The exciting condition

is modified horizontally in order to evidence the presence of a second order lateral mode in the continuous waveguide. The curves are then normalized to 1 to simplify comparisons.

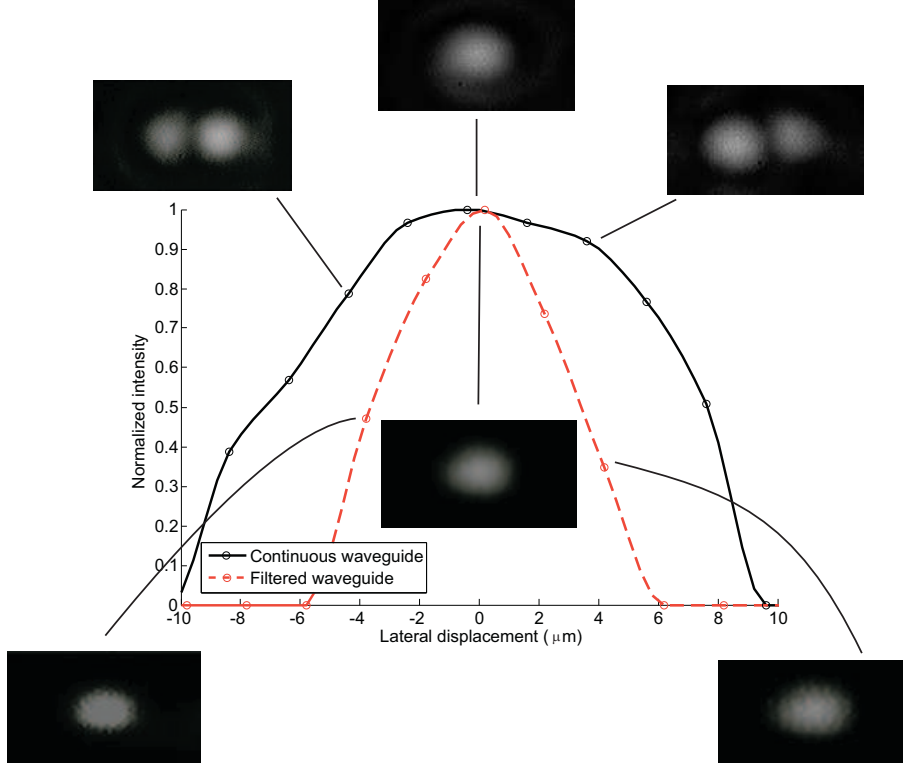


Figure 6.9: Measurement of the transmitted power as a function of the lateral displacement of the input objective for a continuous and a filtered waveguide. Camera images are placed to evidence the presence of the higher order mode at the output of the continuous waveguide and only the fundamental mode for the filtered waveguide.

The curve obtained for a waveguide with mode filter (dashed line) is sharper than that of the continuous waveguide as the contribution of the higher order mode is filtered. The camera images show in fact that the field at the output of the filtered waveguide is only the fundamental mode while the presence of the higher order mode appears clearly for the continuous waveguide. To quantify this effect we calculate the standard deviation (square root of the variance)  $\sigma$  defined as:

$$\sigma = \sqrt{\sum_j I_j |\Delta x_j - \mu|^2} \quad (6.14)$$

where the sum is extended to the measured intensity  $I_j$  obtained in correspondence of a lateral displacement  $\Delta x_j$  and  $\mu$  is the arithmetic mean defined as:

$$\mu = \frac{\sum_j \Delta x_j I_j}{\sum_j I_j}. \quad (6.15)$$

We found that  $\sigma = 3.55 \mu\text{m}$  for the waveguide with mode filter and  $\sigma = 8.2 \mu\text{m}$  for the waveguide without mode filter. We have then repeated the measurement for different values of taper length  $L$ . In particular, when  $L = 2000 \mu\text{m}$  we have obtained the results reported in figure 6.10. As expected for a taper of length  $L = 2000 \mu\text{m}$  the

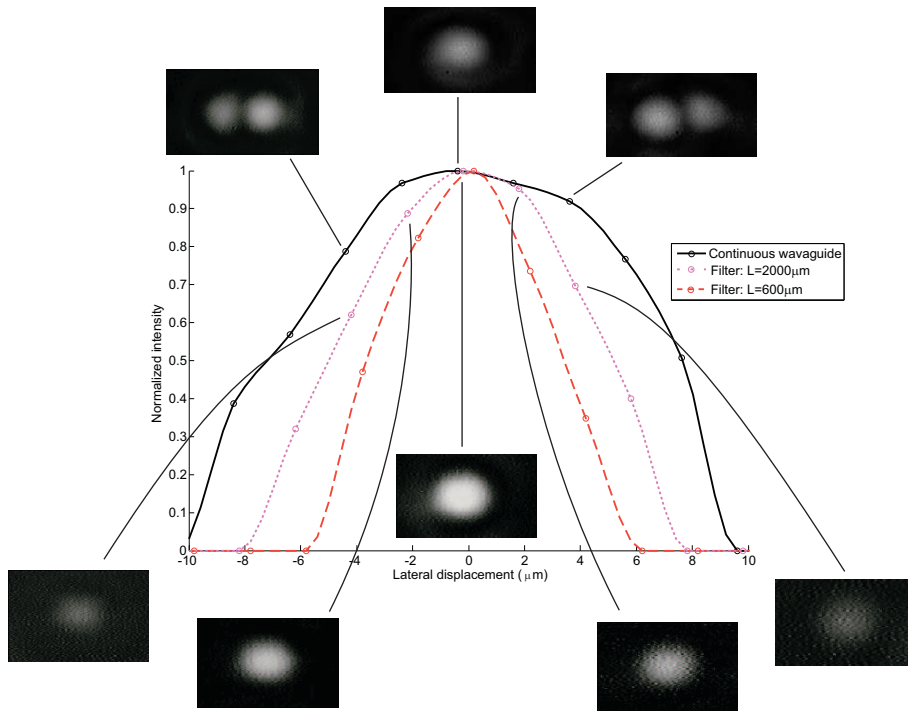


Figure 6.10: Measurement of the transmitted power as a function of the lateral displacement of the input objective for a continuous and two filtered waveguides with taper length  $L = 600 \mu\text{m}$  (dashed line) and  $L = 2000 \mu\text{m}$  (dotted line). The camera images confirm the monomodality of the filtered waveguide also for  $L = 2000 \mu\text{m}$ .

output field presents only the fundamental mode. However, rather surprisingly, the width of the transmission curve as a function of the lateral displacement is larger than in the case of a taper with  $L = 600 \mu\text{m}$ . For  $L = 2000 \mu\text{m}$ , in fact, the value of  $\sigma$  become  $5.79 \mu\text{m}$ . The surprising result is that  $\sigma$  increases despite we would have expected a decrease as larger taper are expected to provide better filtering conditions.

A possible explanation can come from the role played by the input taper. This taper are expected to convert efficiently the energy of the fundamental mode of the

input continuous waveguide into the fundamental mode of the segmented one. In practice, the coupling phenomenon discussed for the output taper occurs also for the input taper. Applying the CMT equations in this case, the coupling effect occurring between taper modes can justify the result of figure 6.10. Assuming that we excite only the higher order mode of the input continuous waveguide, using the equations 6.12, we can calculate the evolution of the fundamental mode power intensity in the taper. This result is shown in figure 6.11.

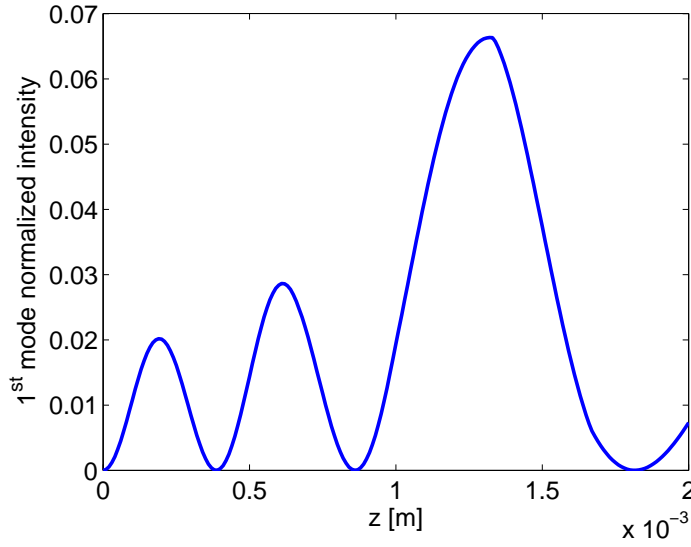


Figure 6.11: Calculation of the normalized fundamental mode intensity in the input taper.

Repeating the calculation for different taper lengths  $L$  and collecting the fundamental mode intensity at the output taper, we obtained the results reported in figure 6.12, which shows that the beneficial effect of the input taper is that part of the energy of the excited higher order mode can couple to the fundamental one and can be transmitted unperturbed through the mode filter. The result presented in figure 6.12 shows that the transferred power from the excited higher order mode and the fundamental one can vary from 0 to 22-29 % as a function of  $L$ . This numerical prediction of our model is quantitatively confirmed by the measurements shown in figure 6.10. When the lateral displacement of the exciting beam is  $6\mu m$ , in fact, the fundamental mode is almost absent as the transmitted power through the filter with taper length  $L = 600\mu m$  is zero. At the same lateral displacement condition, using the filter with taper length  $L = 2000\mu m$ , we measured an output power improvement, related to the mode conversion, of about 30%, which is in good agreement with the model previsions. This also means that, in our case, the chosen  $\kappa_\infty$  value of  $4000m^{-1}$  corresponding to a roughness of about 1% of the waveguide width is approximatively correct.

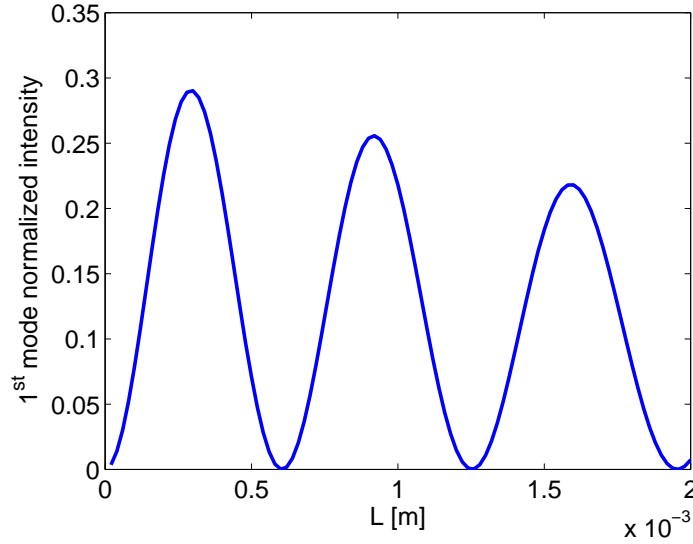


Figure 6.12: Calculation of the normalized fundamental mode intensity at the output of the taper as a function of the taper length  $L$ .

The power transfer from the higher order mode to the fundamental one increases the width  $\sigma$  of the transmission curves as a function of the lateral displacement, explaining the result of figure 6.10. For this reason, oscillations of the fundamental mode intensity (figure 6.12) must correspond to oscillations of the width  $\sigma$ . This has been experimentally verified characterizing mode filters with different periods  $P$  and length  $L$  and obtaining the results reported in figure 6.13. The value of  $\sigma$  varies as a function of the taper length  $L$ . Moreover, it is important to note also that increasing the period  $P$ , the oscillation period is reduced. This behavior can be explained using the equivalent waveguide theorem. In fact increasing the period, the real  $DC$  increases and the equivalent waveguide presents a larger step index. As a consequence  $\Delta\beta$  between the modes increases and the coupling length and  $\sigma$  are reduced. A period  $P$  decrease reduces also the filter capability and this explains why the minimum of the curves corresponds to higher values of  $\sigma$ .

The coupling phenomenon observed at the input taper that allows to transfer energy from an higher order mode to the fundamental one can be used to improve the coupling efficiency of an integrated waveguide with external component like fibers or objectives. Note however that coupling is a reversible phenomena. This means that if we excite perfectly the fundamental mode, part of the energy will be transferred to the higher order modes, contributing to the losses.

In conclusion, a solution without input taper (see Chou et al. [34]) requires a perfect alignment to obtain high transmitted power, with the drawback that small misalignments with respect to the optimum condition introduce losses. In solution proposed here, in case of perfect alignment the device is affected by losses, but has

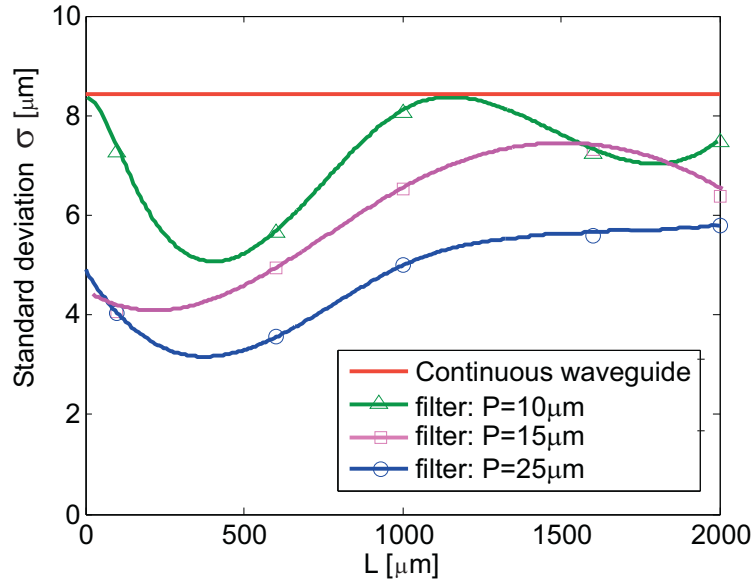


Figure 6.13: Measurement of the width  $\sigma$  as a function of the taper length  $L$  for different period  $P$ . The red line corresponds to the reference width  $\sigma$  obtained in the case of multimode continuous waveguide.

better coupling tolerances with external devices. This is important in case of fiber optics pigtailling where the cost of the system is related to the desired alignment precision.

The drawback of this structure is that device behavior is strongly dependent on the coupling coefficient  $\kappa$ , which depends on technological imperfections. As a consequence, the design of the structure may be very difficult and the results not reproducible. To overcome this problem we propose a new structure that can be obtained introducing a purpose surface roughness (figure 6.14).

The periodicity of the lateral profile of the input taper can be used to obtain the

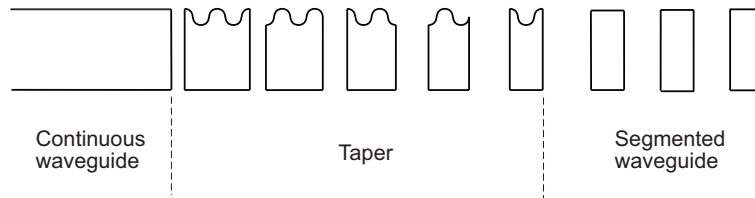


Figure 6.14: Schematic of mode filter with controlled artificial irregularity at the input taper.

phase matching condition between the modes we want to couple. In this case, propagation losses would not be increased because the matching will be between propagating mode instead of radiating modes. Note also that being  $\Delta\beta$  variable in

the taper also the periodicity of the lateral profile must change longitudinally.



# Conclusions

In this thesis, we have reported the main results achieved during my work concerning new devices for photonics applications. The research has been developed following all the steps which lead to the realization of a device prototype in integrated optics: its design, developing and using suitable numerical tools, the choice of the substrate material in which the device is fabricated and the relevant technology, and its characterization, with a suitable experimental setup. Following all these steps allowed me to merge the interest for physical insight into the basics of device behavior, which animates the doctorate “Spécialité Physique” of the University of Nice-Sophia Antipolis, and the engineering oriented search of feasible and cost effective components, underlying the activities of the doctorate in “Ingegneria Elettronica, Informatica e delle Telecomunicazioni” of the University of Bologna. This is in fact a co-tutored PhD made possible by the “*Università Italo-Francese*”, who provided a fellowship in the framework of the *Vinci Program*.

The problem to tackle and hopefully to solve concerned possible devices able to reduce losses when connecting waveguides of different shape and/or materials. This is still a challenging issue in optical telecommunication systems, either to reduce coupling losses, or to allow less critical, and then less expensive, coupling between different devices.

Physics of periodic, or almost periodic, structures has been chosen as basic principle for device operation as it seemed that properties of these waveguides fitted well both simplicity and possibility of tailoring device functionality. So, after studying their main characteristics of light propagation in these structures, an investigation on their many applications in optics has been done, evidencing their possible applications to our purposes.

The characteristics of these structures prevent the use of analytical approaches, except that for preliminary or simplified analysis. So some numerical tools have been developed, aiming at studying propagation in these structures. In particular, a Finite Difference 3D-Beam Propagation Method (3D-BPM), based on the electric field formulation of the Helmholtz equations, previously developed in the Italian group, has been improved and adapted for the study of segmented waveguide structures. Moreover, we have completely developed a second version of this tool, based on the magnetic field formulation, to solve some numerical instability problems intrinsic of the previous version. In both cases we have implemented Perfect Matched Layer

(PML) boundary conditions and Padé approximants for wide angle propagation analysis. In parallel to this, we have also developed a mode solver, able to study longitudinally invariant structures, such as optical fibers and continuous waveguides. This tool can also be used to determine the input field necessary to run BPM simulations.

A second step to do was the choice of the material and the technology to be used for waveguide fabrication. Lithium Niobate substrate and Soft Proton Exchange (SPE) technology have been chosen. Lithium Niobate is in fact one of the favorite materials in integrated optics because of its very good linear and nonlinear properties. The SPE technique is routinely used in the French laboratory where the experimental part of the work has been developed. Using this technique and using CAD assisted design, we have then fabricated segmented waveguide tapers and mode filters. This part required a merge of the two different expertises. In fact numerical modelling of waveguides depends strongly on the used material and fabrication technology, also to include a realistic model of the structure. This allowed, for example, to identify in the roughness of the sample's surface a fabrication problem to be considered to improve the present fabrication technology.

Once waveguides have been fabricated, they have also to be characterized. We have then identified the main parameters to be measured (propagation losses, effective group index and mode size) and set up an apparatus to measure them. The system is controlled by a computer with a Labview program which allows to perform automatic measurements. Precautions have been adopted to avoid systematic errors (spurious cavities between sample and fibers, mechanical changes due to operator induced temperature variations, etc.). Possible ways for further improvement of precision and accuracy of the setup have been identified: lasers with stable internal or external polarization control to guarantee good polarization stability for wide wavelength ranges, positioning control of the piezoelectric adjuster with capacitive probes to increase spatial scanning resolution up to nanometric precision and to eliminate the hysteresis problems and the temporal drift.

The versatility and the possibilities offered by the proposed setup have been confirmed by the results of measurements performed on various samples, either integrated optical waveguides or optical fibers. Using this setup we have characterized segmented waveguide tapers fabricated in  $LiNbO_3$  by the SPE process. Experimental results have been obtained at telecom wavelengths. We have found that when one uses the SPE parameters necessary to reach the maximum confinement of the guided mode, preserving non-linear and electro-optical coefficients, the introduction of an adapted taper allows reducing by 0.78 dB the coupling losses with a standard SMF-28 fiber. For a complete device, presenting optimized tapers at input and output, the benefit could then reach 1.5 dB. All the experimental results are in good agreement with the numerical analysis confirming the precision of the developed numerical tools and the quality of the model. This structure has been introduced in a more complicated structure, a quantum relay developed at LPMC by Guillaume

Bertocchi to be used in quantum transmission experiments, obtaining the expected improvement in terms of insertion losses.

We have also designed, realized and characterized a segmented waveguide acting as a mode filter operating at  $\lambda = 840 \text{ nm}$ . A new structure has been proposed and a semi-analytical formulation, based on the Coupled Mode Theory, has been used to design the filter parameters. The measurement setup able to characterize this device uses a camera to acquire the near field at the output of the sample, evaluating the presence of higher order modes, while the position of the input microscope objective, used to launch the light in the waveguide, is modified through a piezoelectric system. The output power is also measured as a function of the exciting condition in order to evaluate the coupling sensibility. Experimentally, the second higher order mode has been successfully eliminated from a multimode continuous waveguide. During the characterization procedure we have obtained interesting result on the output power measurements as a function of the objective position. We have proposed an explanation, considering the mode coupling at the entrance of the filter, obtaining agreements with experimental results.

These devices should hopefully be useful to improve coupling between fibers and integrated optical devices allowing both mode mismatch and alignment tolerance reduction. The mode filter has also interesting applications in non linear optics experiments, eliminating higher order pump modes as their presence can perturb the non linear process efficiency and the output spectrum by generating undesired wavelengths.



# Author's references

- R. Zoli, M. Gnan, D. Castaldini, G. Bellanca, and P. Bassi, "Reformulation of the plane wave method to model photonic crystal", *OSA Optics Express*, November 3, vol. 11, p. 2905-2910, 2003.
- R. Zoli, D. Castaldini, M. Gnan, G. Bellanca, and P. Bassi, "2d and 3d numerical investigation of photonic crystal waveguides", *Proceedings of NUMELEC*, 2003.
- D. Castaldini, R. Zoli, A. Parini, G. Bellanca, and P. Bassi, "2d or 3d fdtd for photonic crystal waveguides modeling?", *Proceedings of PIERS 2004, Progress in Electromagnetics Research Symposium*, 28-31 March 2004, Pisa, Italy, pp. 381-384.
- D. Castaldini, "Analisi accurata di guide a cristallo fotonico 3d," *Atti della XV RiNEM, Riunione Nazionale di Elettromagnetismo*, Cagliari, 13-16 Settembre 2004.
- G. Bertocchi, D. Castaldini, S. Tascu, D. B. Ostrowsky, S. Tanzilli, M. De Micheli, and P. Baldi, "Integrated-optics quantum relay : Preliminary results", *Proceedings of the 32nd European Conference on Optical Communication (ECOC)*, Cannes, 24th-28th September 2006, vol 6, Paper We3.P.200, pp.91-92.
- D. Castaldini, P. Bassi, S. Tascu, S. Gregory, P. Aschieri, M. De Micheli, P. Baldi, K. Thyagarajan, and M. R. Shenoy, "All-in-one measurement setup for fast and accurate characterization of linear guided-wave optical devices", submitted to *Optical Engineering*.
- D. Castaldini, P. Bassi, S. Tascu, P. Aschieri, M. De Micheli, and P. Baldi, "Soft proton exchange tapers for low insertion loss  $LiNbO_3$  devices", accepted for publication in the IEEE/OSA Journal of Lightwave Technology.
- D. Castaldini, P. Bassi, G. Bertocchi, S. Tascu, P. Aschieri, M. De Micheli, S. Tanzilli and P. Baldi "Segmented waveguide tapers for low insertion loss, high performance SPE:LiNbO<sub>3</sub> integrated circuits", *accepted for 13th European Conference on Integrated Optics (ECIO)*, 25-27 April 2007.



# Bibliography

- [1] G. P. Agrawal, *Fiber-optic communication systems*, 3rd, Ed. J. Wiley & Sons, 2002.
- [2] D. Hussein, T. Mouftah, and J. Zheng, *Optical WDM Networks: Concepts and design principles*. Wiley-IEEE, 2004.
- [3] R. W. Boyd, *Nonlinear Optics*. Elsevier, 2003.
- [4] H. Herrmann and W. Sohler, "Difference-frequency generation of tunable, coherent mid-infrared radiation in  $Ti : LiNbO_3$  channel waveguides," *J. Opt. Soc. Am. B*, vol. 5, p. 278, 1988.
- [5] C. H. Bennett and D. P. D. Vincenzo, "Quantum information and computation," *Nature*, vol. 404, pp. 247–255, 2000.
- [6] D. Bouwmeester, A. K. Ekert, and A. Zeilinger, *The Physics of Quantum Information: Quantum Cryptography, Quantum Teleportation, Quantum Computation*. Springer Verlag, 2000.
- [7] K. Sakoda, *Optical properties of photonic crystals*. Springer, 2001.
- [8] D. D. Stancil, "Kronig-penney model for periodically segmented waveguides," *Applied Optics*, vol. 35, p. 4767, 1996.
- [9] A. Yariv and P. Yeh, *Optical Waves in Crystals*. J. Wiley & Sons, 1984.
- [10] R. E. Collin, "Reflection and transmission at a slotted dielectric interface," *Can.J.Phys*, vol. 34, p. 398, 1956.
- [11] L. R. Lewis and A. Hessel, "Propagation characteristics of periodic arrays of dielectric slabs," *IEEE Transactions on Microwave Theory and Techniques*, vol. MTT-19, p. 276, 1971.
- [12] K. Thyagarajan, C. W. Chien, R. V. Ramaswamy, H. S. Kim, and H. C. Cheng, "Proton-exchanged periodically segmented waveguides in  $LiNbO_3$ ," *Optics Letters*, vol. 19, p. 880, 1994.

- 
- [13] K. Thyagarajan, V. Mahalakshmi, and M. R. Shenoy, "Propagation characteristics of planar segmented waveguides with parabolic index segments," *Optics Letters*, vol. 19, p. 2113, 1994.
- [14] F. Fogli, N. Greco, P. Bassi, G. Bellanca, P. Aschieri, and P. Baldi, "Spatial harmonics modeling of planar periodic segmented waveguide," *Optical and Quantum Electronics*, vol. 33, no. 4-5, pp. 485–498, 2001.
- [15] F. Fogli, G. Bellanca, P. Aschieri, M. De Micheli, and P. Bassi, "Spatial harmonics analysis of deep waveguide bragg gratings," *Opt. A*, vol. 6, pp. 433–438, 2004.
- [16] L. Li and J. J. Burke, "Linear propagation characteristics of periodically segmented waveguides," *Optics Letters*, vol. 17, no. 17, pp. 1195–1197, September 1992.
- [17] J. D. Bierlein, "Propagation in segmented waveguide structures," *Quantum Electronics and Laser Science*, vol. 13, p. 42, 1992.
- [18] V. Rastogi, V. Mahalakshmi, M. R. Shenoy, and K. Thyagarajan, "Propagation characteristics of a novel complementary-structure planar segmented waveguide," *Optics Communications*, vol. 148, pp. 230–235, 1998.
- [19] D. Ortega, R. M. De La Rue, and J. S. Aitchison, "Cutoff wavelength of periodically segmented waveguides in  $Ti : LiNbO_3$ ," *IEEE Journal Of Lightwave Technology*, vol. 16, pp. 284–291, 1998.
- [20] G. B. Hocker and W. Burns, "Modes in diffused optical waveguides of arbitrary index profile," *IEEE Journal of Quantum Electronics*, vol. QE-11, pp. 270–276, 1975.
- [21] A. W. Snyder and R. M. De La Rue, "Asymptotic solution of eigenvalue equations for surface waveguide structures," *IEEE Transactions Microwave Theory Tech.*, vol. MTT-18, p. 650, 1970.
- [22] H. Kogelnik and W. Burns, "Scaling rules for thin-film optical waveguides," *Applied Optics*, vol. 13, pp. 1857–1862, 1974.
- [23] G. B. Hocker and W. Burns, "Mode dispersion in diffused channel waveguides by the effective index method," *Applied Optics*, vol. 16, pp. 113–118, 1977.
- [24] S. G. Johnson, P. Bienstman, M. A. Skorobogatiy, M. Ibanescu, E. Lidorikis, and J. D. Joannopoulos, "Adiabatic theorem and continuous coupled-mode theory for efficient taper transition in photonic crystal," *Physical Review*, vol. 66, pp. 1–15, 2002.

- 
- [25] R. Kashyap, *Fiber Bragg Gratings*. Academic Press, 1999.
- [26] M. L. Povinelli, S. G. Johnson, and J. D. Joannopoulos, "Slow-light, band-edge waveguides for tunable time delays," *Nature*, vol. 438, p. 65, 2005.
- [27] R. de Ridder, R. Wijbrans, H. Albers, J. Aukema, P. Lambeck, J. Hoekstra, and A. Driessen, "A spot-size transformer for fiber-chip coupling in sensor applications at 633 nm in silicon oxynitride," in *Lasers and Electro-Optics Society Annual Meeting, 1995. 8th Annual Meeting Conference Proceedings, Volume 1., IEEE*, vol. 2, 30-31 Oct. 1995, pp. 86–87vol.2.
- [28] Z. Weissman, "Evanescent field sensors with periodically segmented waveguides," *Applied Optics*, vol. 36, p. 1218, 1997.
- [29] J. V. Lith, P. Lambeck, H. Hoekstra, R. Heideman, and R. Wijn, "The segmented waveguide sensor: principle and experiments," *IEEE Journal of Lightwave Technology*, vol. 23, no. 1, pp. 355–363, Jan. 2005.
- [30] A. B. Aceves, "Optical gap solitons: Past, present, and future: theory and experiments," *CHAOS*, vol. 10, pp. 584–589, 2000.
- [31] S. Trillo and W. Torruellas, *Spatial solitons*. Springer, 2001.
- [32] P. Baldi, M. R. Shenoy, S. Nouh, M. De Micheli, and D. B. Ostrowsky, "Estimation of the extent and influence of longitudinal diffusion on  $LiNbO_3$  proton exchanged segmented stripe waveguides," *Optics Communications*, vol. 104, pp. 308–312, 1994.
- [33] Z. Weissman and A. Hardy, "2-d mode tapering via tapered channel waveguide segmentation," *Electronics letters*, vol. 28, p. 1514, 1992.
- [34] M. H. Chou, M. A. Arbore, and M. M. Fejer, "Adiabatically tapered periodic segmentation of channel waveguides for mode size transformation and fundamental mode excitation," *Optics Letters*, vol. 21, pp. 794–796, 1996.
- [35] F. Fogli, G. Bellanca, P. Bassi, I. Madden, and W. Johnstone, "Highly efficient full-vectorial 3-D BPM modeling of fiber to planar waveguide couplers," *IEEE Journal of Lightwave Technology*, vol. 17, no. 1, pp. 136–143, Jan. 1999.
- [36] F. Fogli, G. Bellanca, and P. Bassi, "Tbc and pml conditions for 2d and 3d bpm : a comparison," *Optical and quantum electronics*, vol. 30, pp. 443–456, 1998.
- [37] J. A. Stratton, *Electromagnetic theory*. Mc Graw Hill, 1941.
- [38] P. Bassi, G. Bellanca, and G. Tartarini, *Propagazione ottica libera e guidata*. Clueb, 1999.

- [39] D. Yevick, "The application of complex padé approximants to vector field propagation," *IEEE Photon. Technol. Lett.*, vol. 12, no. 12, pp. 1636–1638, 2000.
- [40] G. R. Hadley, "Wide-angle beam propagation using padé approximant operators," *Optics Letters*, vol. 17, pp. 1426–1428, 1992.
- [41] K. Saitoh and M. Koshiba, "Approximate scalar finite-element beam-propagation method with perfectly matched layers for anisotropic optical waveguides," *J. Light-wave Technol.*, vol. 19, no. 5, pp. 786–792, 2001.
- [42] G. D. Smith, *Numerical Solution of partial differential equations: finite difference methods*. Oxford University Press, 1985.
- [43] D. Li, "The fully vectorial beam propagation method," Ph.D. dissertation, Delft, 1995.
- [44] C. L. Xu, W. P. Huang, S. K. Chaudhuri, and J. Chrostowski, "An unconditionally stable vectorial beam propagation method for 3-d structures," *IEEE Photon. Technol. Lett.*, vol. 6, no. 4, pp. 549–551, 1994.
- [45] C. L. Xu and W. P. Huang, "Finite-difference beam-propagation method for guide-wave optics," in *Progress In Electromagnetic Waves: PIERS 11, Cambridge*, 1995.
- [46] J. L. Volakis, A. Chatterjee, and L. C. Kempel, *Finite Element Method for Electromagnetics: Antennas, Microwave Circuits, and Scattering Applications*. IEEE Press, 1998.
- [47] Y. Saad, *Iterative methods for sparse linear systems*. 2nd ed. Philadelphia: Society for Industrial and Applied Mathematics (SIAM), 2003.
- [48] G. R. Hadley, "Transparent boundary condition for beam propagation," *Optics Letters*, vol. 16, no. 9, pp. 624–626, 1991.
- [49] J.-P. Berenger, "A perfectly matched layer for the absorption of electromagnetic waves," *Journal of Computational Physics*, vol. 114, pp. 185–200, 1994.
- [50] Z. Sacks, D. Kingsland, R. Lee, and J.-F. Lee, "A perfectly matched anisotropic absorber for use as an absorbing boundary condition," *Antennas and Propagation, IEEE Transactions on*, vol. 43, no. 12, pp. 1460–1463, Dec. 1995.
- [51] A. Cucinotta, G. Pelosi, S. Selleri, L. Vincetti, and M. Zoboli, "Perfectly matched anisotropic layers for optical waveguides analysis through the finite element beam propagation method," *Microwave and Optical Technology Letters*, vol. 23, no. 2, pp. 67–69, 1999.

- 
- [52] W. P. Huang, C. L. Xu, W. Lui, and K. Yokoyama, "The perfectly matched layer (pml) boundary condition for the beam propagation method," *IEEE Photon. Technol. Lett.*, vol. 8, no. 5, pp. 649–651, 1996.
- [53] M. Hikari, M. Koshiba, and Y. Tsuji, "A time domain beam propagation method based on a finite element scheme," *Electronics and Communications in Japan*, vol. 82, pp. 52–58, 1999.
- [54] C. Vassallo, "Wide-angle bpm and power conservation," *IEE Electron. Lett.*, vol. 31, pp. 130–131, 1995.
- [55] P. Lüsse, P. Stuwe, J. Schüle, and H. G. Unger, "Analysis of vectorial mode fields in optical waveguide by a new finite difference method," *IEEE Journal of Lightwave Technology*, vol. 12, no. 3, pp. 487–494, 1994.
- [56] M. J. Robertson, S. Ritchie, and P. Dayan, "Semiconductor waveguides: analysis of optical propagation in single rib structures and directional couplers," *Proc. Inst. Elec. Eng.*, vol. 132, pp. 336–342, 1985.
- [57] A. Delage, "Modelling of semiconductor rib waveguides by a finite difference method," *Can. J. Phys.*, vol. 69, pp. 512–519, 1991.
- [58] A. Vassallo, "Improved finite difference deviation of semi-vectorial modes in 3d step index waveguides," in *European conference on optical communications, Berlin*, 1991.
- [59] M. S. Stern, "Semivectorial polarised finite difference methods for optical waveguides with arbitrary index profiles," *Proc. Inst. Elec. Eng.*, vol. 135, pp. 56–63, 1988.
- [60] M. Fujimura and T. Suhara, *Waveguide Nonlinear Optic Devices*. Springer, 2003.
- [61] J. R. Carruthers, I. P. Kaminow, and L. W. Stulz, "Diffusion kinetics and optical waveguiding properties of outdiffused layers in lithium niobate and lithium tantalite," *App. Opt.*, vol. 13, pp. 2333–2342, 1974.
- [62] G. J. Griffiths and R. J. Esdaile, "Analysis of titanium diffused planar optical waveguides in lithium niobate," *IEEE Journal of Quantum Electronics*, vol. 20, pp. 149–159, 1984.
- [63] M. L. Shah, "Optical waveguides in  $LiNbO_3$  by ion exchange technique," *App. Phys. Lett.*, vol. 26, pp. 652–653, 1975.
- [64] J. L. Jackel, C. E. Rice, and J. J. Veselka, "Proton exchange for high-index waveguides in  $LiNbO_3$ ," *App. Phys. Lett.*, vol. 41, pp. 607–608, 1982.

- [65] M. L. Bortz and M. M. Fejer, "Annealed proton-exchanged  $LiNbO_3$  waveguides," *Opt. Lett.*, vol. 16, pp. 1844–1846, 1991.
- [66] L. Chanvillard, P. Aschieri, P. Baldi, D. B. Ostrowsky, M. De Micheli, L. Huang, and D. J. Bamford, "Soft proton exchange on PPLN: a simple waveguide fabrication process for highly efficient non-linear interactions," *Appl. Phys. Lett.*, vol. 76, pp. 1089–1091, 2000.
- [67] Y. N. Korkishko and V. A. Fedorov, "Structural phase diagram of  $H_xLi_{1-x}NbO_3$  waveguides: the correlation between optical and structural properties," *IEEE Journal of Selected Topics in Quantum Electronics*, vol. 2, pp. 187–196, 1996.
- [68] C. Canali, A. Carnera, G. della Mea, P. Mazzoldi, S. M. A. Shukri, A. C. G. Nutt, and R. M. De La Rue, "Structural characterization of proton exchanged  $LiNbO_3$  optical waveguides," *J. Appl. Phys.*, vol. 59, pp. 2643–2649, 1986.
- [69] Y. N. Korkishko, V. A. Fedorov, E. A. Baranov, M. V. Proyaeva, T. V. Morozova, F. Caccavale, F. Segato, C. Sada, and S. M. Kostitskii, "Characterization of alpha-phase soft proton-exchanged  $LiNbO_3$  optical waveguides," *JOSA A*, vol. 18, pp. 1186–1191, 2001.
- [70] K. E. Hadi, V. Rastogi, M. R. Shenoy, K. Thyagarajan, M. De Micheli, and D. B. Ostrowsky, "Spectral measurement of the film substrate index difference in proton-exchanged  $LiNbO_3$  waveguides," *Applied Optics*, vol. 37, pp. 6463–6467, 1998.
- [71] P. Aumont, "Réalisation par échange protonique doux de guides continus et segmentés sur niobate de lithium," Ph.D. dissertation, Laboratoire de Physique de la Matière Condensée, 2003.
- [72] [Online]. Available: [www.barnardmicrosystems.com](http://www.barnardmicrosystems.com)
- [73] [Online]. Available: [www.photonics.com](http://www.photonics.com)
- [74] P. Aschieri, V. Rastogi, L. Chanvillard, P. Baldi, M. De Micheli, D. B. Ostrowsky, G. Bellanca, P. Bassi, K. Thyagarajan, and M. R. Shenoy, "Experimental observation of longitudinal modulation of mode fields in periodically segmented waveguides," *Applied Optics*, vol. 38, pp. 5734–5737, 1999.
- [75] S. Monneret, P. H. Chantome, and F. Flory, "m-lines technique : prism coupling measurement and discussion of accuracy for homogeneous waveguides," *J. Opt. A: Pure Appl. Opt.*, vol. 2, pp. 188–195, 2000.

- [76] P. Mathey, P. Jullien, , and J. L. Bolzinger, "Refractive - index profile reconstructions in planar waveguides by the WKB inverse method and reflectivity calculations," *J. Opt. Soc. Am. B.*, vol. 12, pp. 1663–1670, 1995.
- [77] L. P. Shi, E. Y. B. Pun, and P. S. Chung, "Extended iwkb method for determination of the refractive index profile in optical waveguides," *Optics Letters*, vol. 20, no. 15, pp. 1622–1624, 1995.
- [78] D. Taillaert, W. Bogaerts, P. Bienstman, T. F. Krauss, P. V. Daele, I. Moerman, S. Versteuyft, K. D. Mesel, and R. Baets, "An out-of-plane grating coupler for efficient butt - coupling between compact planar waveguides and single - mode fibers," *IEEE Journal Of Quantum Electronics*, vol. 38, no. 7, pp. 949–955, 2002.
- [79] D. Castaldini, P. Bassi, S. Tascu, S. Gregory, P. Aschieri, M. De Micheli, P. Baldi, K. Thyagarajan, and M. R. Shenoy, "All-in-one measurement setup for fast and accurate characterization of linear guided-wave optical devices," submitted to *Opt. Eng.*
- [80] G. Tittelbach, B. Richeter, and W. Karthe, "Comparison of three transmission methods for integrated optical waveguide propagation loss measurement," *Pure Appl. Opt.*, vol. 2, pp. 683–700, 1993.
- [81] P. J. Brannon, "Improved method of measuring optical waveguide propagation losses," *Applied Optics*, vol. 25, no. 20, pp. 3596–3598, 1986.
- [82] D. B. Ostrowsky, A. M. Roy, and J. Sevin, "Integrated optical waveguide examination using anti-stokes fluorescence," *Applied Physics Letter*, vol. 24, pp. 553–554, 1974.
- [83] R. Regener and W. Sohler, "Loss in low-finesse  $Ti : LiNbO_3$  optical waveguide resonators," *Applied Physics B*, vol. 36, pp. 143–147, 1985.
- [84] A. Ghatak and k. Thyagarajan, *An Introduction to Fiber Optics*. Cambridge University Press, 1998.
- [85] L. G. Cohen and C. Lin, "A universal fiber-optic (UFO) measurement system based on a near-ir raman laser," *IEEE J. Quantum Electron.*, vol. QE-14, pp. 855–859, 1978.
- [86] C. Lin, A. R. Tynes, A. Tomita, P. L. Lin, and D. L. Philen, "Chromatic dispersion measurements in single-mode fibers using picosecond InGaAsP injection lasers in the 1.2 to 1.5  $\mu$ m spectral region," *Bell Syst. Tech. J.*, vol. 62, no. 2, pp. 457–462, 1983.

- [87] M. J. Saunders and W. B. Gardner, "Precision interferometric measurement of dispersion in short single mode fibers," in *Tech Dig. NBS Symp. on Opt. Fib. Meas. (Boulder, CO), Oct. 2-3, 123-126*, 1984.
- [88] H. T. Shang, "Chromatic dispersion measurement by white-light interferometry on metre-length single-mode optical fibers," *Electron. Lett.*, vol. 17, pp. 603–605, 1981.
- [89] R. Zoli, M. Gnan, D. Castaldini, G. Bellanca, and P. Bassi, "Reformulation of the plane wave method to model photonic crystal," *Opt. Express*, vol. 11, p. 2905, 2003.
- [90] R. Zoli, D. Castaldini, M. Gnan, G. Bellanca, and P. Bassi, "2d and 3d numerical investigation of photonic crystal waveguides," in *NUMELEC*, 2003.
- [91] D. Castaldini, R. Zoli, A. Parini, G. Bellanca, and P. Bassi, "2d or 3d ftdt modeling of photonic crystal waveguides?" in *PIERS*, 2003.
- [92] D. Castaldini, "Analisi accurata di guide a cristallo fotonico 3d," in *RINEM*, 2004.
- [93] Y. A. Vlasov, M. O'Boyle, H. F. Hamann, and S. J. McNab, "Active control of slow light on chip with photonic crystal waveguides," *Nature*, vol. 438, p. 65, 2005.
- [94] A. Melloni, F. Morichetti, and M. Martinelli, "Optical slow-wave structures," in *Prof. of 31st European Conference on Optical Communication, Glasgow, UK, 25-29 Sept.*, 2005.
- [95] J. P. Pocholle, J. Auge, and M. Papuchon, "Determination of modal dispersion in monomode fibres from wavelength dependence of the mode spot size," *Electron. Lett.*, vol. 19, no. 25/26, pp. 1093–1094, 1983.
- [96] C. D. Hussey, "Field to dispersion relationships in single-mode fibers," *Electron. Lett.*, vol. 20, no. 25/26, pp. 1251–1252, 1984.
- [97] M. Notomi, K. Yamada, A. Shinya, J. Takahashi, C. Takahashi, and I. Yokohama, "Extremely large group-velocity dispersion of line-defect waveguides in photonic crystal slabs," *Physical Review Letters*, vol. 87, pp. 253 902–1–253 902–4, 2001.
- [98] F. Alard, L. Jeunehomme, and P. Sansonetti, "Fundamental mode spot-size measurement in single-mode optical fibers," *Electron. Lett.*, vol. 17, pp. 958–960, 1981.

- [99] D. Hannappe and J. Desbois, "Original method for measurement of optical mode fields," *Applied Optics*, vol. 35, no. 4, pp. 659–662, 1996.
- [100] A. T. Klemas, W. A. Reed, D. S. Shenk, and M. A. Saifi, "Analysis of mode-field radius calculated from far-field radiation patterns," in *Tech. Dig. OFS85 (San Diego, CA), Feb. 11-13, 30-31*, 1985.
- [101] [Online]. Available: <http://www.ni.com/labview/>
- [102] D. Marcuse, *Light Transmission Optics, 2nd Ed.* Van Nostrand, 1982.
- [103] K. Petermann, "Constraints for fundamental-mode spot size broad-band dispersion-compensated single-mode fibers," *Electron. Lett.*, vol. 19, p. 712, 1983.
- [104] *Corning SMF28 Optical Fiber Product Information, PI1036, (2002)*.
- [105] R. Alferness, V. Ramaswamy, S. Korotky, M. Divino, and L. Buhl, "Efficient single-mode fiber to titanium diffused lithium niobate waveguide coupling for  $\lambda = 1.32\mu\text{m}$ ," *IEEE Journal of Quantum Electronics*, vol. 18, no. 10, pp. 1807–1813, Oct 1982.
- [106] P. Suchoski and R. Ramaswamy, "Constant-width variable-index transition for efficient  $Ti : LiNbO_3$  waveguide-fiber coupling," *IEEE Journal Of Lightwave Technology*, vol. 5, pp. 1246–1251, 1987.
- [107] K. Kasaya, O. Mitomi, M. Naganuma, Y. Kondo, and Y. Noguchi, "A simple laterally tapered waveguide for low-loss coupling to single-mode fibers," *IEEE Journal of Photonics Technology Letters*, vol. 5, no. 3, pp. 345–347, March 1993.
- [108] B. Luyssaert, P. Bienstman, P. Vandersteegen, P. Dumon, and R. Baets, "Efficient nonadiabatic planar waveguide tapers," *IEEE Journal Of Lightwave Technology*, vol. 23, pp. 2462–2468, 2005.
- [109] F. Dorgeuille, B. Mersali, S. Francois, G. Herve-Gruyer, and M. Filoche, "Spot size transformer with a periodically segmented waveguide based on InP," *Optics Letters*, vol. 20, pp. 581–583, 1995.
- [110] M. M. Spühler, B. J. Offrein, G.-L. Bona, R. Germann, I. Massarek, and D. Erni, "A very short planar silica spot-size converter using a nonperiodic segmented waveguide," *IEEE Journal Of Lightwave Technology*, vol. 16, p. 1680, 1998.
- [111] Z. Weissman and I. Hendel, "Analysis of periodically segmented waveguide mode expanders," *IEEE Journal Of Lightwave Technology*, vol. 13, pp. 2053–2058, 1995.

- [112] M. Yanagisawa, Y. Yamada, and M. Kobayashi, "Low-loss and large tolerance fiber coupling of high- $\Delta$  silica waveguides by local mode-field conversion," *IEEE Photonics Technology Letters*, vol. 4, pp. 433–435, 1993.
- [113] O. Alibart, S. Tanzilli, D. B. Ostrowsky, and P. Baldi, "Guided wave technology for telecom wavelength heralded single photon source," *Optics Letters*, vol. 30, pp. 1539–1541, 2005.
- [114] D. Castaldini, P. Bassi, S. Tascu, P. Aschieri, M. De Micheli, and P. Baldi, "Soft proton exchange tapers for low insertion loss  $LiNbO_3$  devices." submitted to *IEEE Journal of Lightwave Technology*.
- [115] Z. Weissman and A. Hardy, "Modes of periodically segmented waveguides," *IEEE Journal Of Lightwave Technology*, vol. 11, p. 1831, 1993.
- [116] D. Ortega, J. M. Aldariz, J. M. Arnold, and J. S. Aitchison, "Analysis of "quasi-modes" in periodic segmented waveguides," *IEEE Journal Of Lightwave Technology*, vol. 17, pp. 369–375, 1999.
- [117] F. Fogli, "Unpublished material."
- [118] W. Tittel, J. Brendel, H. Zbinden, and N. Gisin, "Quantum cryptography using entangled photons in energy-time bell states," *Physical Review Letters*, vol. 84, pp. 4737–4740, 2000.
- [119] G. Bertocchi, D. Castaldini, S. Tascu, D. B. Ostrowsky, S. Tanzilli, M. De Micheli, and P. Baldi, "Integrated-optics quantum relay : Preliminary results," in *ECOC*, 2006.
- [120] G. Bertocchi, "Circuit optique sur  $LiNbO_3$  pour un relais quantique intégré," Ph.D. dissertation, Laboratoire de Physique de la Matière Condensée, 2006.
- [121] M. A. Nielsen and I. L. Chuang, *Quantum Computation and Quantum Information*. Cambridge University Press, 2000.
- [122] I. Marcikic, H. de Riedmatten, W. Tittel, H. Zbinden, and N. Gisin, "Long-distance teleportation of qubits at telecommunication wavelengths," *Nature*, vol. 421, pp. 509–513, 2003.
- [123] D. Castaldini et al., "To be published."
- [124] D. Marcuse, "Mode conversion caused by surface imperfections of a dielectric slab waveguide," *J. Bell Syst. Tech.*, vol. 48, pp. 3187–3215, 1969.

# Acknowledgments

I am deeply grateful to Prof. Paolo Bassi and Prof. Pascal Baldi for giving me the opportunity to work for this interesting and fascinating subject and allowing me to spend a lot of time in two beautiful cities like Bologna and Nice. I am grateful to all the members of DEIS and LPMC in general for the stimulating environment they create and for the many teachings and fruitful advises. In particular I would like to thank Dr Marc De Micheli, Dr Sorin Tascu, Dr Pierre Aschieri, Dr Gaetano Bellanca, Prof. Giovanni Tartarini, Prof. Dan Ostrowsky, Dr Sébastien Tanzilli for helping and assisting me with great expertise.

My sincere thanks also to Marco Gnan, Lara Scolari, Davide Pierleoni, Fabrizio Fogli, Giovanni Battista Montanari, Simone Berneschi, Rossella Zoli, Guido Sanna, Guillaume Bertocchi, Pierre Aboussouan, Olivier Alibert, for the useful discussions and the many fruitful exchanges.

I am grateful to all my friends for their support during these three years and for the unforgivable moments: Nicola Bariselli, Mirco Bovo, Diego Castelli, Valérie Doya, Elisa Garavini, Stefano Gulinelli, Nadir Kchit, Pavel Khuzir, Julien Kieffer, David Laurent, Modesto Lopez, Jerome Maria, Matteo Montanari, Mathieu Neuville, Nicola Panacci, Alberto Parini, Oliver Pozo and Claudia Strazzari.

## **Studio, fabbricazione e caratterizzazione di guide segmentate per componenti fotonici avanzati su Niobato di Litio**

In questa tesi di dottorato descriviamo il progetto, la fabbricazione e la caratterizzazione di componenti basati su guide segmentate per applicazioni di ottica integrata. Una guida segmentata è una struttura ottica caratterizzata da una variazione longitudinale dell'indice di rifrazione.

Tra le numerose applicazioni in cui le guide segmentate possono essere inserite apportando dei miglioramenti, descriviamo con maggior dettaglio il taper e il filtro modale. Il primo componente è in grado di migliorare l'efficienza dell'accoppiamento tra fibra e guida. Il secondo permette di rimuovere i modi di ordine superiore in propagazione in una guida multimodo.

Per capire il comportamento fisico delle guide segmentate, descriviamo inizialmente in maniera analitica la propagazione del campo elettromagnetico per strutture periodiche e successivamente eseguiamo uno studio numerico utilizzando il 3D Beam Propagation Method. Questo strumento numerico permette di progettare i componenti a guide segmentate e lo schema della maschera per la fotolitografia.

Al termine dello studio analitico e numerico abbiamo fabbricato i dispositivi utilizzando la tecnica del Soft Proton Exchange su un substrato di Niobato di Litio.

Per determinare le prestazioni dei dispositivi fabbricati è richiesta una completa caratterizzazione. Per fare questo, abbiamo sviluppato un banco di misura in grado di valutare le perdite alla propagazione, il comportamento dispersivo e la forma del modo nelle guide ottiche. I risultati delle caratterizzazioni mostrano che introducendo un taper in un sistema di telecomunicazioni standard è possibile ottenere una riduzione delle perdite di inserzione fino a 1.5 dB. Per quanto riguarda il filtro modale, mostriamo che i modi di ordine superiore vengono filtrati da una guida multimodo a 840 nm lasciando inalterato il modo fondamentale. Questa funzionalità può produrre vantaggi nelle operazioni di conversione di frequenza basate su interazioni non lineari. Per entrambe i componenti i risultati sperimentali sono in buon accordo con le previsioni fornite dalle simulazioni numeriche.

# **Etude, réalisation et caractérisation des guides segmentés pour composants photoniques avancés sur Niobate de Lithium**

Dans cette thèse de doctorat nous décrivons l'étude, la fabrication et la caractérisation des composants basés sur les guides d'onde segmentés pour des applications d'optique intégré. Un guide segmenté est une structure optique caractérisé par une variations longitudinal de l'indice de réfraction.

Parmi les nombreuses applications dans lesquelles les guides segmenté peuvent être utilement introduites, nous décrivons avec plus de détail le taper et le filtre modal. Le premier composant peut augmenter l'efficacité du couplage entre fibre et guide d'ondes. Le deuxième permet d'éliminer les modes d'ordre supérieur en propagation dans un guide multimode.

Afin de comprendre le comportement physique des guides segmentés, nous décrivons d'abord de façon analytique la propagation du champ dans les structures périodiques et par la suite nous faisons des analyses numériques en utilisant la méthode développée 3D Beam Propagation Method. Cet outil numérique permet de designer les composants basés sur guides segmentés et aussi le plan du masque de photolithographie.

Après l'étude analytique et numérique, nous avons fabriqué les dispositifs en utilisant la technique du Soft Proton Exchange sur un substrat de Niobate de Lithium.

Pour déterminer les prestations des dispositifs fabriqués est nécessaire de faire une complète caractérisation. Pour ça, nous avons développé un banc de mesure pour l'évaluation des pertes à la propagation, le comportement dispersif et la reconstruction de la forme du mode des guides d'onde. Les résultats de la caractérisation montrent que en introduisant des tapers dans un système standard de télécommunication, on peut obtenir des avantages en termes de réduction des pertes d'insertion d'environ 1.5 dB. Pour ce qui concerne le filtre modal, nous prouvons que les modes d'ordre supérieur sont filtrés d'un guide d'onde mulimodal à 840 nm en laissant inaltéré le mode fondamental. Cette fonctionnalité peut induire des avantages dans des opérations de conversion de fréquence basées sur les interactions non linéaires. Pour les deux composants fabriqués, les résultats expérimentaux sont en bon accord avec les prévisions numériques.

# **Study, fabrication and characterization of segmented waveguides for advanced photonic components on Lithium Niobate**

In this PhD thesis we describe the design, the fabrication and the characterization of components for integrated optic applications based on segmented waveguides. A segmented waveguide is an optical structure with longitudinal variations of the refractive index.

Among the numerous applications in which segmented waveguides can be usefully introduced, we describe with more detail tapers and mode filters. The former component can increase the fiber-to-waveguide coupling efficiency. The latter can remove higher order modes from the propagation in multimode waveguides.

In order to understand the physical behavior of segmented waveguides, we first describe analytically the propagation characteristics of periodic structures and then perform a numerical analysis using the developed 3D Beam Propagation Method. This numerical tool allows to design the segmented waveguide components and the photomask draft. After developing the analytical and the numerical investigation, we have fabricated the devices using the Soft Proton Exchange technique on Lithium Niobate substrate.

To determine the performances of the fabricated devices a complete characterization is required. To do that, we have developed an all-in-one experimental setup for the evaluation of the propagation losses, the dispersive behavior and the mode shape reconstruction of integrated optical waveguides. The results of the characterization show that inserting the taper in a standard telecommunication system, it is possible to obtain advantages in terms of insertion losses reduction of about 1.5 dB. Concerning the modal filter, we show that the higher order modes are filtered from a multimode waveguide at 840 nm leaving unchanged the fundamental one. This functionality can induce advantages in frequency conversion operations based on non linear interactions. For both the components the experimental results are in good agreement with numerical predictions.